DEUTERIUM NMR INVESTIGATION OF THE EFFECT OF ISOPROPYL MYRISTATE ON THE SKIN BARRIER USING A MODEL STRATUM CORNEUM

by

John Tien Jui Cheng
Bachelor of Science, Simon Fraser University 2004

THESIS SUBMITTED IN PARTIAL FULFILLMENT OF
THE REQUIREMENTS FOR THE DEGREE OF

MASTER OF SCIENCE

In the
Department
of
Molecular Biology and Biochemistry

SIMON FRASER UNIVERSITY

Fall 2005

APPROVAL

Name:	**John Tien Jui Cheng**
Degree:	**Master of Science**
Title of Thesis:	**Deuterium NMR Investigation of the Effect of Isopropyl Myristate on the Skin Barrier using a Model Stratum Corneum**
Examining Committee:	**Chair: Dr. F. F. Pio** Assistant Professor, Department of Molecular Biology and Biochemistry
	Dr. J. L. Thewalt Senior Supervisor Associate Professor, Department of Molecular Biology and Biochemistry/Physics
	Dr. R. B. Cornell Supervisor Professor, Department of Molecular Biology and Biochemistry/Chemistry
	Dr. M. W. Paetzel Supervisor Assistant Professor, Department of Molecular Biology and Biochemistry
	Dr. C. N. Kitson **Internal Examiner** Clinical Associate Professor of Department of Medicine, Division of Dermatology The University of British Columbia
Date Defended/Approved:	**November 24, 2005**

ABSTRACT

The function of the skin as a barrier is found to be closely associated with lipids in the stratum corneum (SC). At physiological temperature, SC lipids form solid or crystalline domains which may contribute to skin impermeability. A ^{2}H-NMR study has been conducted to observe the effect of Isopropyl Myristate (IPM), a skin penetration enhancer, on the physical properties of model SC (MSC). IPM was added to MSC comprising equimolar mixtures of *N*-palmitoyl D-erythro-sphingosine (Cer16), cholesterol and palmitic acid (PA), containing either Cer16-d_{31} or PA-d_{31}. ^{2}H-NMR data showed that IPM had pronounced effects on the phase behaviour of MSC. Relative proportions of solid, liquid-crystalline and isotropic phases varied with temperature and IPM concentration. Further experiments, using synthesized chain-deuterated IPM, allowed the examination of the behaviour of IPM in MSC. These data, coupled with other studies, can help elucidate the effect of IPM on the integrity of the SC barrier.

DEDICATION

To my Lord, Jesus Christ, the Saviour,
who was, is and is to come,
and will come to judge this world.

To my dear parents, Jackson Kuang Fu Cheng and Lillian Li Ling Hung,
and my dear brother, Peter Tien Hao Cheng.

For God so loved the world that He gave His one and only Son,
that whoever believes in Him shall not perish
but have eternal life.
(John 3:16, The Holy Bible)

ACKNOWLEDGEMENTS

As a Christian, I would like to thank my Lord, Jesus Christ, for His love, guidance, help and support for the past two years of study in the MBB M.Sc. program at SFU, in which He has proven it to me that being a Christian and studying science are not in conflict. I would like to take this opportunity to thank my senior supervisor, Dr. J. L. Thewalt for her expert help and guidance for the past two years, and for offering this great opportunity for me to work on this project in which I have excelled and achieved great accomplishment, and I have thus confirmed my goal in pursuing further study in the field of physical biochemistry and biophysics. I would also like to thank my committee members, Dr. R. B. Cornell and Dr. M. W. Paetzel, for their great help and support whenever I seek assistance. A special "thank you" should be dedicated to Dr. E. E. Brief, who was a postdoctoral fellow in Thewalt Laboratory, for her professional collaboration in this study and her continuous support both academically and personally, as she has been more of an elder sister to me than merely a co-worker. I would want to thank all of my co-workers for their cooperation and support in the lab. I would also want to thank my friends from Evangelical Chinese Bible Church, church fellowship, badminton club and all other friends for their continuous comfort and company. I must thank my parents and brother for their endless love and support, as I cannot have completed this study without them. Finally, but not the least, I would like to dedicate my special appreciation to Simon Fraser University for providing me with this fantastic opportunity to accomplish both my undergraduate and master degrees in Molecular Biology and Biochemistry in which I have been trained to become a professional in this field.

TABLE OF CONTENTS

LIST OF FIGURES

LIST OF TABLES

LIST OF EQUATIONS

LIST OF PROCEDURES

LIST OF COMPUTER PROGRAM SCRIPTS

GLOSSARY

Ω	ohm, unit of resistance.
ν_0	Resonance frequency, a vector quantity
ν	Frequency of precession, a vector quantity
°C	Degree Celsius
$\nu_{C\text{-}HS}$	The chemical shift value of a specific bond or functional group of a chemical compound in Infrared Spectroscopy or Fourier Transform Infrared Spectroscopy.
τ_L	Long repetition time for ^{2}H-NMR data acquisition
µl	microlitre (10^{-6} litre)
τ_S	Short repetition time for ^{2}H-NMR data acquisition
^{1}H-NMR	Proton Nuclear Magnetic Resonance
^{2}H-NMR	Deuterium Nuclear Magnetic Resonance
^{13}C-NMR	Carbon-13 Nuclear Magnetic Resonance
B	Magnetic field, a vector quantity
B_0	The external magnetic field, a vector quantity
BBCer	Bovine Brain Ceramides
$CDCl_3$	Deuterated chloroform
Cer16	*N*-palmitoyl D-erythro-sphingosine
Cer16-d_{31}	Deuterated *N*-palmitoyl D-erythro-sphingosine
$CHCl_3$	Chloroform
Chol	Cholesterol
Chol-d_6	Deuterated cholesterol
cm^{-1}	Wavenumber, the unit of chemical shift in FTIR/IR.
CPE	Chemical Penetration Enhancer
DMSO	Dimethyl Sulfoxide
DSC	Differential Scanning Calorimetry
EH_L	Echo Height obtained from the ^{2}H-NMR data acquisition with long repetition time
EH_S	Echo Height obtained from the ^{2}H-NMR data acquisition with short repetition time

EtOH	Ethanol (Ethyl alcohol)
FFA	Free Fatty Acid
FID	Free Induction Decay
FTIR	Fourier Transform Infrared (Spectroscopy)
g	gram
H_2O	Water
$He_{(l)}$	Liquid helium
Hz	Hertz (cycles/second)
IPA	Isopropyl Alcohol (2-propanol or isopropanol)
IPM	Isopropyl Myristate
IPM-d_{27}	Deuterated Isopropyl Myristate
IR	Infrared (Spectroscopy)
kHz	kilohertz
Lipid domain	A domain in the MSC/SC membranes/bilayers that is restricted to specific lipid/lipids.
M	Magnetization spins, a vector quantity
M_0	Total magnetization spins, a vector quantity
M_1	The average width of a ^{2}H-NMR spectrum. The unit is sec^{-1}.
MeOH	Methanol (Methyl alcohol)
mg	milligram (10^{-3} gram)
min	minute
ml	millilitre (10^{-3} litre)
mM	Millimolar (10^{-3} mol/litre)
mol/mol	Mole to mole ratio
MSC	Model Stratum Corneum. It is an equimolar mixture of *N*-palmitoyl D-erythro-sphingosine (Cer16), Cholesterol (Chol) and Hexadecanoic acid (PA).
mtorr	millitorr (10^{-3} torr)
M_x	Magnetization spins along x-axis, a vector quantity
M_{xy}	Magnetization spins along xy-plane, a vector quantity
M_y	Magnetization spins along y-axis, a vector quantity
M_z	Magnetization spins along x-axis, a vector quantity
$N_{2\ (l)}$	Liquid nitrogen
nm	Nanometer (10^{-9} meter)
NMP	N-methyl-2-pyrrolidone
NMR	Nuclear Magnetic Resonance

OA	Oleic Acid
OA-d_2	Deuterated oleic acid
PA	Palmitic acid (Hexadecanoic acid)
PA-d_{31}	Deuterated palmitic acid
Phase behaviour	The temperature-dependent and CPE-concentration-dependent behaviour of a specific phase component of individual deuterated membrane lipids in MSC.
Phase component	The quantitative measure of a specific phase.
Phase composition	This can be defined in two ideas. One is the combination of various phases in MSC. Another is the list of membrane lipid components that comprise a specific phase. Phase composition can be temperature-dependent and CPE-concentration-dependent.
Phase conversion	The process of a specific phase component converting into another specific phase component.
Phase domain	A domain in the MSC/SC membranes/bilayers that is restricted to specific phase/phases.
Phase profile	The temperature-dependent and CPE-concentration-dependent behaviour of all phase components of a specific deuterated membrane lipid in MSC.
Phase property	Phase behaviour, phase profile, phase composition, phase transition of individual membrane lipids in MSC or MSC.
Phase quantity	The percentage of a specific phase component with respect to the total.
Phase separation	A phenomenon observed in the MSC/SC membranes/bilayers in which membrane components segregate into domains of same lipid species.
Phase transition	The process of one or more phase components converting into one or or more phase components. A phase transition may consist of multiple phase conversions.
Phase transition temperature	The temperature at which a phase transition occurs. It may be a range of temperatures.
ppm	part per million
rad	radian
Reptime	Repetition time. It is the amount of delay time that is required between individual data acquisition when performing a ^{2}H-NMR experiment. It is dependent on the value of T_1.
RF	Radio frequency
R_f	Retardation factor
s	second
SAXD	Small Angle X-ray Diffraction
SC	Stratum Corneum

sec	second
T	Tesla, unit of magnetic field
TDD	Transdermal Drug Delivery
TLC	Thin Layer Chromatography
T_m	The solid to liquid-crystalline phase transition temperature.
UV	Ultraviolet
v/v	Volume to volume ratio
w/v	Weight to volume ratio
w/w	Weight to weight ratio
WAXD	Wide Angle X-ray Diffraction

CHAPTER 1: INTRODUCTION

Traditional drug delivery usually involves ingestion and injection. They are sometimes not efficient (ingestion) and cause irritations (injection). A drug delivered through ingestion has to travel to the treatment site and its effect could be decreased through a long travel distance, particularly if the drug is biodegradable. A drug delivered through injection can be directly applied to the treatment site; however, needles are usually physically and psychologically unpleasant. Transdermal Drug Delivery (TDD) has been studied for decades as an alternative to drug ingestion and injection. It is a method of delivering drugs to the treatment site through the skin. However, it has limitations. The skin is found to be a strong barrier resisting the drug permeation. The stratum corneum (SC), the outermost layer of the skin, is one of the key components that lowers the drug permeation rate and sometimes inhibits the drug permeation entirely.

This chapter will introduce the reader to the structure and functions of the skin, particularly SC, and their relationship to difficulties behind TDD. In order to overcome this barrier problem, a chemical penetration enhancer (CPE) is often used to facilitate/accelerate TDD. This chapter will outline an overview of the usage of CPEs in various TDD studies and the physical/molecular mechanisms of penetration enhancement. Then, this chapter will give more details on simplified model systems, which has been used instead of the real skin for studying TDD, so that the behaviour of individual SC components can be observed. Various techniques have been utilized to

observe drug permeation mechanisms and efficiencies in both the real skin and model systems, and they will be described in more depth. Particularly, a comprehensive description of deuterium nuclear magnetic resonance spectroscopy (^{2}H-NMR) will be included in Chapter 2 since ^{2}H-NMR was used as the spectroscopic tool in our study. In our study, we used ^{2}H-NMR to investigate the behaviour and transdermal enhancement mechanisms of isopropyl myristate (IPM), a commonly used CPE in commercial products, in a well defined and developed model system. A section of this chapter will be used to summarize the findings of several studies on the penetration enhancement mechanisms of IPM as a CPE, including the recent findings from the *in vitro* study by Brinkmann and Müller-Goymann (Brinkmann and Müller-Goymann, 2003) which is the basis of our ^{2}H-NMR study. Finally, this chapter will end with a brief description of the logic and series of experimental approaches to reach the understanding of IPM as a CPE in a model system using ^{2}H-NMR spectroscopy.

1.1 The skin

The skin is a very complex organ. It has numerous tissues arranged in a well defined structure in order to support its various functions. The skin can be divided into two layers resting on a basal layer, namely the epidermis and the dermis resting on the hypodermis. Epidermis is a type of epithelia. Different types of epithelia serve different functions and line different organs. The specific epithelial structure of epidermis allows it to play a key role in waterproof and barrier functions. This section will give a brief overview of the structural differences in different types of epithelia in an organism. Then, the structure and functions of epidermis, dermis and hypodermis will be stated in more

details. Particularly, the structure and functions of SC will be described thoroughly, as to how they enhance the skin impermeability and resistance to drug permeation, and how changes in SC structure can influence the overall skin permeability.

1.1.1 Epithelium

Epithelium is a layer of tissue covering internal and external surfaces of the body. It is composed of various cells, glands, blood vessels and extracellular matrices. The functions of epithelia include protections of underlying structure, barriers, permeation, secretion and absorption of substances. Epithelia are divided into different categories according to their cell shapes, arrangements and functions. Simple squamous epithelium consists of a single layer of thin, fat cells functioning in passive diffusion of substances. Simple cuboidal epithelium consists of a single layer of cube-like cells facilitating active transport of molecules. Simple columnar epithelium consists of a single layer of tall, thin cells performing active secretion of mucus and enzymes as well as active and passive transport of substances. Pseudostratified columnar epithelium consists of a single layer of cells, of which some are and some are not in contact with the surface, resembling a two-layered structure, functioning in secretion of mucus and disposal of debris through cilia movement. Transitional epithelium belongs to the category of stratified epithelium with its stretching function upon expansion of pouch organs. Finally, stratified squamous epithelium consists of numerous layers of cells, acting as the barrier function, with inner layers of cells proliferating and replacing the shedding and damaged outer layers of cells. (Seeley *et al.*, 2005) The epidermal tissue of the skin belongs to this category (stratified squamous epithelium).

1.1.2 Functions and structures of the skin

Skin is considered an organ, actually the largest organ in the body. It consists of complex arrays of tissues that function together to accomplish particular tasks. It has numerous functions including regulation of body temperature (thermal regulation), hydroregulation, protection, sensation, cutaneous absorption and excretion, immunity, synthesis, blood reservoir and communication (Seeley *et al.*, 2005; Van De Graaff, 2002). With these functions, the skin is able to build the first line of defence against abrasions, infections and dehydrations (Seeley *et al.*, 2005). Without the skin, the organism would be subjected to damages from above leading to possible death.

The skin is a multilayered, house-like structure (Figure 1). It has several accessory organs such as hairs, glands, blood vessels and fats. The skin consists of two major layers, the dermis and the epidermis, resting on the innermost layer, the hypodermis. The hypodermis acts as the foundation of the house structure, connecting the skin to underlying bones and muscles, providing mechanical supports through loose connective tissues (collagenous and elastic fibers) and insulation/cushion through accumulation of subcutaneous fat (Seeley *et al.*, 2005; Van De Graaff, 2002). The dermis is located between the hypodermis and the epidermis (the body of the house), which consists of fibroblasts, fat cells and macrophages. It acts as a dense connective tissue and is responsible for the structural strength of the skin through cross-linking networks of collagen fibers to produce resistance to stretch. Vascular supply of nutrients through blood and lymphatic vessels nourishes dermal cells, glands and hair follicles. These vessels are also responsible for removal of waste and for thermal regulation. The innervation of nerve endings and presence of glands provide the skin with sensation and

hydroregulation. The dermis can be divided into two layers, the upper stratum papillarosum (papillary layer) which is closely associated with the epidermis, and the lower stratum reticularosum (reticular layer) which forms the thick, firm yet resilient meshwork. (Seeley *et al.*, 2005; Tortora, 1995; Van De Graaff, 2002)

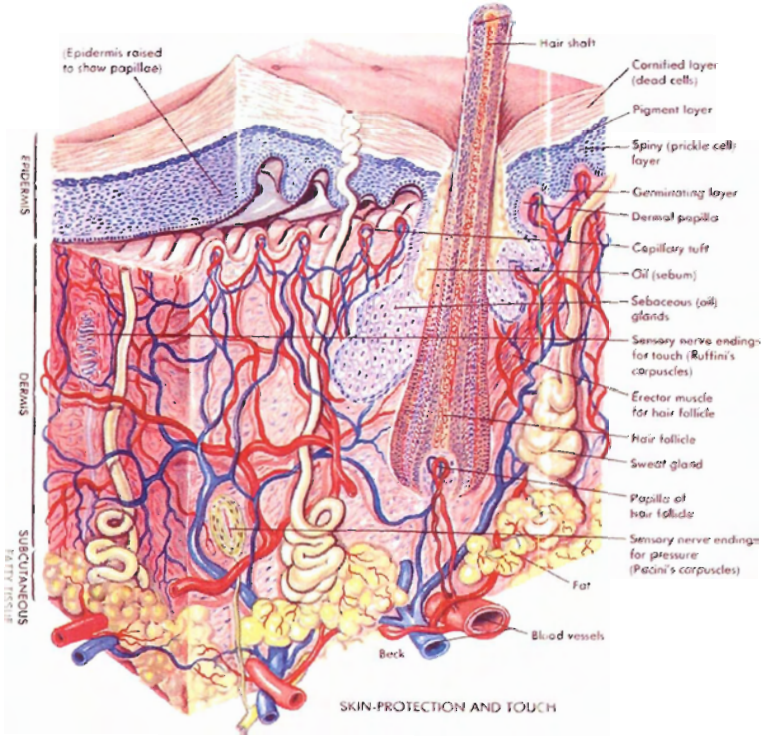

Figure 1: The skin.

The skin is usually described as a house-like structure, the Epidermis (the roof of the house) and the Dermis (the body of the house) resting on the Hypodermis (the foundation of the house). [Adapted from Clausen, K., The Aikido FAQ.] (Clausen, 1993-2004)

The uppermost layer of the skin is called the epidermis (the roof of the house). It is composed of four types of cells and five distinct layers (strata). Keratinocytes (90% of the epidermal cells) produce the protein keratin which is responsible for the rigidity of the skin. Melanocytes (8% of the epidermal cells) synthesize the brown-black pigment melanin capable of absorbing ultraviolet (UV) light to protect keratinocytes from genetic

damage and the skin from radiation. Langerhans cells originate in bone marrow and cooperate with helper T cells in immune responses. Other immune response cells include nonpigmented granular dendrocytes and protective macrophages. Both types of cells ingest bacteria and foreign debris in the stratum basale (the deepest epidermal layer). Merkel cells provide the sensory function of the skin through their connection to the endings of sensory neurons in tactile discs. While located at the stratum basale, these cells are attached to keratinocytes through cellular junctions. The last two types of cells comprise the remaining 2% of the epidermal population. (Tortora, 1995; Van De Graaff, 2002)

The stratum basale is the innermost single layer composed of the four types of cells mentioned earlier. It is the location of stem cell population and proliferation, and it is also the place where sweat glands, oil glands and hair follicles originate. The next layer is the stratum spinosum (eight to ten layers of cells), characterized by the spinelike protrusions from the keratinocytes which join themselves together and with the melanocytes. The rate of cell proliferation is relatively slow compared to the stratum basale. The layer above the stratum spinosum is the stratum granulosum (three to five layers of cells), in which the cells contain dark granules of keratohyalin as the precursor of keratin. The next layer up is the stratum lucidum (three to five layers of cells), in which cells are invisible (transparent histologically). These cells produce eleidin, a derivative of keratohyalin, to form keratin. This stratum exists only in the lips, the soles and palms. The final and most superficial layer of the skin is the stratum corneum (SC), which acts as the first line of defence/barrier and controls the exchange between the external environment and internal organs of an organism. (Blank, 1965; Potts and

Francoeur, 1990; Seeley *et al.*, 2005; Sweeney and Downing, 1970; Tortora, 1995; Van De Graaff, 2002; Wertz and Downing, 1989). Figure 2 shows the five stratum layers of the epidermis.

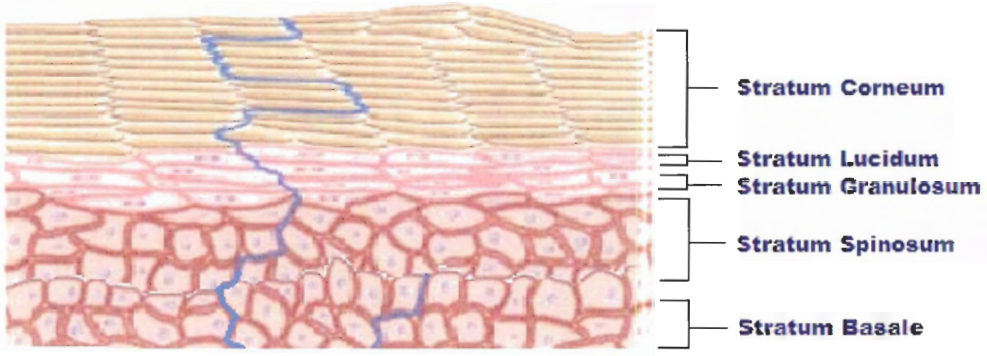

Figure 2: The epidermis.

This diagram illustrates the five stratum layers of the epidermis. Refer to the text for more details. Note that the blue line represents the possible skin permeation route through the intercellular lipid matrix. [Adapted from Gray J., P&G Beauty Science.] (Gray, 1997)

1.1.3 The stratum corneum

SC consists of 25 to 30 layers of flat, dead keratinocytes, filled up fully with keratins, and joined by desmosomes (Seeley *et al.*, 2005). These dead cells derive from the progressive drive of cells in the stratum basale toward the superficial layers. As cells approach the superficial layers, the blood and oxygen supply are disconnected which causes the degeneration of nuclei (and other organelles) and the subsequent keratinization of cells. These layers of dead cells undergo cornification, where they are dried and flattened to build the protective cover on the top of the skin. These cells are now called corneocytes (Elias, 1983; Schurer and Elias, 1991). The shedding of these keratinized cells off SC occurs through breakage of desmosomes, and it is a continuous process

where the empty space is filled constantly with new keratinized cells. (Tortora, 1995; Van De Graaff, 2002)

The intercellular spaces of keratinized cells in SC are filled with lipids (Elias, 1983; Schurer and Elias, 1991; Wertz, 2000). They play very important roles in minimizing fluid loss (Potts and Francoeur, 1990; Seeley *et al.*, 2005). Elias and Friend (1975) suggested that even though keratinized cell layers in SC are demonstrated to be an effective barrier, the actual impermeable barrier is formed by the progressive accumulation of lamellar material and other substances secreted from lamellar bodies in the mid-to-upper stratum granulosa. The secretion of these materials leads to the formation of a wide, persistent barrier in the intercellular spaces of SC which is capable of resisting percutaneous absorption or secretion. Lamellar materials are secreted as lipid packages and found to be mostly lipids. (Elias and Friend, 1975)

SC lipids consist of three major classes: ceramides, cholesterol and free fatty acids (FFA) (Bouwstra *et al.*, 2003; Elias, 1983; Lampe *et al.*, 1983; Wertz *et al.*, 1987; Yardley and Summerly, 1981). By 2003, eight subclasses of ceramides have been found in human SC, differing mostly by the headgroup (Bouwstra *et al.*, 2003). FFA comprises saturated 12- to 36-carbon chains, with 22- to 26-carbon FFA being the most abundant (Norlén *et al.*, 1998). A tiny amount of cholesterol sulfate is also present in addition to cholesterol, which is responsible for desquamation of SC (Bouwstra *et al.*, 2003). These lipids form a tightly associated cross-linking network in various crystalline domains, with chains mostly in orthorhombic and hexagonal packing conformations (Bouwstra *et al.*, 1992; Bouwstra *et al.*, 1996; Bouwstra 1997; Bouwstra *et al.*, 2003; White *et al.*, 1988). These conformational domains have been found to have a crucial influence on the

integrity of the SC structure (Forslind, 1994). Differential Scanning Calorimetry (DSC) and Infrared Spectroscopy (IR) data have found that a lipid thermotropic transition occurs between 60°C ~ 80°C from an ordered crystalline structure to a more disordered liquid-crystalline structure (Golden *et al.*, 1986; Ongpipattanakul *et al.*, 1994) (Refer to Section 1.4 for DSC and IR techniques). Similar studies proposed that upon the thermotropic transition, the permeability of SC increases from the low value associated with an ordered SC structure to a much higher value associated with a disordered SC structure (Golden *et al.*, 1987; Knutson *et al.*, 1985;Potts and Francoeur, 1990). Thus, SC lipids play a very important role in the SC permeability and barrier function, and provide the route for drug permeation (Elias and Friend, 1975; Golden *et al.*, 1987; Knutson *et al.*, 1985; Potts and Francoeur, 1990; Sweeney and Downing, 1970). By perturbing the phase behaviour, composition, transition and order of this barrier, the resistance to percutaneous absorption can be compromised (Golden *et al.*, 1987; Knutson *et al.*, 1985; Potts and Francoeur, 1990).

1.2 Chemical Penetration Enhancer (CPE)

The SC barrier has always been a limitation to TDD. In order to make it easier for substances to permeate through the skin, it is necessary to reduce the SC barrier function or create additional pathways through SC. Various methods have been used to increase the permeability of SC, including the physical enhancement through iontophoresis, the supersaturation of topical vehicles in SC, and the usage of metabolic and biochemical enhancers (Finnin and Morgan, 1999). Recently, a great amount of work has been put into studying the effect, ability and mechanism of chemical penetration enhancers (CPE)

in facilitating percutaneous permeation (Benson, 2005). Examples of CPEs include Dimethyl sulfoxide (DMSO), Ethanol (EtOH) and Laurocapram (Azone), which are found to improve the transdermal permeation of different agents (Ghanem *et al.*, 1992; Kanikkannan *et al.*, 2000; Stoughton and Fritsch, 1964; Wiechers and de Zeeuw, 1990). Both *ex vivo* and *in vitro* studies have suggested that CPEs improve the SC permeability by persisting in SC, disrupting the physiochemical structure of SC or partially extracting SC lipids (Benson 2005; Kanikkannan *et al.*, 2000; Suhonen *et al.*, 1999). Other CPEs include the most recent finding of Iminosulfuranes for its non-toxicity (Song *et al.*, 2005).

Classical CPEs such as Azone, EtOH and DMSO have been widely investigated. Each of them is proposed to enhance the skin permeability through distinct mechanisms, although most of them remain speculative. Azone has been suggested to facilitate TDD by forming ionic pairs with anionic drugs, fluidizing SC lipids by inserting into the ceramide bilayers, exerting hydration effect on SC for easier penetration of hydrophilic drugs, and increasing thermodynamic driving force by decreasing activation energy (Hadgraft *et al.*, 1985; Ito *et al.*, 1988; Ogiso *et al.*, 1992; Sugibayashi *et al.*, 1992), although it is not persisting in SC for a long period of time (Wieshers *et al.*, 1987). EtOH has been proposed to modify the polar headgroup region of the lipid bilayers by displacing the headgroup-bound water, interdigitating into the SC lipid bilayers at low concentrations, and extracting SC lipids at high concentrations (Suhonen *et al.*, 1999). DMSO has been suggested to facilitate the drug permeation through fast establishment of drug reservoir in SC, active extraction of SC components (possibly leading to loss of barrier mass) and displacing bound water from proteins or lipids (for a more solvated environment) (Smith and Maibach, 1995).

Binary and ternary CPE systems, surprisingly, have long been utilized to further improve percutaneous absorption. The earliest finding can be dated back to the *in vitro* study of Azone and Propylene Glycol (PG) at 1987 which showed that Azone/PG is more effective than Azone alone (Priborsky *et al.*, 1987). Other examples include co-enhancement of Azone by N-methyl-2-pyrrolidone (NMP) and incorporation of Azone, NMP or DMSO in PG formulations of the drug to achieve better drug permeation (Priborsky *et al.*, 1987; Sugibayashi *et al.*, 1989). A ternary CPE system using a solvent system such as ethanol-water, in addition to a CPE such as l-menthol, was also found to increase the drug delivery through the skin as well (Al-Saidan *et al.*, 2004; Morimoto *et al.*, 2000).

While these *ex vivo* and *in vitro* studies provide qualitative and some quantitative investigation of CPEs in enhancing the permeability of SC, only few model studies have been conducted to provide more quantitative and biophysical analyses on the property changes of SC membrane components in relationship to the permeability enhancement upon CPE applications. The next section will describe the model system that has been used to observe the biophysical properties of SC in TDD studies.

1.3 Studying TDD in model systems

A more quantitative approach to studying permeation through the skin in model systems requires a model stratum corneum (MSC). Because of the complexity in the lipid composition of SC, it is necessary to use an MSC with simplified lipid compositions, comprising of only major classes of lipids found in SC. MSC containing ceramide (Cer), cholesterol (Chol) and palmitic acid (PA) has been used as a model membrane system to

study the epidermal permeability (Kitson *et al.*, 1994; Thewalt *et al.*, 1992). Phase property changes of each lipid class can be observed as a function of temperature. The changes in the phase behaviour, profile and composition can reflect changes in the order of MSC structure in the presence of a CPE. As the order of phase structure and transition of model system is well correlated with that of SC (Abraham and Downing, 1991; Fenske *et al.*, 1994; Kitson *et al.*, 1994), these changes in MSC would simulate changes in SC.

However, a few components that exist in SC are not included in MSC. Examples include intracellular and matrix proteins such as keratins (Suhonen *et al.*, 1999). Studies suggested that these protein crosslinking networks contribute to resistance against percutaneous absorption (Suhonen *et al.*, 1999). These components may play crucial roles in drug permeation through the cellular regions in SC (transcellular transport). This is not taken into consideration in our study since we are investigating the effect of CPEs on intercellular transport (via intercellular lipid matrix). Even though MSC lacks some equivalent SC components, studies have shown that SC lipids (Cer, Chol and FFA) are the major components in contributing the barrier function of SC (Abraham and Downing, 1991; Fenske *et al.*, 1994; Kitson *et al.*, 1994). Therefore, MSC is considered a valid system depicting SC in this study.

Macroscopic changes in phase behaviour and composition of MSC can be detected and observed by various methods. The next section will introduce a number of techniques commonly used to study CPEs in TDD.

1.4 Techniques for studying TDD

A wide range of methods have been used to study the effect of CPE on drug permeation (mostly in SC), including Fourier Transform Infrared Spectroscopy (FTIR), Differential Scanning Calorimetry (DSC), X-Ray Crystallography and Deuterium NMR Spectroscopy (^{2}H-NMR). These techniques provide information of both macroscopic and microscopic changes in the skin when CPE is applied.

FTIR reflects changes in the vibrational energy levels of covalent bonds. There are two major types of molecular vibrations: the stretching (symmetric and asymmetric) and bending (rocking, scissoring, wagging and twisting). When applying FTIR radiation, the absorption by the molecular bond can be detected only if there is a change in the dipole moment of the molecule in molecular vibration motion. The frequency of absorption is dependent on the bond strengths and the mass of atoms, and it is specific for the type of bond. Generally, the stronger the bond is, the higher the energy is required to induce molecular vibrations (with a net dipole change), and the absorption peak will appear at the higher wavenumber. When studying the lipids in SC or MSC using FTIR, the position of the C-H stretching ($\nu_{C\text{-}H}$s) absorption peak is sensitive to and can shift upon the change in the conformational order of the hydrocarbon chains (Knutson *et al.*, 1985; Lafleur, 1998). More ordered conformations would be at low-energy states and absorb FTIR radiation at lower frequencies (lower wavenumbers); whereas, less ordered conformations would be at high-energy states and absorb FTIR radiation at higher frequencies (higher wavenumbers). As the conformational order of SC lipids is responsible for the order of the SC structure (Forslind, 1994), the shift of the $\nu_{C\text{-}H}$s absorption peak can thus provide information on the change in the overall structural order

and phase transition of SC and MSC (Knutson *et al.*, 1985; Lafleur, 1998). For example, in MSC (equimolar mixture of ceramide/sphingomyelin, cholesterol and palmitic acid), a gradual shift in the position of the $\nu_{C\text{-}H}$s absorption peak occurs from 2849.5 cm^{-1} to 2850 cm^{-1} at low temperatures (5°C ~ 40°C); whereas, a larger shift in the position of the $\nu_{C\text{-}H}$s absorption peak occurs from 2850 cm^{-1} to 2854 cm^{-1} at high temperatures (40°C to 75°C) (Lafleur, 1998). In addition, the disappearance, reduced intensity or broadening of an FTIR peak can also indicate the disruption of a specific bond or structure in both SC and MSC, for example, upon CPE application.

DSC measures the amount of energy required to induce a phase transition by outlining a heating profile of the sample. The heating profile of the sample is usually measured against that of an inert reference. The power required to keep the sample at the same temperature as the inert reference as both are heated is measured and converted to the enthalpy change associated with phase transition in the sample. The heat absorption is then plotted as a function of temperature in a DSC thermogram as the heating profile of the sample. A melting transition is an endothermic reaction, so it can be detected as an endothermic peak in a DSC thermogram. Thus, a phase transition of SC or MSC can be observed from the appearance of an endothermic peak in the DSC thermogram. In SC, a total of four thermal transitions have been observed. The first two thermal transitions (~ 40°C and ~ 70°C) have been suggested to be the phase transitions of SC lipids (Golden *et al.*, 1986; Golden *et al.*, 1987; Van Duzee, 1975); whereas, the last two thermal transitions (~ 85°C and ~ 95°C) have been suggested to be the phase transitions of intercellular lipids bound with membrane protein complexes and intracellular keratin (Golden *et al.*, 1986; Golden *et al.*, 1987; Van Duzee, 1975). The shift in the phase

transition temperature suggests whether the integrity of SC structure is maintained (Hirvonen *et al.*, 1995).

X-ray crystallography examines the crystal structure of a substance. When the substance is irradiated with a monochromatic x-ray from one direction, each unit cell of the crystal diffracts the X-ray forming a pattern which is the sum of constructive interferences. X-ray irradiation from three different directions would result in three specific diffraction patterns. These diffraction patterns can be superimposed to create a characteristic diffraction image with high-intensity spots called reflections. The distance between individual reflections and the distance between reflections and the central spot indicate the spacing of the lattice plane and thus give the information on the structure of the crystal. X-ray diffraction observations on SC include Small-Angle X-ray Diffraction (SAXD, angular range 1°-10°) and Wide-Angle X-ray Diffraction (WAXD, angular range 7°-60°), which can be used to measure the repeat distance of lipid bilayer packing and the distance of lipid lateral packing, respectively. In addition, the intensity and position of SAXD/WAXD peaks provide information on the relative proportion and identity of specific lipid conformational domains in SC (Bouwstra *et al.*, 1994; Bouwstra *et al.*, 2003). The change in the intensity of a specific SAXD/WAXD peak indicates the change in the relative proportion of a specific lipid conformational domain in SC. The shift in the position of a SAXD/WAXD peak shows the change in the lipid packing distance and the order of a specific lipid conformational domain. In SC, three distinct WAXD reflections have been observed at 0.367 nm, 0.413 nm and 0.467 nm, corresponding to the orthorhombically packed lipids, hexagonally packed lipids and corneocyte-bonded lipids, respectively (Bouwstra *et al.*, 2003; Brinkmann and Müller-

Goymann, 2003). An SAXD reflection has also been observed at 6.4 nm, which corresponds to the lipid bilayers packing in SC (Brinkmann and Müller-Goymann, 2003).

^{2}H-NMR can be used to observe the structural flexibility and molecular reorientation of lipids. Deuterating either Cer16 or PA allows ^{2}H-NMR observation on the structural influence of CPE on separate membrane components in MSC. ^{2}H-NMR spectra also provide information on the phase behaviour, profile and composition of MSC lipids at different temperatures. The average spectral width, or M_1, can also be analyzed to find the relative order of membranes. In the previous ^{2}H-NMR study of MSC (equimolar mixture of ceramide/sphingomyelin, cholesterol and palmitic acid), ^{2}H-NMR spectra and M_1 values showed characteristics of more ordered phase conformations at lower temperatures, and showed characteristics of less ordered phase conformations at higher temperatures (Kitson *et al.*, 1994). The authors suggested that the phase behaviour and M_1 value of MSC are temperature-dependent (Kitson *et al.*, 1994). A more detailed description of the ^{2}H-NMR technique will be given in Chapter 2.

1.5 IPM as a CPE

Isopropyl myristate is a widely known CPE. It has been used in several commercial products including cosmetics and creams. It has also been used in several *ex vivo* and *in vitro* drug permeation studies including hydrocortisone, terbinafine, mefenamic acid and emedastine (antihistamine) (Alberti *et al.*, 2001; Brinkmann and Müller-Goymann, 2003; Fang *et al.*, 2002; Harada *et al.*, 2005). Recent research suggested that the combination of IPM with other CPEs, such as 2-propanol (isopropyl alcohol), ethanol and triethanolamine, increases the drug permeation rate and

bioavailability of these drugs. (Alberti *et al.*, 2001; Brinkmann and Müller-Goymann, 2003; Fang *et al.*, 2002). Several mechanisms of penetration enhancement by IPM were proposed. FTIR studies showed that in the presence of IPM, the peak intensity of $\nu_{C\text{-}H}$s does not decrease but the peak shifts to a higher wavenumber (higher frequencies), which suggested that IPM increases the fluidity/disorder of SC structure (Pillai *et al.*, 2004). DSC studies demonstrated that the IPM-containing application to the skin *in vitro* results in a decrease of the phase transition temperature from ~ 70°C to ~ 62°C (intercellular lipid phase transition), and from ~ 81°C to ~ 75°C (intercellular lipids/membrane protein complex phase transition), which suggested that IPM causes a higher disorder in the SC lipid microstructure (Brinkmann and Müller-Goymann, 2003; Leopold and Lippold, 1995). SAXD/WAXD data showed a decrease in the intensity and shift in the position of peaks in SC pretreated with IPM, which suggested that IPM disrupts the SC lipid packing (Brinkmann and Müller-Goymann, 2003). These studies suggest that IPM is capable of integrating into the lipid bilayers to cause increased membrane fluidity, which may contribute to the increased disorder of SC and thus enhances the permeability of SC lipids.

To further understand these mechanisms, we have investigated the effect and behaviour of IPM in MSC. Since the conformational order of SC intercellular lipids is responsible for drug permeation through intercellular pathways, by disrupting the order of SC intercellular lipid packing and structure, we can achieve better SC permeability. Since only intercellular lipid species are involved in the intercellular pathways and we are not investigating the transcellular pathways, cellular proteins and envelope components can be neglected. Consequently, studying the effect and behaviour of IPM in MSC allows us

to achieve a better understanding (in a model system) of how IPM acts on the SC intercellular lipids to modify intercellular transport routes. While *ex vivo* and *in vitro* studies mentioned above suggest the possible mechanisms and interactions of IPM with SC lipids, our investigation allows the observation of changes of individual MSC membrane components in response to the addition of IPM. The temperature-dependent phase appearance, behaviour, profile and composition can be analyzed quantitatively for each membrane component. The CPE-concentration-dependent phase changes can also be observed in the membrane components individually. Hence, both temperature- and CPE-concentration-dependent changes in the phase properties of MSC can be proposed.

Since IPM causes increased fluidity/disorder in the SC lipid bilayers, we hypothesized that the addition of IPM would cause increased fluidity/disorder in the MSC lipid structure. We examined the changes in the phase properties and M_1 as functions of temperature and concentration of IPM added. We expected that the changes in phase properties would lead to the change in the MSC structural order.

CHAPTER 2: BASICS OF DEUTERIUM NUCLEAR MAGNETIC RESONANCE SPECTROSCOPY (^{2}H-NMR)

This chapter will give a brief overview of nuclear magnetic resonance (NMR) spectroscopy. This chapter is divided into three major sections. The first section deals with the general principles of NMR, how NMR works, and how NMR spectroscopy is performed. A brief description of NMR spectrometer hardware will also be included in this section. The second section lists a number of important parameters that we measure in ^{2}H-NMR spectroscopy. We will look at the importance of operating the NMR spectrometer at the resonance frequency of the sample, how a Free Induction Decay (FID) is obtained at the resonance frequency, and the types of nuclear magnetic relaxation mechanisms we acquire an FID from. The last section deals with the interpretation of Fourier transformed ^{2}H-NMR spectra, and the relationship between the ^{2}H-NMR spectral shape and the phase of the sample. The characteristic spectral features in each ^{2}H-NMR spectrum of different phases will be described and compared to demonstrate the qualitative determination of phase changes of the sample. This chapter will conclude with the list of information that we can get from a ^{2}H-NMR spectrum.

2.1 What is NMR spectroscopy?

NMR spectroscopy is a technique for measuring phenomena which involve nuclei of atoms. Nuclei have magnetic moments (μ) in "spins". When nuclei with a non-zero spins are placed in an external magnetic field $\mathbf{B}_0$, they will interact with the magnetic

field and yield a signal when the frequency of the nuclear precession matches the frequency of the external magnetic field (Refer to Section 2.2.1 and Figure 7). **M** is the vector quantity of the sum of these magnetic moments, and $\mathbf{M}_0$ is the vector that defines **M** when **M** is in its equilibrium position along the z axis in $\mathbf{B}_0$. When another magnetic field ($\mathbf{B}_1$) is applied, **M** will be tipped to the xy plane and the signal measured comes from the vector $\mathbf{M}_{xy}$. Depending on the nucleus and its environment, it allows researchers to learn and obtain information related to molecular or atomic/subatomic interactions and activities, relative positions and motions of a molecule with respect to others, phases and the chemical environment around a specific molecule/atom, and so on. NMR spectroscopy is not a highly sensitive technique because the number of spins at the higher energy level is very close to the number of spins at the lower energy level at room temperature according to the Boltzmann distribution (Refer to Section 2.1.1 for Boltzmann distribution).

There are various types of NMR spectroscopy. The most commonly used are ^{1}H (proton), ^{2}H (deuterium), and ^{13}C (carbon-13) NMR spectroscopy. Others include ^{3}He (helium), ^{15}N (nitrogen), and ^{31}P (phosphorus) NMR spectroscopy. In our study, we used ^{2}H-NMR spectroscopy. The following section will introduce how ^{2}H-NMR spectroscopy works.

2.1.1 How does NMR work?

There are two levels of energy state for spin ½ particles with magnetic moment μ, in a constant magnetic field, **B**. The energy difference between the two states is ΔE =

$2\mu\mathbf{B}$. According to Boltzmann distribution, the ratio of the spins in the upper and lower energy level is given by the Boltzmann equation:

$$\frac{N_1}{N_2} = e^{\frac{-\Delta E}{kT}}$$

Equation 1: The Boltzmann distribution

Where N_1 is the number of spins in the upper energy level and N_2 is that in the lower, ΔE is the energy difference between the two levels, k is the Boltzmann's constant [1.38066×10^{-23} $J \cdot K^{-1}$] and T is the temperature [°K]. Figure 3 illustrates the energy difference between the two levels.

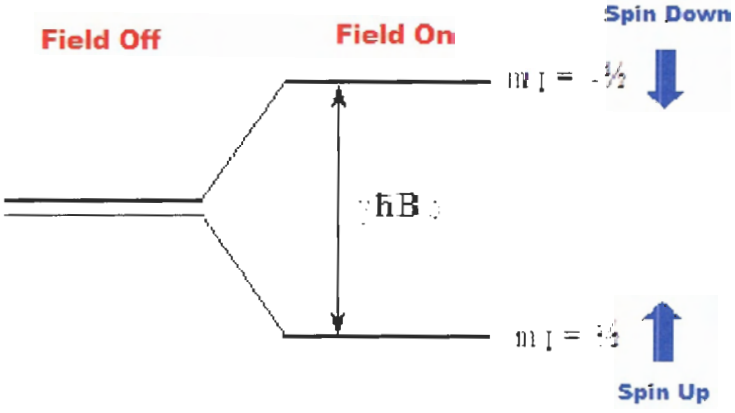

Figure 3: The energy difference between the two levels in protons (I = ½).
m_I = -½ is the higher energy level with spins antiparallel to the external magnetic field $\mathbf{B}_0$. m_I = ½ is the lower energy level with spins parallel to the external magnetic field $\mathbf{B}_0$.

Protons have nuclear spins of ½, so they have two energy levels. Boltzmann distribution predicts that nuclei will favour the lower energy level in order to reach the equilibrium state when they are placed in $\mathbf{B}_0$. If at the same time they are irradiated with an RF, they will be excited to the higher energy level. When they return to the lower

energy level, they will emit signals that give information about their chemical environment.

2.1.2 ^{2}H-NMR spectroscopy and quadrupolar interaction

For deuterons, it is slightly different. Deuterons have nuclear spins of 1, so they have three energy levels. They will still obey the principle of Boltzmann distribution. If they are placed in $\mathbf{B}_0$, they will favour the lower energy level to reach the equilibrium state as well. If they are irradiated with an RF, they will also be excited but to two different levels (1 to 0 and 0 to -1). When they return to the lower energy levels (-1 to 0 and 0 to 1), they will emit different signals that give information about their phases.

Figure 4 shows the three energy levels in deuterons:

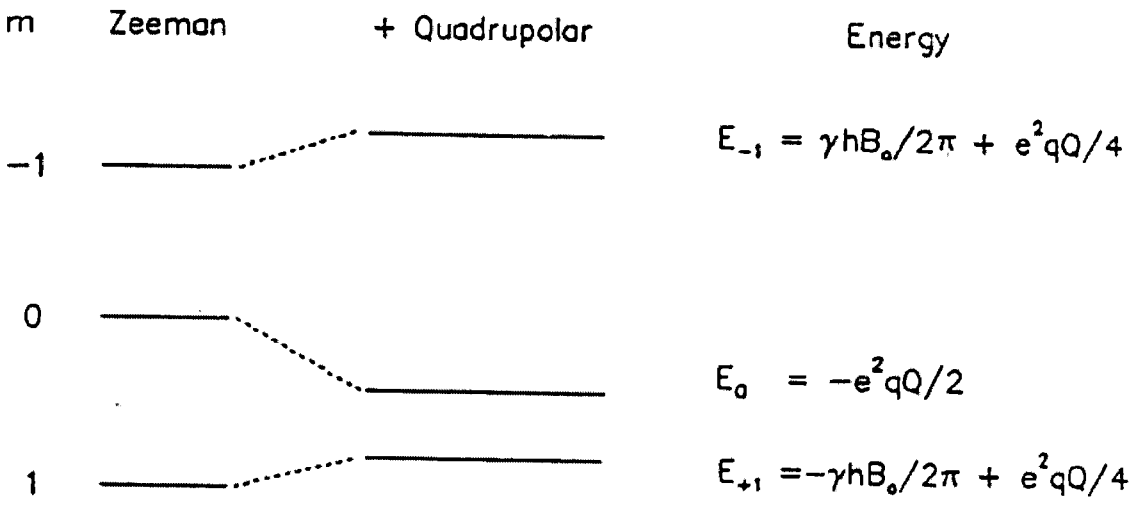

Figure 4: The energy difference among three levels in deuterons (I = 1).

m = -1 is the higher energy level with spins antiparallel to the external magnetic field $\mathbf{B}_0$. m = 1 is the lower energy level with spins parallel to the external magnetic field $\mathbf{B}_0$. m = 0 is the energy level in between m = -1 and m = 1. [Adapted from J. L. Thewalt, Simon Fraser University.]

Quadrupolar interaction is an interaction between the nuclear spin $I \geq 1$ (For example, the deuteron nucleus which has a non-spherically symmetric nuclear charge distribution) and the electric field gradient at the nucleus. In our deuterated MSC lipid samples, the electric field gradient is the C-D bond. As a result of the quadrupolar interaction, the ^{2}H-NMR spectral lines observed from quadrupolar nuclei are split by quadrupolar splitting, $\Delta\nu_Q$ [kHz]. The $\Delta\nu_Q$ is dependent on the orientation (θ) of C-D bond with respect to the magnetic field, which is shown by the following equation:

$$\Delta\nu_Q = \frac{3}{2}\left(\frac{e^2qQ}{h}\right)\left(\frac{3\cos^2\theta - 1}{2}\right)$$

Equation 2: Quadrupolar splitting

Where $\left(\frac{e^2qQ}{h}\right)$ is the quadrupolar coupling constant [168 kHz]. The sum of all orientations gives rise to a ^{2}H-NMR spectrum, a characteristic Pake doublet with a quadrupolar splitting $(\Delta\nu_Q)_{90°}$ measured between the sharp 90° peaks.

In lipids undergoing different motions, the orientation of the C-D bond with respect to the magnetic field is averaged differently. In a solid phase, there is no lipid motion. Thus, no motional averaging occurs for the C-D bond and according to Equation 2, the $(\Delta\nu_Q)_{90°}$ = 126 kHz. In a liquid-crystalline phase, the lipids undergo axially symmetric rotation, and this effectively reduces the quadrupolar interaction. The average orientation of the C-D bond with respect to the axis of lipid symmetry is 90° in an all-trans lipid chain, and the maximum $\Delta\nu_Q$ is reduced to 63 kHz. In an isotropic phase, since lipid molecules are in rapidly reorienting, the C-D bond would explore all orientations, which averages the quadrupolar interaction to zero. Thus, $\Delta\nu_Q$ is 0 kHz, so the ^{2}H-NMR

spectrum is a single peak at the centre. More description of ^{2}H-NMR spectral interpretation and demonstration of ^{2}H-NMR spectra of different phases will be shown in Section 2.2.4.

2.1.3 ^{2}H-NMR spectroscopy hardware: the magnet and probe

This section of the chapter will focus on the hardware of NMR spectroscopy, particularly the magnet, the probe and the spectrometer. The magnet provides the main fixed magnetic field. The probe secures the sample and carries various cables and electronics connected to the spectrometer. The spectrometer contains all the electronic equipment for performing an NMR experiment.

2.1.3.1 The NMR magnet

In our ^{2}H-NMR study, we used the 300 MHz Oxford Superconducting Magnet with the magnetic field of approximately 7 T. The NMR magnet is located inside a silver dewar with plugs for liquid helium (He $_{(l)}$) and liquid nitrogen (N_2 $_{(l)}$). The NMR magnet is submerged in a pool of He $_{(l)}$ surrounded with another pool of N_2 $_{(l)}$ in order to keep the NMR magnet cool. By cooling the NMR magnet, any loss of electric current due to heat dissipation can be prevented under this extremely low-temperature condition. No power supply is needed to maintain the electric current once it has been started. (Rowat, 1996)

Information regarding different samples can be acquired using the same NMR magnet and spectrometer. In our study, the ^{2}H-NMR spectra of lipid samples are acquired using the quadrupolar echo technique (Davis *et al.*, 1976), with a locally built spectrometer operating approximately at 46.8 MHz. However, the transmitter radio

frequency is mostly set at 46.79 MHz with minor adjustment depending on the resonance frequency of the sample. A number of parameters will need to be adjusted before running a ^{2}H-NMR experiment on a deuterated sample, including the pulse length, the interpulse spacing, the dwell time and the repetition time (the delay time between data acquisitions).

Figure 5 is a photograph of the Oxford Superconducting Magnet showing the silver dewar, plugs for He $_{(l)}$ and $N_{2\ (l)}$ and various cable connections to the probe.

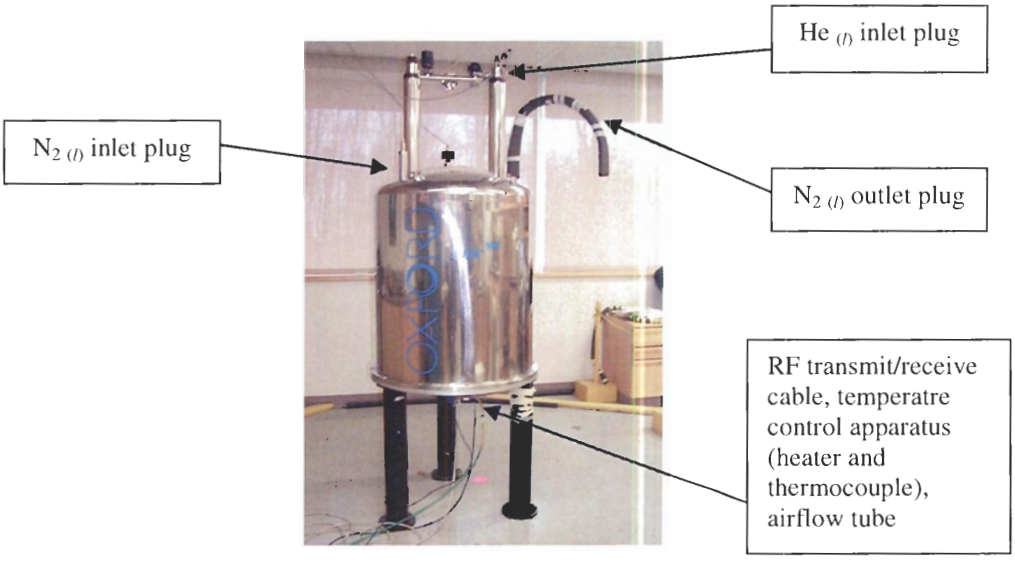

Figure 5: The Oxford Superconducting Magnet

2.1.3.2 The probe

The sample probe is a tube-like structure that holds and secures the sample in a coil, and positions it in the centre of the magnetic field produced by the NMR magnet. The probe consists of several metal rods and plates (the skeleton), two brass rods (for manual handling of the probe), a ceramic plate on which the coil is mounted, a thermocouple and two capacitor rods (both are inserted from the bottom of the probe and attached to the ceramic plate), a plug for the transmitter/receiver cable, and a glass case to

protect the coil and the sample. Some probes are designed to be able to fit between the pole faces of a magnet or in the bore of a superconducting solenoid.

The coil is a unique part of the probe which can act as the transmitter coil that applies the input RF pulse or the receiver coil that detects the output signal. The coil is designed to meet a few criteria: able to handle the large RF voltage while the pulse is on; recover rapidly from this powerful pulse; quickly receive and process the weak nuclear signal following the pulse. The probe used in our ^{2}H-NMR experiments is manufactured by "Morris Instruments" with few partially home-made/locally-built parts.

Figure 6 shows detailed photographs of the probe and its components. Different views of the probe are included in this figure as well. Photographs of the coil with and without the NMR sample tube, as well as with and without the glass case, are presented in this figure. The bottom view of the probe shows the translucent capacitor rods (for tuning the probe to the resonance frequency of the sample) and the plug for transmitter/receiver cable. It is hard to obtain an image of the inductor, so it is not included in this figure. A photograph of the NMR sample tube is also included in this figure.

(i) Coil & Thermocouple

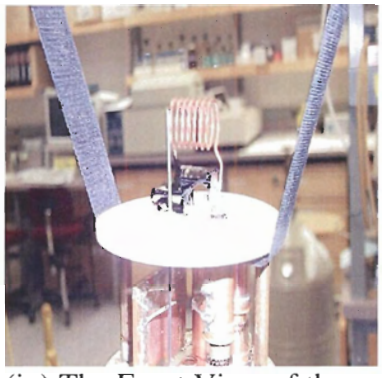

(ii) The Left View of the Probe Head

(iii) The Front View of the Probe Head

(iv) The Front View of the Probe Head with Capacitors

(v) The NMR Tube

(vi) The Bottom View of the Probe. Note the two translucent Capacitor rods.

Figure 6: The structure and components of the NMR magnet probe.

This figure shows the different views and the hand-drawn schematic diagram of the probe. Different views reveal different parts of the probe which show the delicacy and neat design of the probe. The image of an NMR tube is also included. [Courtesy of E. E. Brief, Simon Fraser University.]

2.1.3.3 The spectrometer

The transmitter/receiver cable, thermocouple and heater are connected between the spectrometer and the probe. The spectrometer is connected to a spectrometer computer. The spectrometer computer allows the operator to design and input computer

programs or single commands to operate the spectrometer. The spectrometer inputs RF pulses, receives the signal and processes the data according to the computer program commands.

2.2 What does ^{2}H-NMR spectroscopy measure?

^{2}H-NMR spectroscopy measures the Free Induction Decay (FID) of the total signal due to magnetization from nuclear spins of a deuterated sample. In order to obtain an exponential FID, the spectrometer has to operate at the resonance frequency of the deuterated sample. The repetition of FID data acquisition is dependent on the T_1 relaxation mechanism of the nuclear magnetization spins. This section will give a brief overview of what the resonance frequency, FID and T_1 relaxation are, and how they are measured by ^{2}H-NMR spectroscopy.

2.2.1 Resonance frequency

This section will describe briefly what radio, resonance and transmitter frequencies are, the difference between them and how to determine whether the resonance is matched.

2.2.1.1 Radio frequency, resonance frequency and transmitter frequency

Radio frequency (RF) is a general term describing one slice of the electromagnetic spectrum. It is the frequencies of the electromagnetic spectrum normally associated with radio wave propagation. It ranges from 3 kHz to 300 GHz.

Resonance frequency is the same as Larmor frequency of precession. It is a specific frequency of precession for a given type of nuclei in a given magnetic field. (Farrar and Becker, 1971; Fukushima and Roeder, 1994)

Transmitter frequency is the reference frequency that the transmitter of the NMR spectrometer applies a pulse at (Farrar and Becker, 1971). Generally, by locating the sample in the main magnetic field $\mathbf{B}_0$ and adjusting the transmitter frequency through a range of radio frequencies, the resonance frequency of a specific type of sample (For example, the deuterated lipid membrane sample) can be determined.

2.2.1.2 How to find the resonance frequency

Energy is absorbed from the RF field only when the radio frequency ν_{rf} obeys the resonant condition (Farrar and Becker, 1971):

$$\vec{\nu}_{rf} = \overrightarrow{\nu_0}$$

Equation 3: The resonance frequency

Where ν_0 is the Larmor frequency of precession for the given nuclei in a specific magnetic field $\mathbf{B}_0$.

The magnetic vector of the RF field, $\mathbf{B}_1$, can be thought of as rotating in the xy plane (the plane perpendicular to $\mathbf{B}_0$). On absorption from $\mathbf{B}_1$, the magnetic moment tips to a different angle θ, but the precession frequency remains constant. Refer to Figure 7 for illustration (Farrar and Becker, 1971).

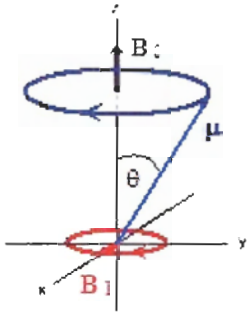

Figure 7: The precession of a magnetic moment μ about a fixed external magnetic field B_0 with an applied magnetic field B_1.

The radio frequency field $\mathbf{B}_1$ rotates in the xy plane. The external magnetic field $\mathbf{B}_0$ is aligned along the z-axis. The magnetic moment μ is precessing at an angle θ with respect to the z-axis. [Adapted from Farrar, T. C. and Becker, E. D., 1971. *Pulse & Fourier Transform NMR*, p. 6, Academic Press Inc.] (Farrar and Becker, 1971)

The Larmor equation is used to analyze each radio frequency setting to see the effect of different transmitter frequencies on the FID. By using this equation, the resonance frequency of a specific type of nuclei can be calculated. The Larmor equation is presented below:

$$\vec{\nu}_0 = -\frac{\gamma \vec{H}_0}{2\pi} \text{ [Hz]}$$

Equation 4: The Larmor equation in frequency [Hz]

OR

$$\vec{\omega}_0 = -\gamma \vec{H}_0 \text{ [rad·s}^{-1}\text{]}$$

Equation 5: The Larmor equation in angular velocity [rad·s^{-1}]

Where ν_0 is the Larmor frequency of precession [Hz]; ω_0 is the angular velocity of precession [rad·sec^{-1}]; γ is the magnetogyric ratio [sec^{-1}·T^{-1}]; $\mathbf{B}_0$ is the external magnetic field the sample is located in [T]. From this equation, it can be seen that ν_0 is proportional

to and dependent on the magnetic field strength. So, the resonance frequency may be different in different external magnetic field. However, since our NMR magnet produces a constant external magnetic field at 7 T, ν_0 will be dependent on γ value of the nuclei observed. In our ^{2}H-NMR experiments, the resonance frequency of deuterated MSC lipid samples was found approximately 46.79 MHz.

In order to obtain an FID for analysis, the transmitter frequency has to be set at the Larmor frequency (resonance frequency) of the sample. The following section will discuss briefly how an FID is acquired and the results of acquiring an FID at and off resonance.

2.2.2 Free Induction Decay (FID)

This section will provide a brief description of what an FID is, how they are acquired and how an FID signal behaves if the pulse is applied from different directions.

2.2.2.1 What is an FID?

The spectrometer is designed such that it can only detect signals induced in the coil in the xy plane. Thus, the vector quantity of $\mathbf{M}_z$ is not observable but that of $\mathbf{M}_{xy}$ is. The vector quantity of $\mathbf{M}_{xy}$ indicates the intensity of the signal that the spectrometer detects. This observed signal is called a free induction signal. Over time, this signal will start to decay, as $\mathbf{M}_{xy}$ dephases. This phenomenon is called the "Free Induction Decay". (Farrar and Becker, 1971)

When the resonance frequency is matched, the FID will show as an exponential decay curve. The reason why this occurs is that if the RF (transmitter frequency) is in

resonance with the Larmor frequency, then the rotating frame of the applied magnetic field $\mathbf{B}_1$ is in phase with the rotating frame of **M** and thus, this would provide a detector which is referenced in phase to the RF. Since $\mathbf{B}_1$ and **M** are in phase, the detector would be able to detect a pure exponential decay along a fixed axis in the rotating frame (e.g. y axis). However, if the RF is slightly different from the Larmor frequency, the rotating frame of the RF is not in phase with that of **M**. Since $\mathbf{B}_1$ and **M** are not in phase, the detector is referenced in phase not only to the RF, but also the **M** as well. The detector will display both the exponentially decaying value and the interference effect from the fact that the reference frequency and $\mathbf{M}_{xy}$ alternatively come in and out of phase with each other. This is why when the RF is off resonance, an oscillating decay of FID would be obtained instead of an exponential decay of FID. (Farrar and Becker, 1971) Figure 8 shows the FID at resonance and off resonance:

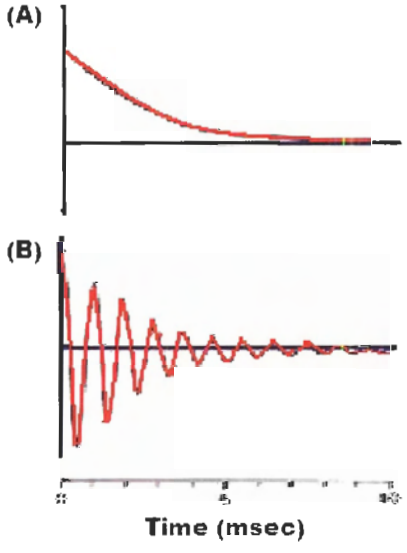

Figure 8: The Free Induction Decay.

(A) At Resonance and (B) Off Resonance. [Adapted from Farrar, T. C. and Becker, E. D., 1971. *Pulse & Fourier Transform NMR*, p. 20, Academic Press Inc.] (Farrar and Becker, 1971)

The time between data acquisitions and the decaying rate of a signal are dependent on two different relaxation mechanisms of the nuclear magnetization spins after a $\mathbf{B}_1$ application: T_1 and T_2 relaxation. T_1 is the time constant of **M** signal recovery to its equilibrium position ($\mathbf{M}_0$) along the z axis in $\mathbf{B}_0$. T_2 is the time constant of $\mathbf{M}_{xy}$ signal decay when **M** dephases in xy plane. In our ^{2}H-NMR experiments, the T_1 values of different phases determine the repetition times between data acquisitions, and the T_2 values of different phase determine the decaying rate of the signal.

2.2.3 T_1 relaxation

T_1 relaxation is a natural phenomenon which occurs when the magnetic moments attempt to align with the external magnetic field $\mathbf{B}_0$ in which they are placed. This phenomenon is not negligible and has impact on the setup of an NMR experiment, particularly on the value of repetition time (reptime). As it is mentioned in Section 2.1.3.1, reptime is the time of delay between data acquisitions. It is dependent on the value of T_1 for the full recovery of **M** back to its equilibrium position, so no signal can be detected and the next acquisition of data can be carried out.

Generally, when a single 90° pulse is generated along the x axis, **M** will be tipped from the equilibrium position, z axis, down to the y axis and start precessing about the y axis. After a period of time, **M** will decrease as magnetic moments dephase, and as well, **M** will slowly rotate back to its equilibrium position. This latter phenomenon is the process of T_1 relaxation. All these phenomena are observed under the conditions that the shape of the RF during a pulse is roughly rectangular or square wave, as the RF from the transmitter to the probe is turned on and off in a very rapid manner. In this way, the pulse

length, t_p, is relatively very short compared to T_1, so that it can be assumed that there is no relaxation occurring during the pulse. (Farrar and Becker, 1971)

Now, let's look at the physical processes of T_1 relaxation in NMR spectroscopy in detail. When a magnetic field, $\mathbf{B}_1$, is applied along the x axis, the total magnetization, **M**, will be tipped to, if by a full $\pi/2$ pulse, to the y axis. $\pi/2$ pulse is the pulse length in time unit required to tip **M** 90° fully from the z axis to the xy plane. When $\mathbf{B}_1$ is turned off, a few processes occur such that **M** will decrease both longitudinally and transversely and eventually, **M** will return to its equilibrium magnetization state, $\mathbf{M}_0$. **M** undergoes the longitudinal relaxation where it returns from the xy plane to its equilibrium position along the z axis. This is the process of spin-lattice relaxation. This relaxation occurs when the nuclear moments lose energy to their surroundings, and the $\mathbf{M}_z$ component of **M** will recover to its equilibrium value with the time constant, T_1. (Farrar and Becker, 1971)

In our ^{2}H-NMR experiments where the quadrupolar echo technique was used (Davis *et al.*, 1976), another $\pi/2$ pulse is applied at a period of time τ after the first $\pi/2$ pulse. $\mathbf{M}_{xy}$, which dephases in the xy plane after the first $\pi/2$ pulse, refocuses at the time 2τ to give the maximum signal (the echo). Then, the subsequent FID was recorded.

The T_1 value is different in different phases. In the solid phase, the nuclear magnetization spins takes the longest time to return to their equilibrium position in $\mathbf{B}_0$. In the liquid-crystalline phase, the nuclear magnetization spins take the shortest time to return to their equilibrium position in $\mathbf{B}_0$. In the isotropic phase, the nuclear magnetization spins take a slightly longer time than those in the liquid-crystalline phase to return to their equilibrium position in $\mathbf{B}_0$. Thus, the value of T_1 in different phases is: T_1 (liquid-crystalline) < T_1 (isotropic) < T_1 (solid). The difference in T_1 values has a major

impact on the speed of data collection (reptime settings). Generally, reptime is adjusted and set to be five times greater than T_1. In our ^{2}H-NMR experiments, two reptimes were used: the short reptime (300 msec) and the long reptime (1 sec ~ 50 sec). Since non-solid phase portions of the sample have a faster relaxation time, the short reptime data acquisition would include all the signals from non-solid phase portions. However, because the solid phase portion of the sample has a much slower relaxation time, the short reptime data acquisition would to a good approximation, not include the signal from the solid phase portion. The long reptime data acquisition, on the other hand, would include all the signals from all phases as it is sufficiently longer than the relaxation time of all phases. By acquiring signals using the short and long reptimes, we were able to distinguish the signals from the non-solid and solid phase portions of the sample.

2.2.4 Fourier transformed ^{2}H-NMR spectra and MSC phases

Fourier Transformation, as it is mentioned earlier, is a process to transform information (voltage) in the time domain (FID) to the frequency domain (spectrum) and vice versa. It involves a series of rigorous mathematical derivations and calculations. We will not discuss the mathematics of Fourier transformation in this chapter, as it is mostly performed by computer programs. However, it is necessary for us to look into how to interpret the Fourier transformed ^{2}H-NMR spectra and what phase information we can obtain from these spectra.

2.2.4.1 Interpreting the Fourier transformed ^{2}H-NMR spectra

The deuterated membrane component in MSC can exhibit different physical structures and characteristics in different phase conditions which result in distinct ^{2}H-NMR spectra. A Model Stratum Corneum (MSC) displays two different phases from a more ordered crystalline phase to a more mobile liquid-crystalline phase with the transition temperature $T_m \sim 42°C$ (Kitson *et al.*, 1994; Thewalt *et al.*, 1992). Below the phase transition, the MSC remains mostly in the solid or crystalline phase, During the phase transition, the MSC converts into from the solid or crystalline phase into the liquid-crystalline phase in which the deuterated acyl chains have increased mobility and undergo axially symmetric motion At higher temperatures, MSC undergoes the second phase transition from the liquid-crystalline phase into the isotropic phase, where the deuterated acyl chains have increased isotropic motion (high molecular motion/tumbling of deuterated acyl chain in all directions on the NMR timescale).

2.2.4.2 ^{2}H-NMR spectral shapes and MSC phases

By visualizing ^{2}H-NMR spectral shapes, the phase changes of MSC can be determined qualitatively. Figure 9 shows the ^{2}H-NMR spectral shape in relationship to the phase of MSC.

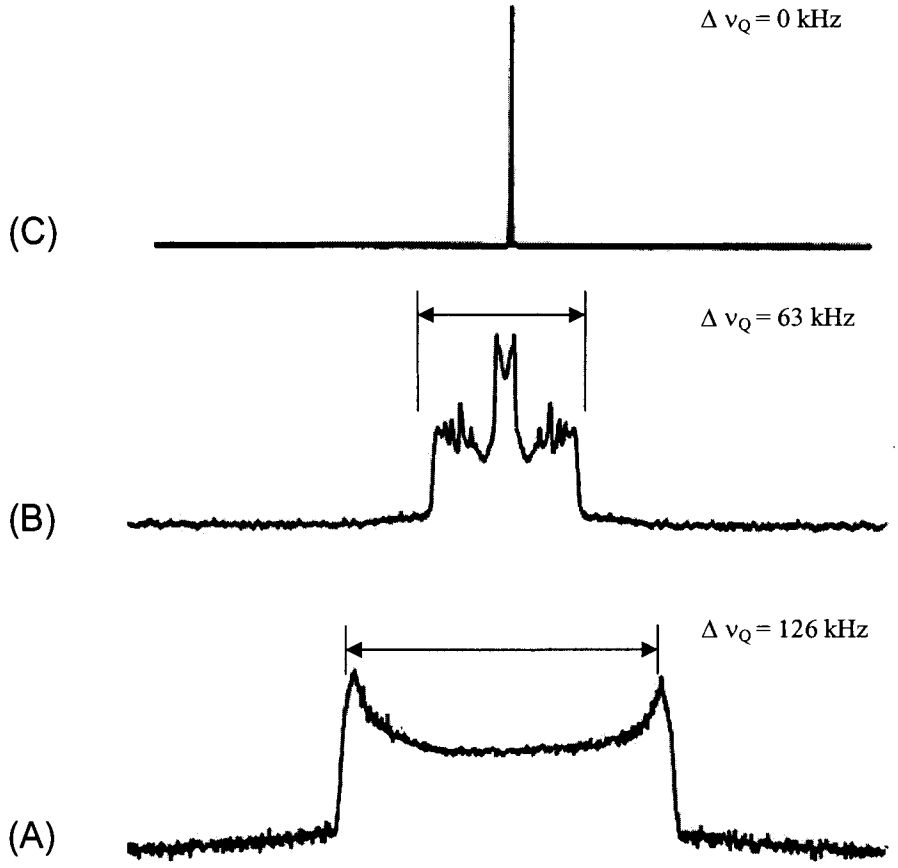

Figure 9: The ^{2}H-NMR spectra representing different phases of chain-deuterated MSC lipids.

(A) Solid phase. Note that the CD_3 signal has been removed; (B) Liquid-crystalline phase; (C) Isotropic phase. [Adapted from E. E. Brief, Simon Fraser University.]

Figure 9A shows the quadrupolar spectrum of a solid phase. It is characterized by a Pake doublet. The quadrupolar splitting (Δ ν_Q) of this Pake doublet is 126 kHz (the immobile deuterated acyl chain on the NMR timescale), and a Pake doublet with a maximum quadrupolar splitting of 40 kHz (the terminal methyl group rotational motion on the NMR timescale) has been removed.

Figure 9B shows the ^{2}H-NMR spectrum of a liquid-crystalline phase. Note that the Pake doublet characterizing the solid phase disappears and a number of Pake doublets with reduced splittings (by at least a factor of two) and superimposed peaks

(conformational disorder of the deuterated acyl chain) appear in the ^{2}H-NMR spectrum of a liquid-crystalline phase. The maximum splitting of these Pake doublets is 63 kHz. The Pake doublet near the centre of the spectrum corresponds to the terminal methyl group.

Figure 9C shows the ^{2}H-NMR spectrum of an isotropic phase. It is characterized by the single peak at the centre of the spectrum at 0 kHz. Because the deuteron movement of the deuterated acyl chain occurs in all orientations in the isotropic phase, the time average of quadrupolar interaction is zero. This gives the single peak at 0 kHz.

By visualizing these spectra, we are able to observe the phase property changes in MSC qualitatively. By analyzing these spectra quantitatively, we are able to deduce the changes in the phase behaviour, profile, composition and transition of individual membrane components and MSC as the whole. The structural integrity of phases, phase domains, lipid domains and MSC as the whole can also be analyzed and determined. A detailed description of this analysis can be found in the Materials and Methods section (Chapter 3).

CHAPTER 3: MATERIALS AND METHODS

3.1 Materials

Palmitic acid (PA) was purchased from Sigma-Aldrich (Sigma grade: ~ 99.0%; Lot 22H0090; Sigma Chemical Co. St. Louise, MO 63178, USA) while deuterated PA (PA-d_{31}) was synthesized previously by Dr. J. L. Thewalt. Both Ceramide 16 (Cer16) and deuterated Ceramide (Cer16-d_{31}) were obtained from Northern Lipids (Unknown grade; Purity tested by TLC prior to use; Lot CER15705101 [Cer16]/Lot CER 15705002 [Cer16-d_{31}]; Northern Lipids Inc. Vancouver, B.C. Canada V6S 2L2). Cholesterol (Chol) was purchased from Sigma-Aldrich (Sigma grade: 99.0+%; Lot 54H8479; Sigma Chemical Co. St. Louis, MO 63178, USA). Isopropyl myristate (IPM) was obtained from Aldrich (98.0+%; Aldrich Chemical Company, Inc. Milwaukee, WI 53201, USA). Myristic acid (MA) was purchased from Sigma-Aldrich (Sigma grade: 99.0% ~ 100.0%; Lot 24H3306; Sigma Chemical Co. St. Louis, MO 63178, USA) and deuterated myristic acid (MA-d_{27}) was purchased from CIL (D: 98.0%; Lot DI-393; Cambridge Isotope Laboratories. Woburn, MA 0180, USA). 2-propanol, Benzene and Methanol were obtained from Caledon (Distilled in glass, Lot 50722 [2-propanol]; Spectro grade, Lot 28322 [Benzene]; Spectro grade, Lot 28062 [Methanol]; Calendon Laboratories Ltd. Georgetown, Ont. Canada L7G 4R9). Chloroform ($CHCl_3$) was purchased from Fisher Scientific (A.C.S.; Lot 043452; Fisher Scientific. Fair Lawn, NJ 07410, USA), whereas deuterated chloroform ($CDCl_3$) was obtained from CIL (D: 99.8%; Lot DLM-7;

Cambridge Isotope Laboratories Inc. Andover, MA 01810-5413, USA). Concentrated sulfuric acid ($H_2SO_{4\ (l)}$, Reagent A.C.S.: 95.0% ~ 98.0%; Lot 199033; Fisher Scientific. Nepean, Ont. Canada K2E 7L6). Sodium chloride (NaCl) was purchased from BHD (A.C.S.: 99.0%; Lot 128680-126773; BHD Inc. Toronto, Ont. Canada M8Z 1K5). Tri-sodium citrate was obtained from BHD (Analytical Reagent: 99.0%; Unknown Lot No.; BHD Inc. Toronto, Ont. Canada M8Z 1K5). EDTA was purchased from BHD (A.C.S.: 99.0% ~ 101.0%; Lot 121213/79469; BHD Inc. Toronto, Ont. Canada M8Z 1K5). Sodium hydroxide (NaOH) was purchased from EM Science (GR A.C.S.; Lot 41171125; EM Science EM Industries, Inc. Gibbstown, NJ 08027, USA). Sodium bicarbonate ($NaHCO_3$) was obtained from EMD (GR A.C.S.; Lot 43164329; EMD Chemicals Inc. Gibbstown, NJ 00827, USA). Deuterium depleted water was purchased from Sigma-Aldrich (Unknown grade: 99.99%; Lot 59F3650; Sigma Chemicals Co. St. Louise, MO 63178, USA). Millipore water was obtained from NANOpure ultrapure water system (Resistance filter: 16.0 Ω ~ 18.0 Ω; Barnstead/Thermolyne. Dubuque, Iowa 52001, USA). Silica-gel Thin-Layer Chromatography (TLC) plates were obtained from EMD (25 TLC aluminum sheets 20 × 20 cm Silica gel 60F234; EMD Chemicals, Inc. Gibbstown, NJ 08027-1296, USA). Drierite was purchased from W. A. Hammond (Anhydrous calcium sulfate, 97.0%, CAS #: 7778-18-9, W. A. Hammond Drierite Company Ltd., Ohio 45385, USA).

3.2 Model stratum corneum preparation

The canonical model stratum corneum (MSC) mixture consists of equimolar Cer16, Chol and PA. For ^{2}H-NMR measurements, either Cer16-d_{31} or PA-d_{31} was used

in each sample, thus the two complementary MSC samples are Cer16-d_{31}:Chol:PA (1:1:1) and Cer16:Chol:PA-d_{31} (1:1:1). In this study, MSC samples were prepared with IPM as a penetration enhancer. As IPM is an organic compound and not water-soluble, it will not dissolve in the buffer, and must be incorporated into the MSC mixture before adding the buffer. MSC mixtures contained either 10% or 1% IPM. The four samples are Cer16-d_{31}:Chol:PA:IPM (3:3:3:1) and (33:33:33:1) and Cer16:Chol:PA-d_{31}:IPM (3:3:3:1) and (33:33:33:1). Each of the four samples had a mass of 200 mg. An MSC sample with 10% IPM-d_{27} with a total mass of 200 mg was also prepared to investigate the behaviour of IPM in MSC. The synthesis of IPM-d_{27} will be outlined in Chapter 4.

During the sample preparation, weighing was carried out before and after each procedure to ensure maximal sublimation of solvent and minimal loss of buffer. Pre-lyophilized lipids and sterols (to remove absorbed atmospheric water during storage) were weighed under minimum atmospheric water absorption by placing four pans of drierite in the balance. MSC samples were co-dissolved in approximately 3.0 ml of Benzene:Methanol (70:30, v/v) and the solution was lyophilized until dry (approximately 6 hours at 7 mtorr). The samples were hydrated with 400 µl of pH 5.2 Citrate buffer (150 mM NaCl, 100 mM Citrate, 4 mM EDTA) and then underwent five heat-vortex/freeze-thaw cycles where each sample was heated in a 90°C bath during which the sample was briefly vortexed 3 ~ 4 times, the sample was then frozen in liquid nitrogen and the process was repeated. After completing the heat-vortex/freeze-thaw procedure, the samples were equilibrated in a 33°C water bath for (up to) three weeks (under $N_{2\,(g)}$). The samples were transferred to clean NMR tubes, sealed with Teflon tape and parafilm to prevent buffer loss, and ^{2}H-NMR spectra were acquired to determine the percentage of

lipids in the solid (crystalline) phase. Once the samples reached 80% solid, the ^{2}H-NMR experiments were carried out from 25°C continuously to 80°C.

For MSC sample preparation and IPM-d_{27} synthesis, the mass discrepancies during weighing of individual membrane lipid components were found to be within 0.03 mg which is equivalent to $\pm$ 0.01 $\times$ 10^{-4} mol. The error in the amount of buffer added was not calculated as an excessive amount was required to hydrate MSC samples; however, automatic pipetters (MANDEL Scientific) were always calibrated prior to use. The variable temperature unit (VTU) in the temperature controller of the ^{2}H-NMR spectrometer was constantly checked to be ensured to read correct temperatures, with estimated error of $\pm$ 0.25°C. A minor VTU fluctuation occurred during the ^{2}H-NMR experiment of the sample 3:3:3:1 Cer16:Chol:PA-d_{31}:IPM (10% IPM). However, the fluctuation was determined and the data were corrected to the precise temperatures.

The pH of the buffer was confirmed with pH paper before hydrating the samples and shown to be within the right pH prior to use. Constant weighing during the sample preparation has shown no major loss of buffer and maximum lyophilization of the lipids. Teflon tape and parafilm have proved themselves to be effective in preventing buffer evaporation during the ^{2}H-NMR experiments at high temperatures. The loss of buffer has been measured after the ^{2}H-NMR experiment and found to be within 5% of the total amount of buffer added.

3.3 Solid-state ^{2}H-NMR spectral acquisition

A 300 MHz Oxford Magnet was used to acquire ^{2}H-NMR spectra, using the quadrupolar echo technique (Davis *et al.*, 1976) with a locally built spectrometer

operating at 46.79 MHz. Spectra were acquired with 1000-10000 repetitions using the two-pulse sequence with a 90° pulse length of 3.95 μs, an interpulse spacing of 40 μs and a dwell time of 2 μs. Two delay times or repetition times (reptime) were used between acquisitions: a short delay (τ_S) 300 ms, and a long delay (τ_L) 50 s (for MSC containing PA-d_{31}) and 30 s (for MSC containing Cer16-d_{31}). Data were collected in quadrature with 8-cyclops phase cycling.

3.4 Apodization

Apodization were applied to the FIDs of the 10% IPM sample (3:3:3:1 Cer16:Chol:PA:IPM-d_{27}) to remove the isotropic truncation effect. The apodization was performed using "Origin 7.0" Graphing Analysis Program, with appropriate parameters to achieve the full removal of the isotropic truncation effect. The apodized FIDs were then Fourier-transformed in "Igor 4.0" Spectral Analysis Program to qualitatively determine the visibility of ^{2}H-NMR spectra and their underlying spectra. For the apodization procedure, please refer to Appendix A-1 and Appendix A-2 for details.

3.5 Calculation of percentage of each phase in FIDs and M_1 values

The percentage of each phase of a deuterated lipid is calculated from the Free Induction Decay (FID) obtained from both long and short time/reptime. For simplicity, we assign the echo height (EH) for the long delay time/reptime (τ_L) FIDs as EH_L, and the echo height (EH) for the short delay time/reptime (τ_S) as EH_S. The % isotropic phase calculation is always done with the τ_L FID. The calculation of the % solid is different for samples with PA-d_{31} and Cer16-d_{31}.

3.5.1 Calculation of % isotropic phase component in model stratum corneum samples

When an isotropic signal was present, the undulating signal in the FID was fit to a Gaussian curve (Figure 10). The % isotropic is given by:

$$\%\,\text{isotropic} = \frac{I_o}{EH_L} \times 100$$

Equation 6: The general formula for calculating the percentage of the isotropic phase component in MSC containing PA-d_{31}, Cer16-d_{31} or IPM-d_{27}

Where I_o is the y-intercept of the Gaussian fit at maximum Echo Height (EH_L) of the τ_L FID.

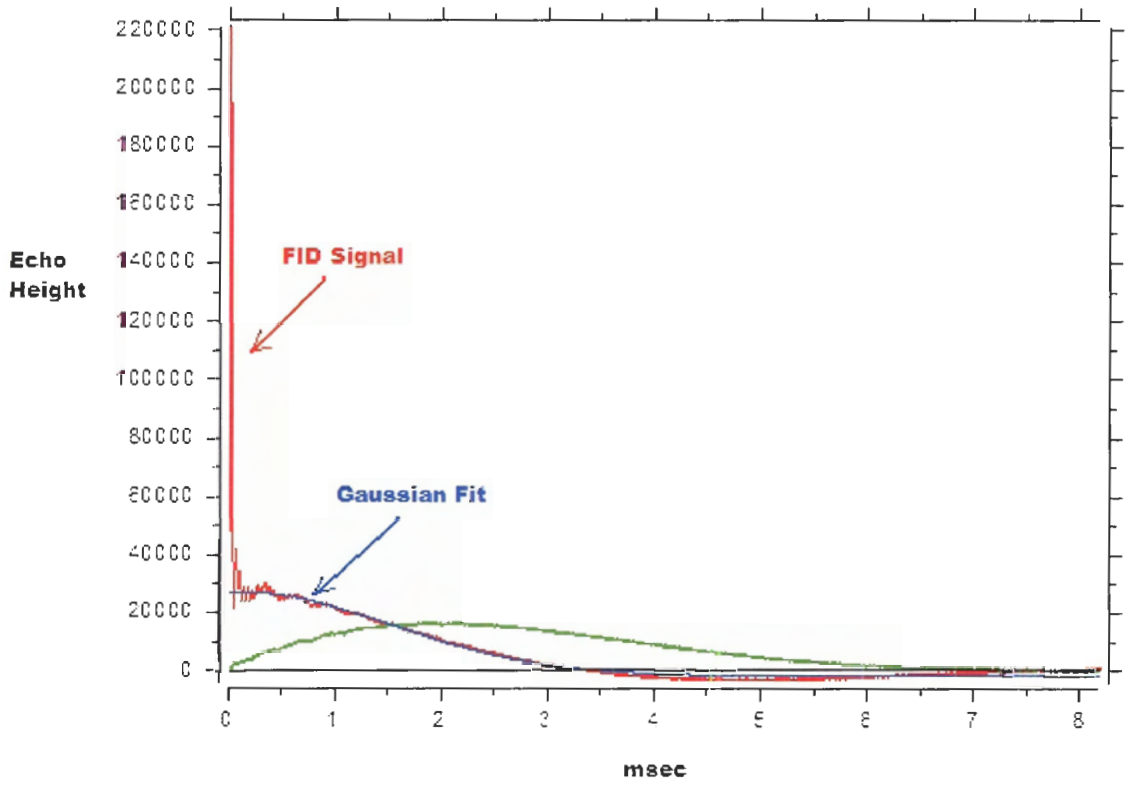

Figure 10: An example of FID with isotropic signal in 1% IPM sample (33:33:33:1 Cer16-d_{31}:Chol:PA:IPM) at 65°C.

The FID is shown in red and the isotropic signal is fit with a Gaussian curve shown in blue. Note that the unit of the y-axis is arbitrary.

"Origin 7.0" Graphing Analysis Program was used with the Gaussian equation:

$$y = y_o + Ae^{-\frac{(x-x_c)^2}{2w^2}}$$

Equation 7: The formula for Gaussian fitting of the isotropic phase signal in an FID

Refer to Appendix A-1 for the analysis procedure.

3.5.2 Calculation of % solid and % liquid-crystalline phase components in model stratum corneum samples

Essentially, the % solid phase component in each sample is given by:

$$\%\ \text{solid} = \frac{(\text{solid})}{(\text{non}-\text{solid})+(\text{solid})} \times 100$$

Equation 8: The general formula for calculating the percentage of the solid phase component in MSC containing PA-d_{31} or Cer16-d_{31}

And the % liquid-crystalline phase component is simply:

$$\%\ \text{liquid - crystalline} = (100\ \%) - (\%\ \text{solid}) - (\%\ \text{isotropic})$$

Equation 9: The general formula for the percentage of the liquid-crystalline phase component in MSC containing PA-d_{31}, Cer16-d_{31} or IPM-d_{27}

3.5.2.1 MSC samples containing PA-d_{31}

The τ_L (50 s) scans acquire the full signal (solid, liquid-crystalline, and isotropic phase components) while the τ_S scans (300 ms) acquire signals from the liquid-crystalline and the isotropic phase components only (non-solid components). In the absence of an isotropic phase signal, it is easy to find % solid by simply comparing the Echo Heights of the τ_L and τ_S FID signals, shown by the equation:

$$\%\ \text{solid} = \left(\frac{n}{n-3}\right)\left(\frac{EH_L - EH_S}{EH_L}\right) \times 100$$

Equation 10: The general formula for calculating the percentage of the solid phase component in MSC containing PA-d_{31} in the absence of isotropic phase signals

Where n is the number of deuterons on the chain; EH_L is the Echo Height of the τ_L FID signals; EH_S is the Echo Height of the τ_S FID signals (Kitson *et al.*, 1994). However, in

the presence of an isotropic phase signal, it is more complicated to calculate the % solid. The % solid of the non-isotropic signals (ordered component) has to be calculated first. The % solid of the non-isotropic signal (% solid*) is given by:

$$\%\ \text{solid}^* = \left(\frac{n}{n-3}\right)\left(\frac{\%\ \text{ord}_L \times EH_L - \%\ \text{ord}_S \times EH_S}{\%\ \text{ord}_L \times EH_L}\right) \times 100$$

Equation 11: The formula for calculating the percentage of the solid phase component in the ordered portion of MSC containing PA-d_{31} in the presence of an isotropic phase signal

Where n is the number of deuterons on the chain and % ord_L and % ord_S are the percentage of ordered signal in τ_L and τ_S FID, respectively. The total percentage of solid is then:

$$\%\ \text{solid} = (\%\ \text{solid}^*) \times (\%\ \text{ord}_L)$$

Equation 12: The formula for calculating the total percentage of the solid phase component in MSC spectra in the presence of an isotropic phase signal

Note that Equation 10, Equation 11 and Equation 12 may not be accurate in calculating the percentage of the PA-d_{31} solid phase component when it approaches zero. In this instance, an examination of the spectra between 63 kHz and 126 kHz is done to confirm that the percentage of the solid phase component is zero.

3.5.2.2 MSC samples containing Cer16-d_{31}

Unlike the PA-d_{31} samples where the τ_S scans acquire signal from non-solid phase components only (to a good approximation), the τ_S scans for Cer16-d_{31} samples include a significant amount of the solid phase component. Therefore, a more complex procedure is

required to calculate the magnitude of the % solid. Since this procedure was developed by Dr. E. E. Brief, we present the derivation of the procedure in the appendix (Appendix A-3). To calculate the % solid for Cer16-d_{31} samples, it is necessary to measure the amount of solid phase signal contributed from the τ_S FID first.

The fractional amount of solid phase signal c in the τ_S FID is found by subtracting the τ_L spectrum multiplied by "c" from the τ_S spectrum, such that the spectrum between 63 kHz and 126 kHz is zero (The resulting spectrum contains contributions from liquid-crystalline and isotropic phase signals only). In the absence of an isotropic phase signal, the % solid of MSC containing Cer16-d_{31} is then given by:

$$\%\,\text{solid} = \left(\frac{n}{n-3-nc}\right)\left(\frac{EH_L - EH_S}{EH_L}\right)\times 100$$

Equation 13: The formula for calculating the total percentage of the solid phase component in MSC containing Cer16-d_{31} in the absence of an isotropic phase signal

If an isotropic phase signal is present, then the % solid of the non-isotropic signals (ordered component) has to be calculated first. The % solid of the non-isotropic signal (% solid*) is given by:

$$\%\,\text{solid}^* = \left(\frac{n}{n-3-nc}\right)\left(\frac{(100\% - \%Iso_L)\cdot(EH_L) - (100\% - \%Iso_S)\cdot(EH_S)}{(100\% - \%Iso_L)\cdot(EH_L)}\right)\times 100$$

Equation 14: The formula for calculating the percentage of the solid phase component in the ordered portion of MSC containing Cer16-d_{31} in the presence of an isotropic phase signal

Where n is the number of deuterons on the chain and % Iso_L and % Iso_S are the percentage of isotropic phase signal in τ_L and τ_S FID, respectively. The total percentage of solid is then given by Equation 12.

"Igor 4.0" Spectral Analysis/Graphing program is used in addition to "Origin 7.0" Graphing Analysis Program to assess % solid in MSC samples containing Cer16-d_{31}. Refer to Appendix A-1 and Appendix A-2 for the procedures and program scripts.

3.5.3 First moment, M_1

Another way to characterize phase changes in the spectrum is by the average spectral width, M_1, which is given by:

$$M_1 = \frac{\sum |\omega| I(\omega)}{\sum I(\omega)}$$

Equation 15: The formula for calculating the value of M_1 (the average spectral width)

Where $I(\omega)$ is the spectral intensity at frequency ω. M_1 is proportional to the order of the spectrum. "Igor 4.0" Spectral Analysis/Graphing program is used to assess M_1 values. Refer to Appendix A-2 for the procedure and program scripts.

3.5.4 Calculation of phase composition of the control and 10% IPM samples

The phase composition of the control (1:1:1 Cer16:Chol:PA) and 10% IPM (3:3:3:1 Cer16:Chol:PA:IPM) samples consisting of individual deuterated membrane components (Cer16-d_{31}, PA-d_{31} and IPM-d_{27}) in different phases were calculated and presented as percentages of total deuterated membrane components. The ratios among

deuterated membrane components in different phases were also computed for each sample. The phase composition and the ratio were calculated from the data obtained at 25°C, 32°C, 50°C and 65°C.

CHAPTER 4: SYNTHESIS OF DEUTERATED ISOPROPYL MYRISTATE

This chapter will be dedicated to describing the microscale synthesis of IPM-d_{27} in detail. There is no commercial or academic procedure available for synthesizing IPM-d_{27}.

IPM-d_{27} was synthesized with the procedures modified from the experimental protocols published for the synthesis of isopentyl acetate (Pavia *et al.*, 1999) and ethyl oleate (Okamoto *et al.*, 1993) and the esterification of myristic acid with propylene (Chakrabarti and Sharma, 1992). Trial syntheses of IPM with non-deuterated myristic acid (MA) were initially performed to formulate the appropriate protocol for the synthesis of IPM-d_{27} with deuterated myristic acid (MA-d_{27}).

4.1.1 Experimental procedure

Excessive amount (0.5 ml) of 2-propanol was added and swirled to mix with pre-lyophilized 0.2092 g of MA (0.2118 g of MA-d_{27}) which was weighed in a 5 ml P-shaped flask under minimum atmospheric water absorption by placing four pans of drierite in the balance. The mixture was added with 1.5 µl of concentrated $H_2SO_{4\ (l)}$ and underwent reflux for 6 ~ 7 hours at 150°C ~ 160°C with periodic examinations of the reaction progress by TLC (Figure 11 and Figure 12). After the reaction reached equilibrium, the reaction mixture underwent workup three times, where the mixture was added with 100 µl of 5% (w/v) $NaHCO_{3\ (aq)}$ ($NaHCO_{3\ (aq)}$ was prepared in Millipore water for the

synthesis of IPM and in deuterium depleted water for the synthesis of IPM-d_{27}) very slowly and drop-wise, stirred and shaked gently/vertically to allow the evolution of $H_{2\ (g)}$ and then, the yellowish ester layer was transferred to a clean 5 ml P-shaped flask. The ester layer underwent distillation for 1 hour at 168°C ~ 170°C (Figure 11) where it turned into a clear or faintly yellow liquid. The final product was transferred to a clean, preweighed vial and weighed to determine the % yield. The purity was confirmed by TLC, ^{1}H- and ^{13}C-NMR spectra.

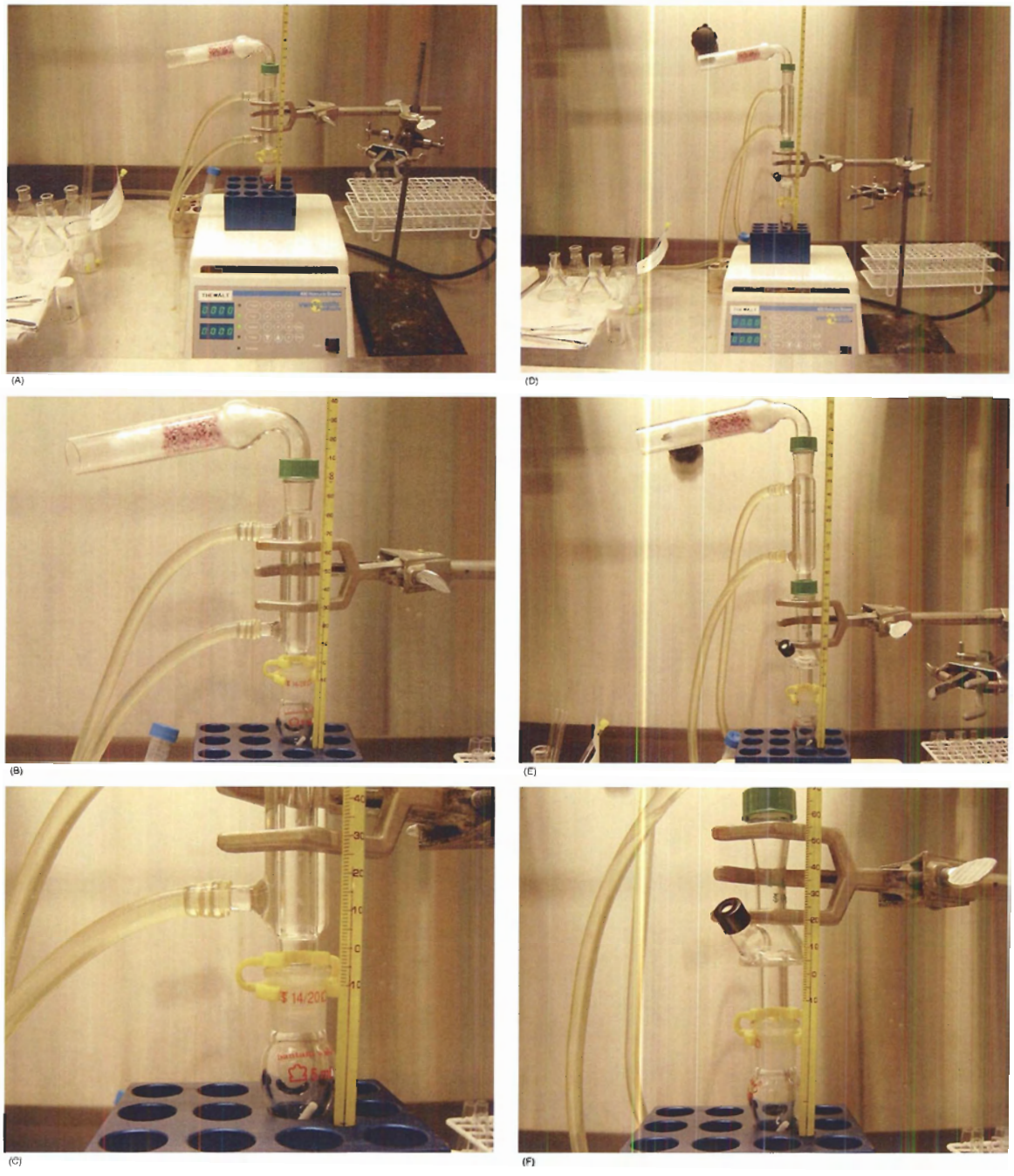

Figure 11: The apparatus setup for the (A) ~ (C) reflux and (D) ~ (F) distillation step of the esterification procedure used to synthesize IPM and IPM-d_{27}.

Progressive magnifications of the image go from the top to the bottom for both apparatus setups. Note the use of a drying tube to prevent odour leakage rather than reagent evaporation.

(A)

(B)

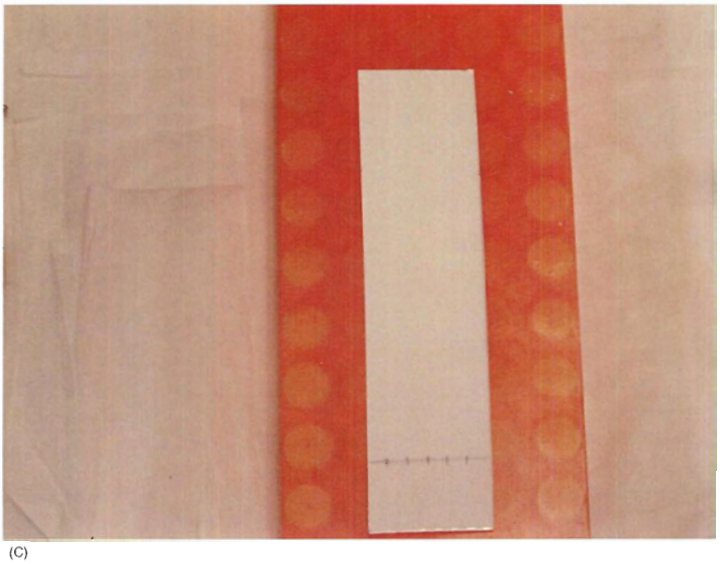

(C)

Figure 12:
TLC apparatus.

(A) TLC solvent chamber (left) and Iodine chamber for TLC plate development (right); (B) Capillary tubes (2 λ diameter) and the spotter for TLC; (C) TLC plate (2.5 cm × 10 cm, width × height).

Figure 13 shows the purity of MA and MA-d_{27} as the starting reagents confirmed by TLC.

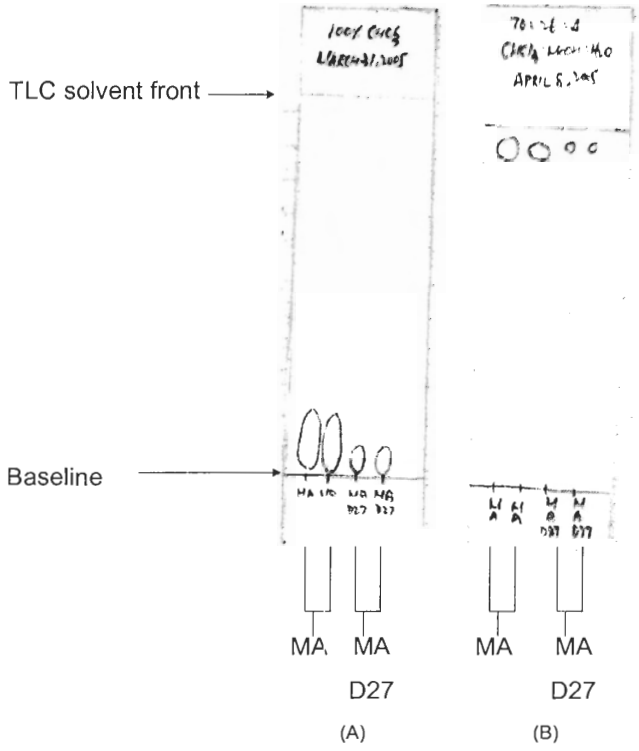

Figure 13: TLC examinations of the purity of MA and MA-d_{27}.

TLC solvent = (A) 100% $CHCl_3$ or (B) 70:26:4 $CHCl_3$:MeOH:H_2O. MA = Myristic acid; MA D27 = Deuterated myristic acid.

4.1.2 TLC

TLC was carried out according to the standard protocol (Pavia *et al.*, 1999) with slight modifications: TLC plates were heated for 20 min at 50°C ~ 60°C prior to use to discard absorbed atmospheric water (Worcestor Polytechnic Institute, 2004). 100% $CHCl_3$ was used as the solvent for the stationary phase. All the standards were freshly prepared in 100% $CHCl_3$.

4.1.3 Reflux products and final products

This section will present the TLC results showing the achievement of reaction equilibrium and purified final products of IPM and IPM-d_{27} syntheses. ^{1}H- and ^{13}C-NMR spectra will also be presented to demonstrate the purity of the synthesized IPM and IPM-d_{27} in comparison with the commercial IPM from Aldrich.

4.1.3.1 TLC Results

Figure 14 shows the periodic TLC examination results of the reaction progress of IPM synthesis. The reaction equilibrium was reached approximately at six to seven hours of reflux, where the estimated quantification of TLC spots showed no evidence of further synthesis of IPM product and depletion of MA (the rate-determining reactant).

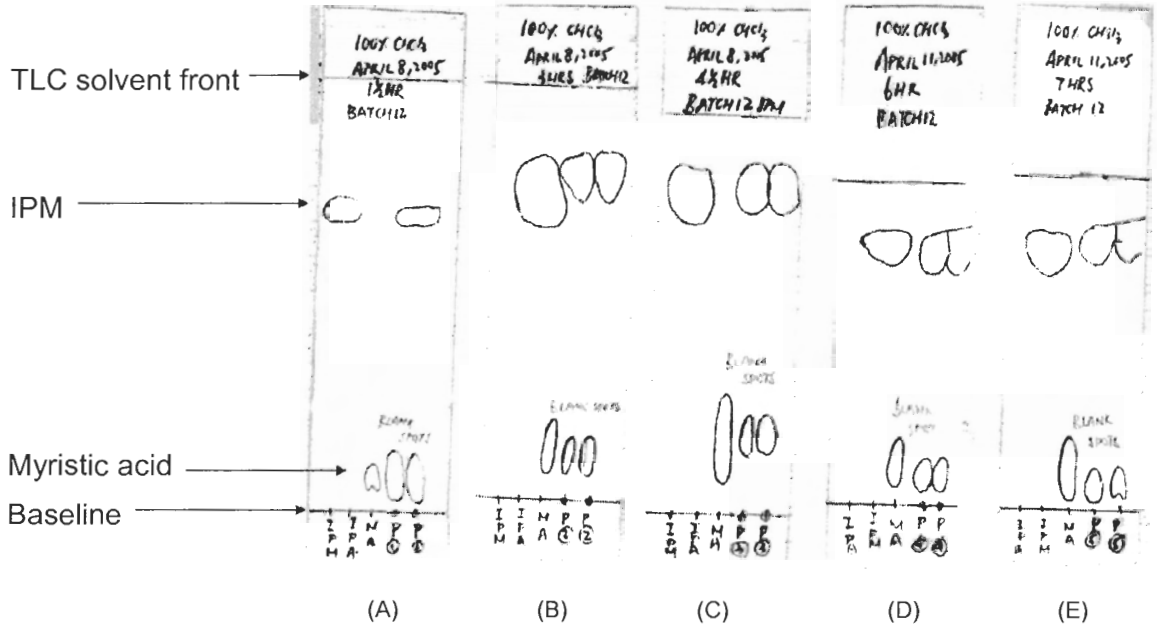

Figure 14: TLC examinations of IPM synthesis.

Results of periodic TLC examinations of the reaction progress at (A) 1.5 hours; (B) 3.0 hours; (C) 4.5 hours; (D) 6.0 hours and (E) 7.0 hours of reflux at 150°C ~ 160°C. TLC solvent = 100% $CHCl_3$; IPM = Isopropyl myristate (from Aldrich); IPA = Isopropyl alcohol (2-propanol); MA = Myristic acid; P = Reflux product.

Figure 15 shows the periodic TLC examination results of the reaction progress of IPM-d_{27} synthesis. Similarly, the reaction equilibrium was reached approximately at six hours of reflux, where the estimated quantification of TLC spots showed no evidence of further synthesis of IPM product and depletion of MA-d_{27} (the rate-determining reactant).

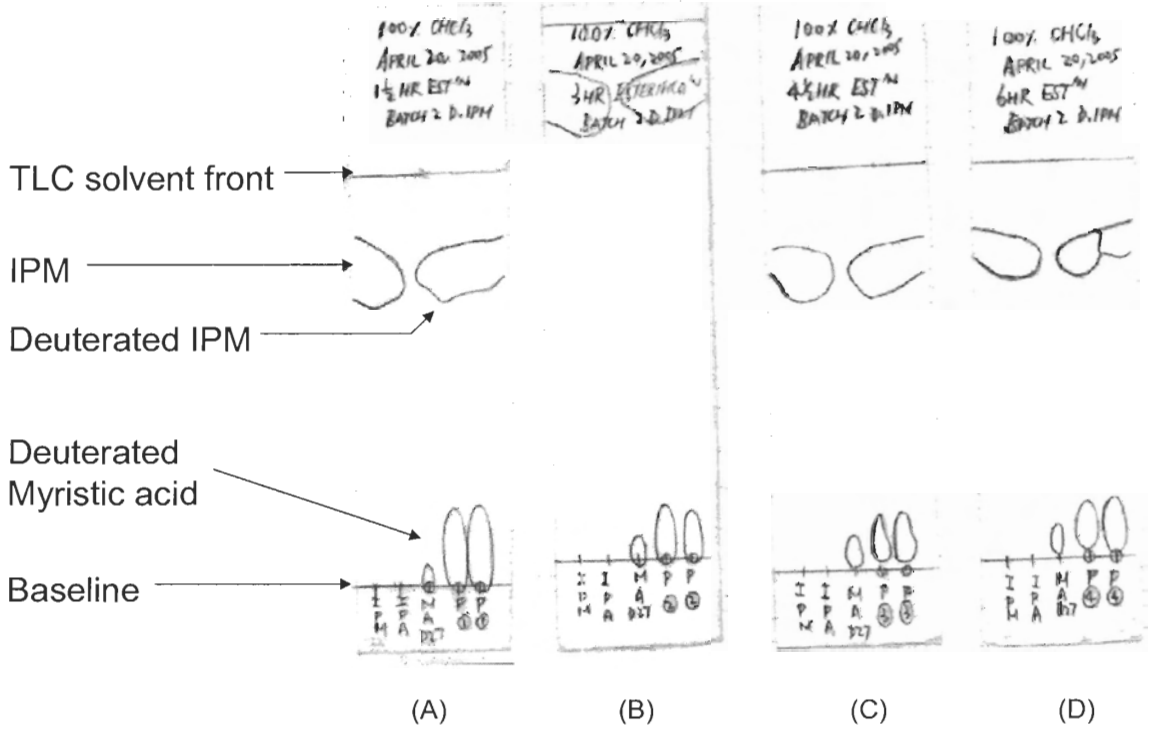

Figure 15: TLC examinations of IPM-d_{27} synthesis.

Results of periodic TLC examinations of the reaction progress at (A) 1.5 hours; (B) 3.0 hours; (C) 4.5 hours and (D) 6.0 hours of reflux at 150°C ~ 160°C. TLC solvent = 100% $CHCl_3$; IPM = Isopropyl myristate (from Aldrich); IPA = Isopropyl alcohol (2-propanol); MA-D27 = Deuterated myristic acid; P = Reflux product.

Figure 16 shows the TLC results of the final purified products of IPM and IPM-d_{27} syntheses. No residual MA or MA-d_{27} spot demonstrates that the workup was successful in isolating the esters and the final product purity is confirmed.

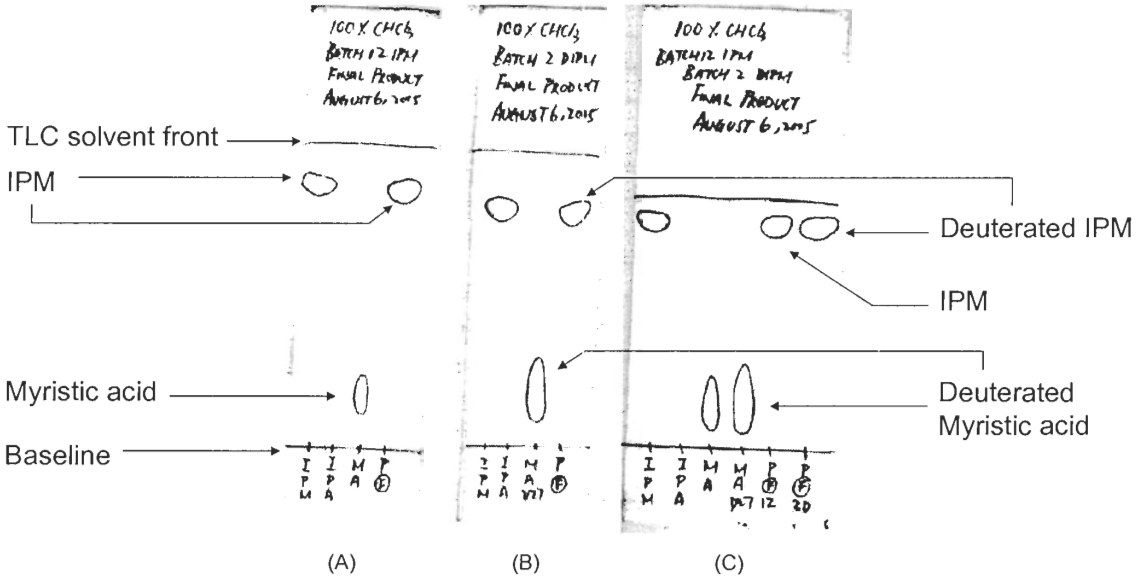

Figure 16: TLC examinations of final products of IPM and IPM-d_{27} syntheses.

TLC results of the final product from (A) IPM synthesis; (B) IPM-d_{27} synthesis and (C) comparison between IPM and IPM-d_{27} synthesis products. TLC solvent = 100% $CHCl_3$; IPM = Isopropyl myristate; IPA = Isopropyl alcohol (2-propanol); MA = Myristic acid; MA-D27 = Deuterated myristic acid; P = Final product.

4.1.3.2 ^{1}H- and ^{13}C-NMR spectra of the commercial and synthesized IPM

Figure 17 shows the ^{1}H- and ^{13}C-NMR spectra of commercial IPA, MA and IPM purchased from Caledon and Sigma-Aldrich. The spectra were obtained from Sigma-Aldrich website (Sigma-Aldrich Co., 2005). Figure 18 shows the ^{1}H- and ^{13}C-NMR spectra of the synthesized IPM. The ^{1}H- and ^{13}C-NMR spectra of the synthesized IPM are consistent with those of the commercial IPM, with correct splittings and locations (chemical shift) of the peaks. Note that the triplet at 77.236 ppm of the ^{13}C-NMR spectra is characteristic of products from Sigma-Aldrich (Figure 17). A tiny singlet peak at 2.174 ppm in the ^{1}H-NMR spectrum of the synthesized IPM is not visible in that of the commercial IPM. The singlets at 7.262 ppm (^{1}H-NMR) and at 173.703 ppm (^{13}C-NMR) of the synthesized IPM are the reference $CDCl_3$ peaks.

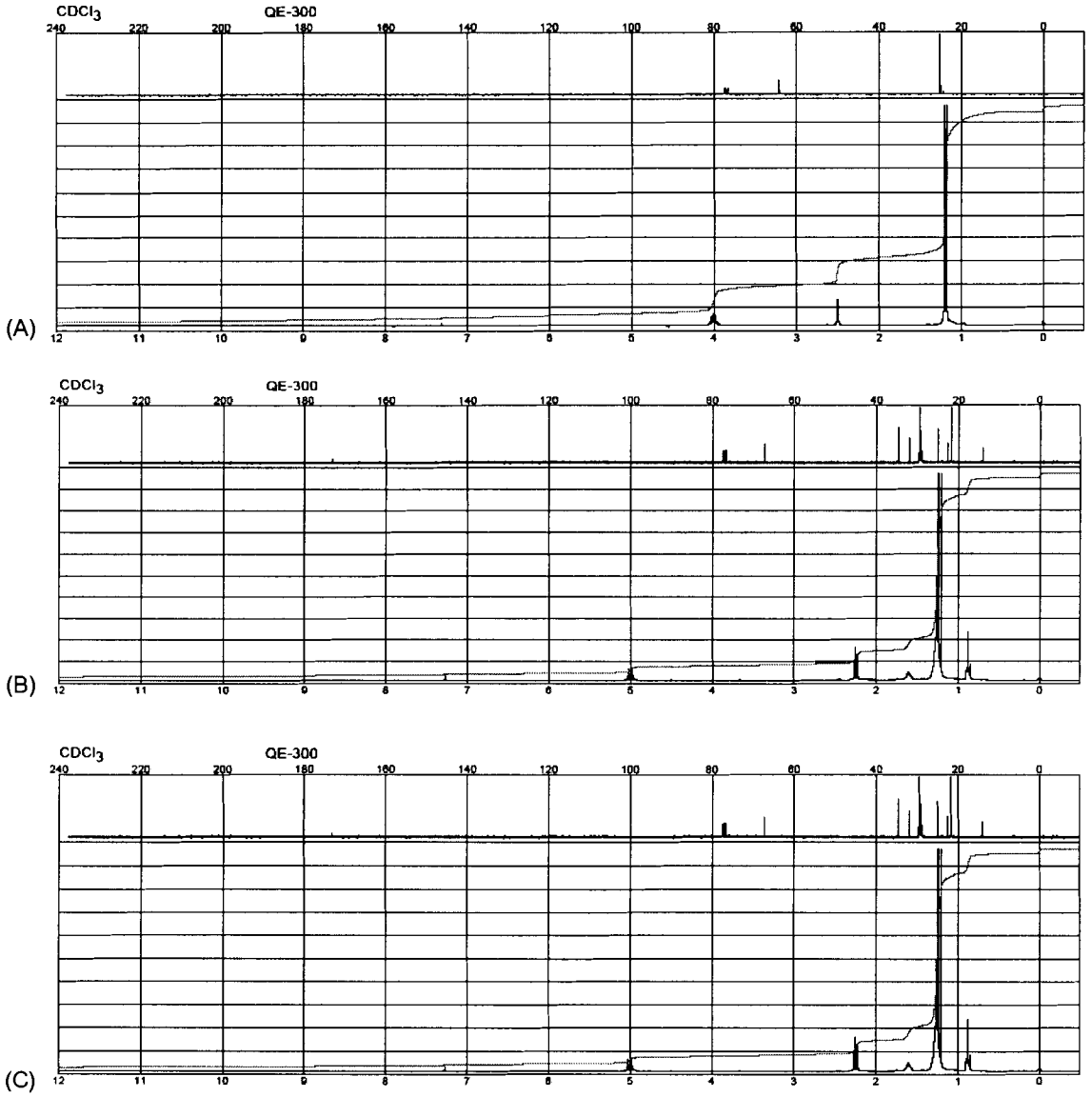

Figure 17: ^{1}H- and ^{13}C-NMR spectra of (A) IPA; (B) MA and (C) IPM obtained from Sigma-Aldrich (Sigma-Aldrich Co., 2005).

^{1}H-NMR spectra are located at the bottom panel and ^{13}C-NMR spectra are located on the top panel. NMR solvent = $CDCl_3$; Chemical shift unit = ppm. Note the triplet peak at ~ 77.000 ppm in all ^{13}C-NMR spectra which is characteristic of Sigma-Aldrich products.

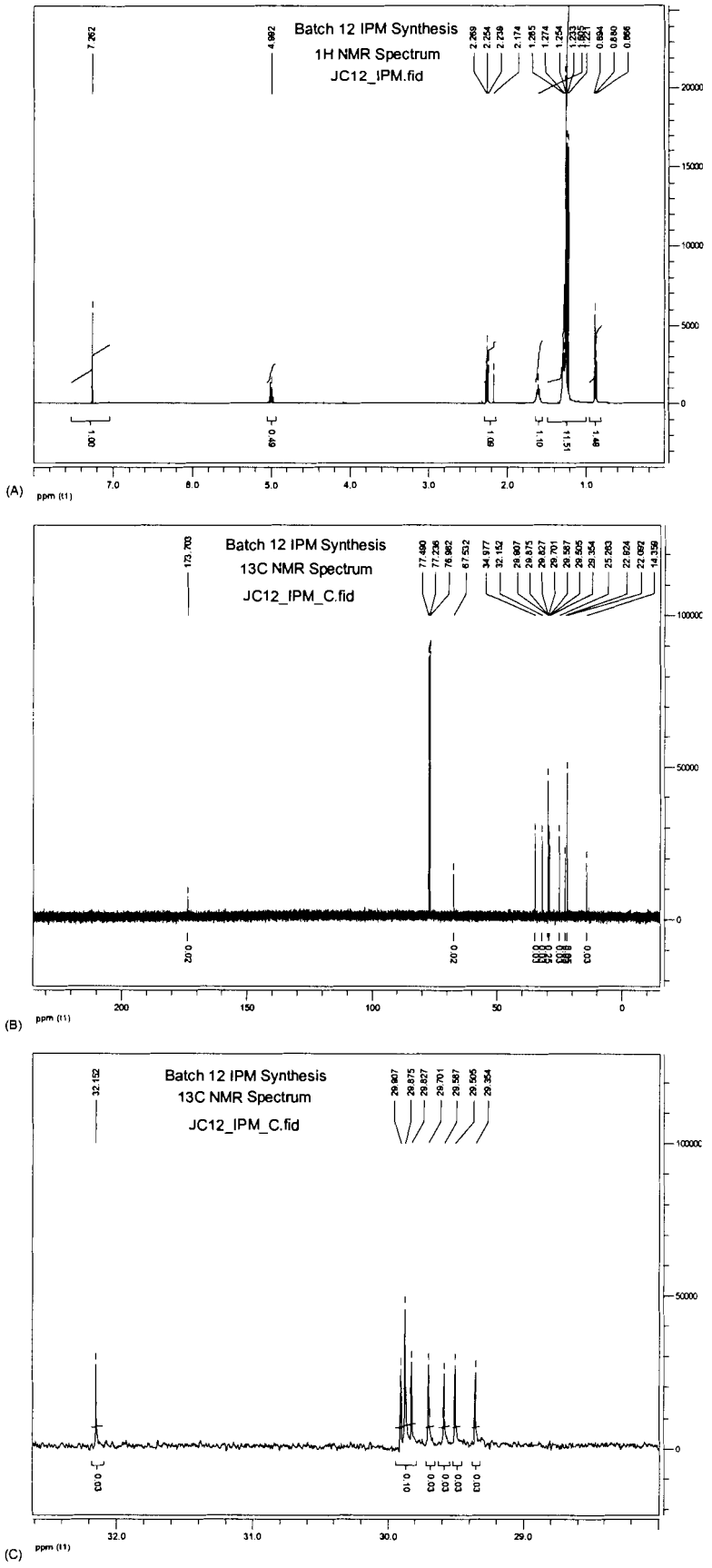

Figure 18:
(A) ^{1}H-NMR, (B) ^{13}C-NMR and (C) enlarged ^{13}C-NMR (28.0 ppm ~ 32.6 ppm) spectra of synthesized IPM.

Concentration = 10.0 mg/ml $CDCl_3$. All spectra have the peaks with the same chemical shifts and splittings corresponding to the peaks of ^{1}H- and ^{13}C-NMR spectra obtained from commercial IPM (Aldrich). Note the triplet peak at ~ 77.000 ppm in the ^{13}C-NMR spectrum which is characteristic of Sigma-Aldrich products.

4.1.3.3 ^{1}H- and ^{13}C-NMR spectra of the synthesized IPM-d_{27}

Figure 19 shows the ^{1}H- and ^{13}C-NMR spectra of commercial MA-d_{27} purchased from Cambridge Isotope Laboratories. Figure 20 shows the ^{1}H- and ^{13}C-NMR spectra of synthesized IPM-d_{27}. There is no ^{1}H signal from acyl chains of MA-d_{27} and IPM-d_{27} since they are deuterated (deuterons should not show signals in a ^{1}H-NMR spectrum), and the ^{1}H signals come from the isopropyl group only (1.226 ppm, Figure 19A; 1.232 ppm, Figure 20A). Similarly, the ^{13}C signals come from only the isopropyl group (22.093 ppm and 67.492 ppm, Figure 20B), where no ^{13}C signal comes from the deuterated acyl chain due to the deuteron splitting effect (Reusch, 2004). These suggest the successful esterification of the deuterated myristic acid acyl chain to the non-deuterated isopropyl alcohol group. Note that the triplet at 77.441 ppm of the ^{13}C-NMR spectra is characteristic of products from Sigma-Aldrich (Figure 17 and Figure 20B). The singlets at 7.262 ppm (^{1}H-NMR) and at 173.703 ppm (^{13}C-NMR, not visible due to spectral noise) of the synthesized IPM-d_{27} are the reference $CDCl_3$ peak.

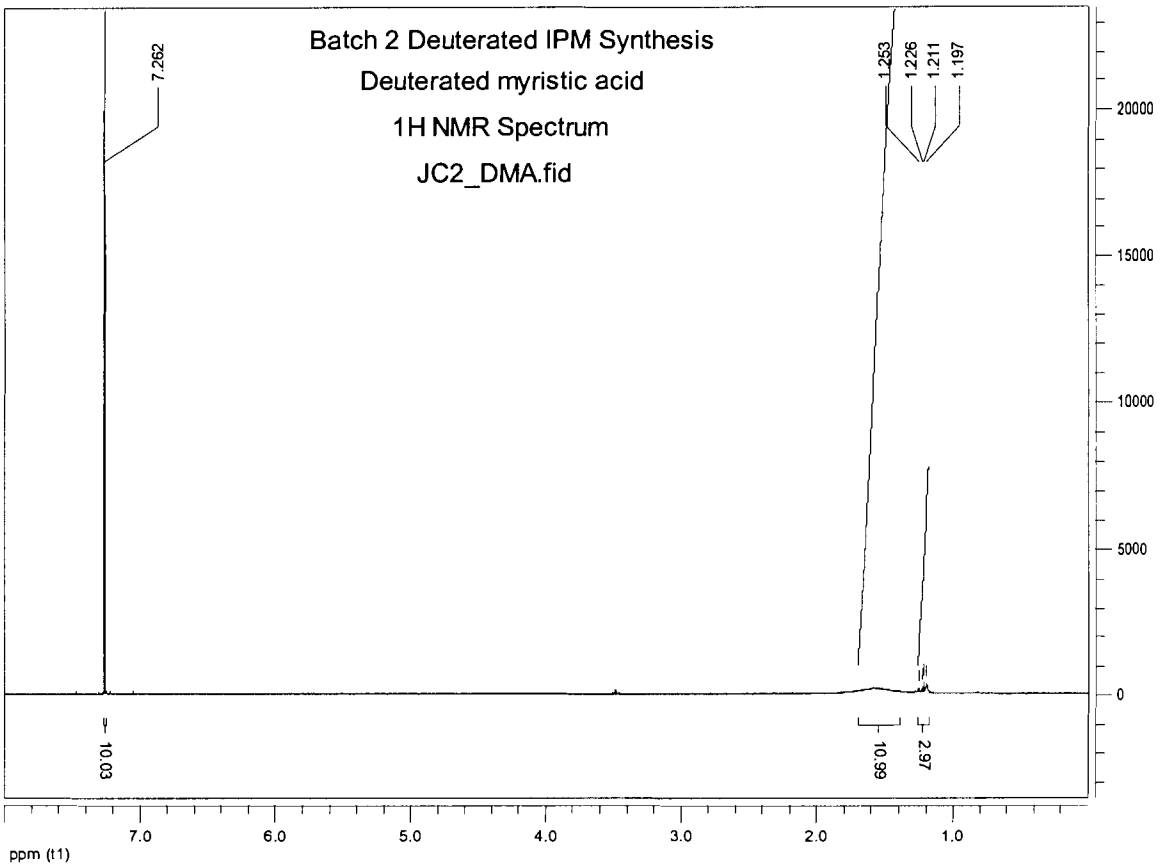

Figure 19: ^{1}H-NMR spectrum of commercial MA-d_{27} (Cambridge Isotope Laboratories).

Concentration = 50.0 mg/ml $CDCl_3$. ^{1}H signals only come from the isopropyl group since the acyl chain is deuterated.

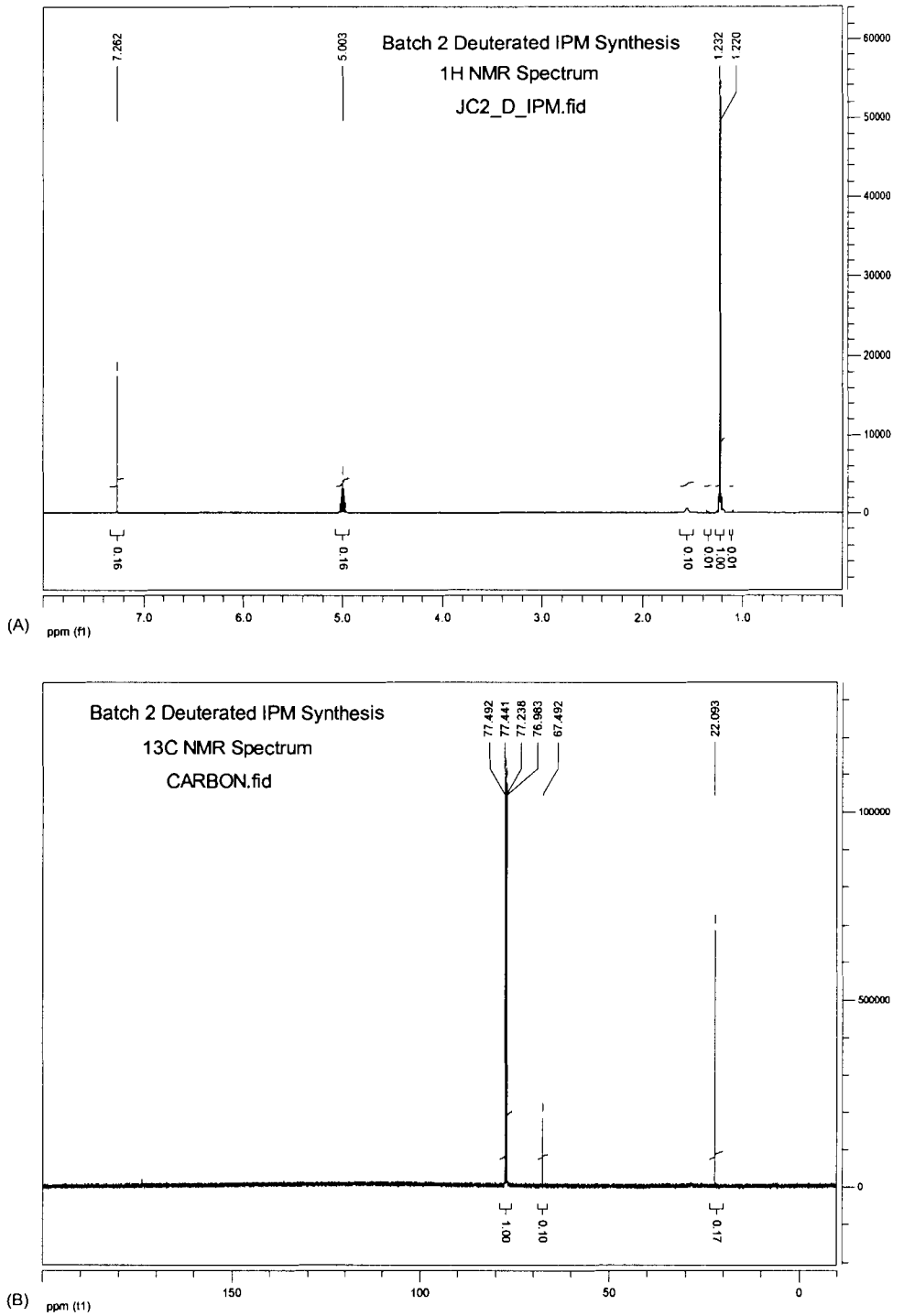

Figure 20: (A) ^{1}H- and (B) ^{13}C-NMR spectra of synthesized IPM-d_{27}.

Concentration = 50.0 mg/ml $CDCl_3$. ^{1}H signals only come from the isopropyl group since the acyl chain is deuterated. Both spectra have the peaks with the same chemical shifts and splittings corresponding to the peaks of ^{1}H- and ^{13}C-NMR spectra obtained from commercial IPM (Aldrich). Note the triplet peak at ~ 77.000 ppm in the ^{13}C-NMR spectrum which is characteristic of Sigma-Aldrich products.

4.1.3.4 ^{1}H- and ^{13}C-NMR data comparison among commercial IPM, synthesized IPM and IPM-d_{27}

This section will focus on ^{1}H- and ^{13}C-NMR data comparison among commercial IPM (Aldrich), synthesized IPM and IPM-d_{27}. Peaks will be assigned to individual functional groups of the structure, while chemical shifts and area integrations will be listed in tables.

Figure 21 shows the ^{1}H-NMR spectra of IPM from Spectral Data Base System, SDBS (Saito *et al.*, 2005; SDBS, 2005), synthesized IPM and IPM-d_{27}, and commercial MA-d_{27} from CIL. Figure 22 shows the structure of IPM and assignment of hydrogen (H's) according to SDBS which was used as the basis for assigning ^{1}H-NMR peaks of IPM, IPM-d_{27} and MA-d_{27}. Table 1 lists the ^{1}H-NMR data including chemical shifts and integration values for comparison.

Figure 21: ^{1}H-NMR spectrum of the commercial IPM/MA-d_{27} and the synthesized IPM/IPM-d_{27}.

(A) IPM from Spectral Data Base System (Saito *et al.*, 2005; SDBS, 2005); (B) synthesized IPM; (C) synthesized IPM-d_{27} and (D) commercial MA-d_{27} (CIL). Concentration = (A) 0.1 mg/ml $CDCl_3$; (B) 10 mg/ml $CDCl_3$; (C) and (D) 50 mg/ml $CDCl_3$.

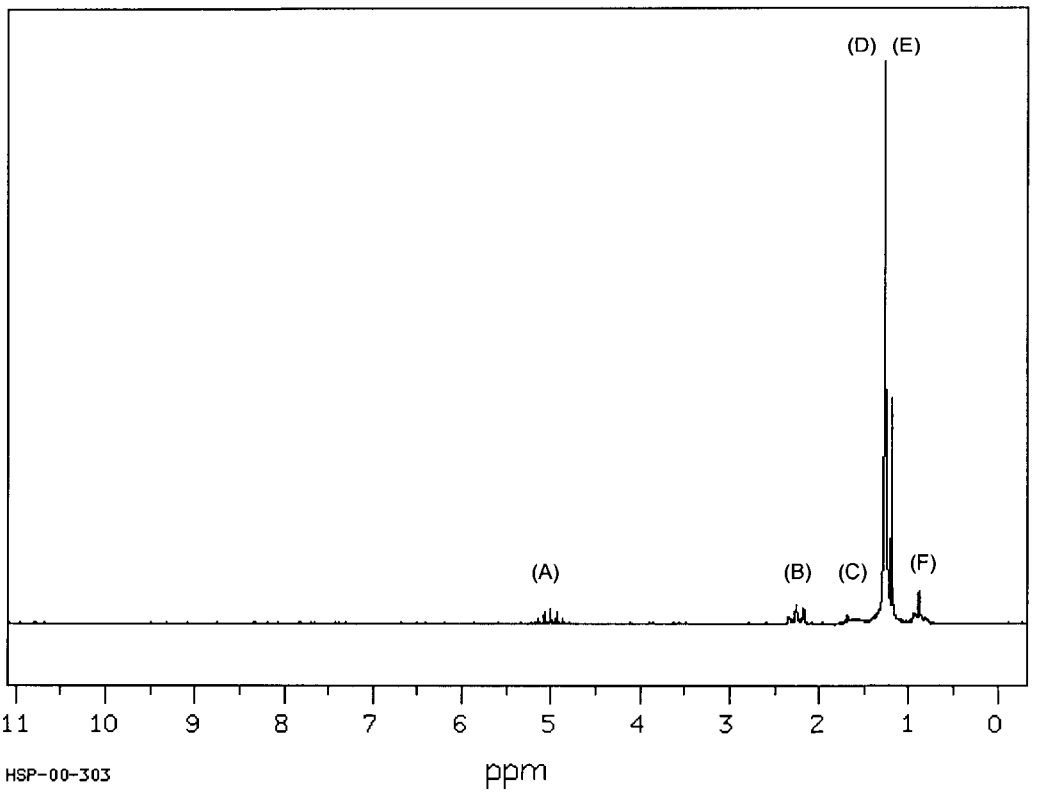
(D) (E)
(A)
(B)
(C)
(F)
11
10
9
8
7
6
5
4
3
2
1
0
ppm
HSP-00-303

(A)

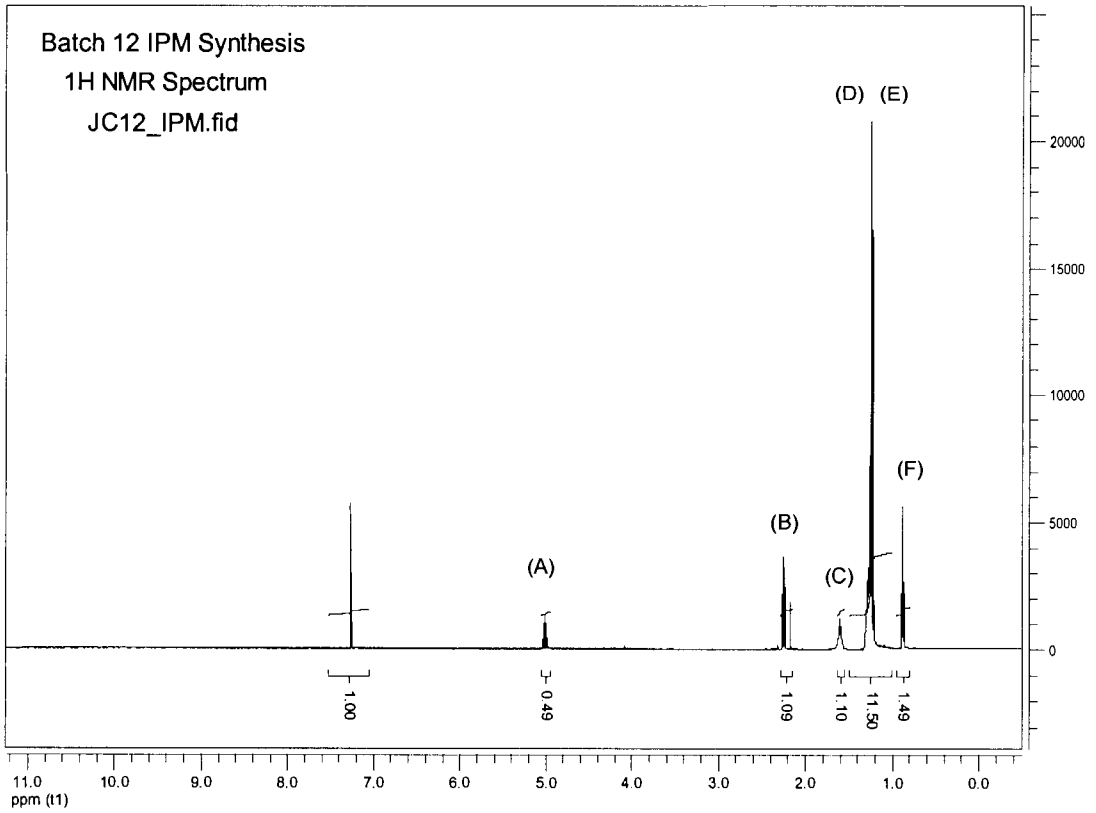
Batch 12 IPM Synthesis
1H NMR Spectrum
JC12_IPM.fid
(D) (E)
(F)
(B)
(A)
(C)
20000
15000
10000
5000
0
1.00
0.49
1.09
1.10
11.50
1.49
11.0
10.0
9.0
8.0
7.0
6.0
5.0
4.0
3.0
2.0
1.0
0.0
ppm (t1)

(B)

(C)

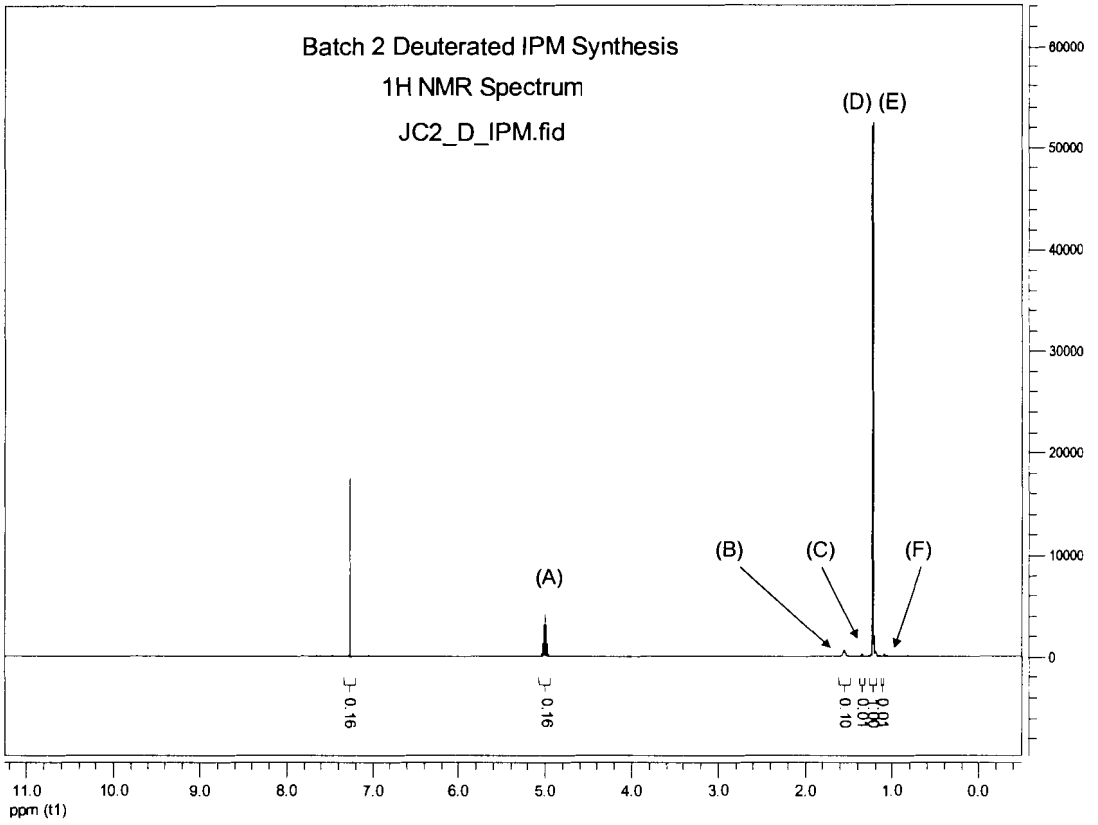
Batch 2 Deuterated IPM Synthesis
1H NMR Spectrum
JC2_D_IPM.fid
(A)
(B)
(C)
(D) (E)
(F)
0.16
0.16
0.10
11.0
10.0
9.0
8.0
7.0
6.0
5.0
4.0
3.0
2.0
1.0
0.0
ppm (t1)
60000
50000
40000
30000
20000
10000
0

(D)

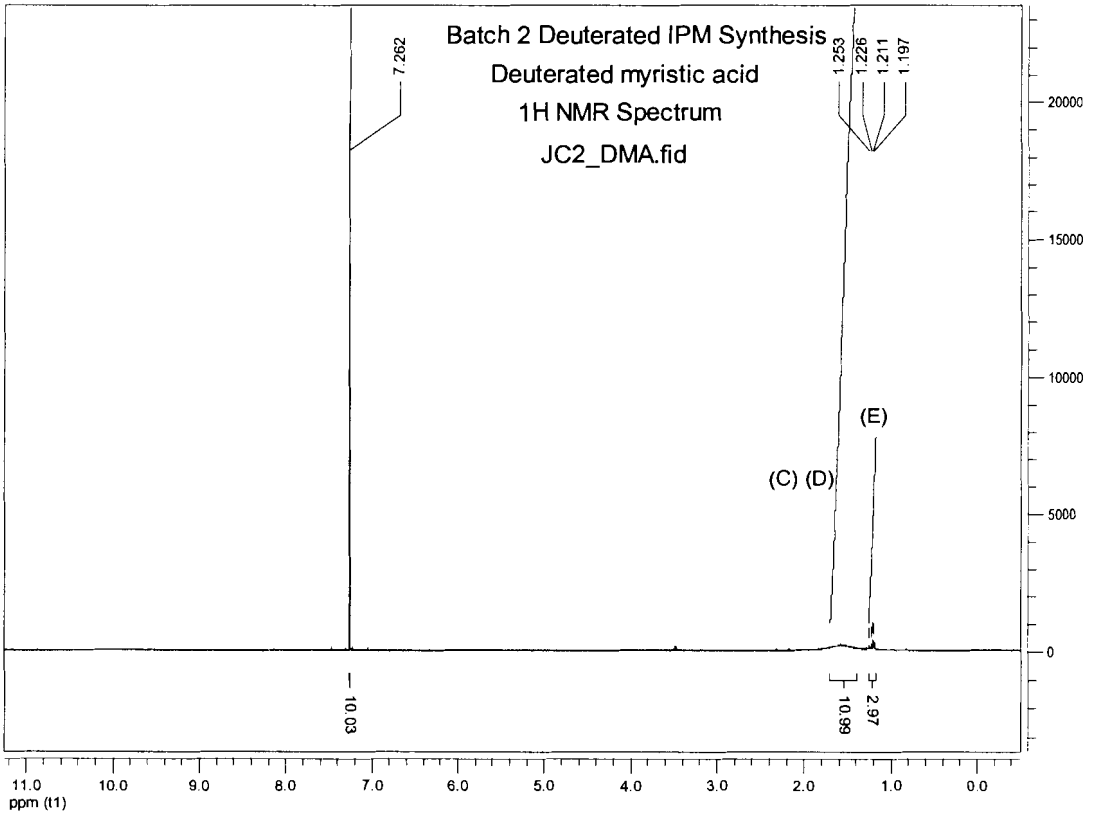
Batch 2 Deuterated IPM Synthesis
Deuterated myristic acid
1H NMR Spectrum
JC2_DMA.fid
7.262
1.253
1.226
1.211
1.197
(C) (D)
(E)
10.03
10.09
2.97
11.0
10.0
9.0
8.0
7.0
6.0
5.0
4.0
3.0
2.0
1.0
0.0
ppm (t1)
20000
15000
10000
5000
0

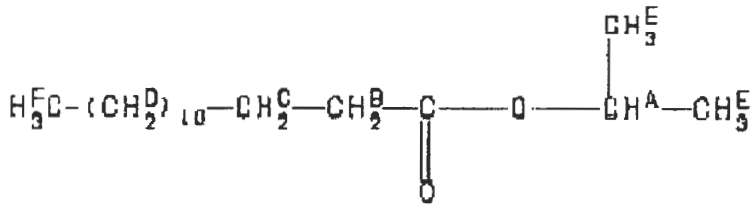

Figure 22: Assignment of ^{1}H-NMR peaks according to Spectral Data Base System (Saito *et al.*, 2005; SDBS, 2005).

Table 1: ^{1}H-NMR data comparison among SDBS data (Saito *et al.*, 2005; SDBS, 2005), synthesized IPM, IPM-d_{27} and MA-d_{27}.

	SDBS Data (IPM)			*Batch 12 IPM*			*Batch 2 IPM-d_{27}*			*MA-d_{27}*		
Assign.	Shift (ppm)	Int.	# H's	Shift (ppm)	Int.	# H's	Shift (ppm)	Int.	# H's	Shift (ppm)	Int.	# H's
A	5.003	28.00	1	4.992	0.49	1	5.003	0.16	1	—	—	—
B	2.250	33.00	1	2.254	1.09	2	—	0.10	0	—	—	—
C	1.590	28.00	1	1.605	1.10	2	—	0.01	0	—	10.99	22
D	1.260	1000.00	36	1.254	11.51	23	—	1.00	0	—		
E	1.240	401.00	14	1.233			1.232		6	1.226	2.97	6
F	0.890	58.00	2	0.880	1.49	3	—	0.01	0	—	—	—

**Assign. = Assignment
**Int. = Integration
**H = Hydrogen

All of SDBS data, synthesized IPM and IPM-d_{27} have very similar chemical shifts, with negligible offsets in few assignments of peaks. Attention should be paid to IPM-d_{27} data which show ^{1}H signals from only isopropyl group (Assign. A, D & E). The integrations of area were used to calculate the number of H's in each peak. The number of H's is correct for all samples according to the assignments in Figure 22, except some inaccuracies in the SDBS data.

Figure 23 shows the ^{13}C-NMR spectra of IPM from SDBS (Saito *et al.*, 2005; SDBS, 2005), synthesized IPM and IPM-d_{27}. Figure 24 shows the structure of IPM and assignment of carbons (C's) according to SDBS which was used as the basis for

assigning ^{13}C-NMR peaks of IPM and IPM-d_{27}. Table 2 lists the ^{1}H-NMR data including chemical shifts and integration values for comparison.

Figure 23: ^{13}C-NMR spectrum of (A) IPM from Spectral Data Base System (Saito *et al.*, 2005; SDBS, 2005); (B) synthesized IPM and (C) synthesized IPM-d_{27}.

Concentration = (A) 0.1 mg/ml $CDCl_3$; (B) 10 mg/ml $CDCl_3$; (C) 50 mg/ml $CDCl_3$.

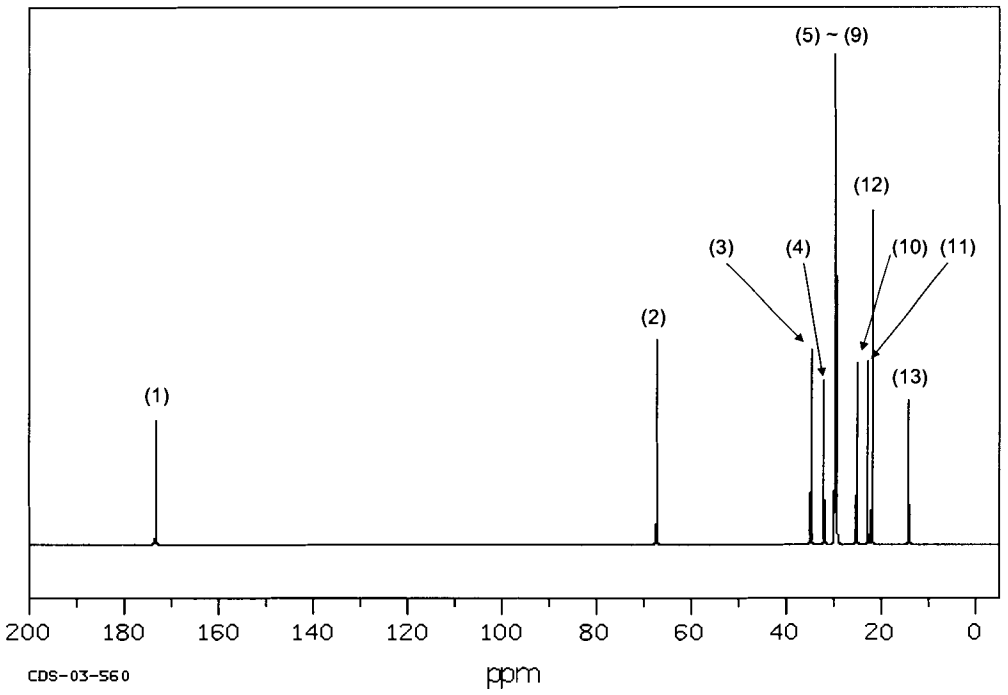
(5) ~ (9)
(12)
(3)
(4)
(10)
(11)
(2)
(13)
(1)
200
180
160
140
120
100
80
60
40
20
0
CDS-03-560
ppm

(A)

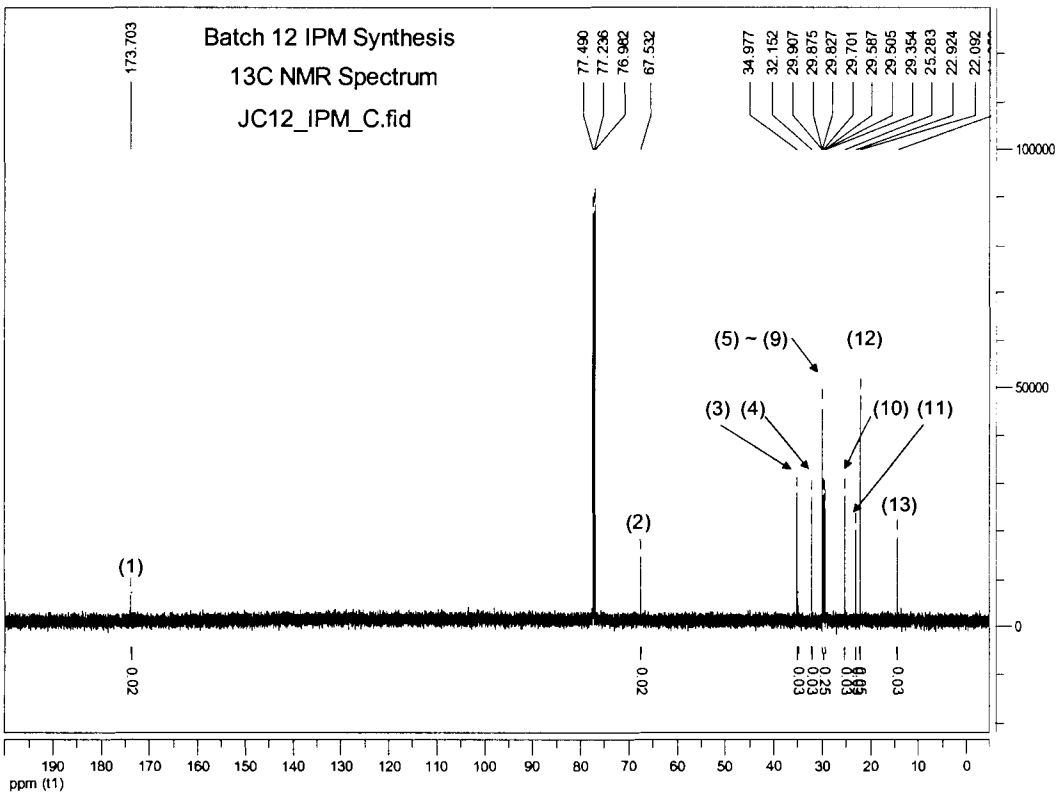
Batch 12 IPM Synthesis
13C NMR Spectrum
JC12_IPM_C.fid
173.703
77.490
77.236
76.982
67.532
34.977
32.152
29.907
29.875
29.827
29.701
29.587
29.505
29.354
25.283
22.924
22.092
100000
50000
0
(5) ~ (9)
(12)
(3) (4)
(10) (11)
(13)
(2)
(1)
0.02
0.02
0.03
190
180
170
160
150
140
130
120
110
100
90
80
70
60
50
40
30
20
10
0
ppm (t1)

(B)

(C)

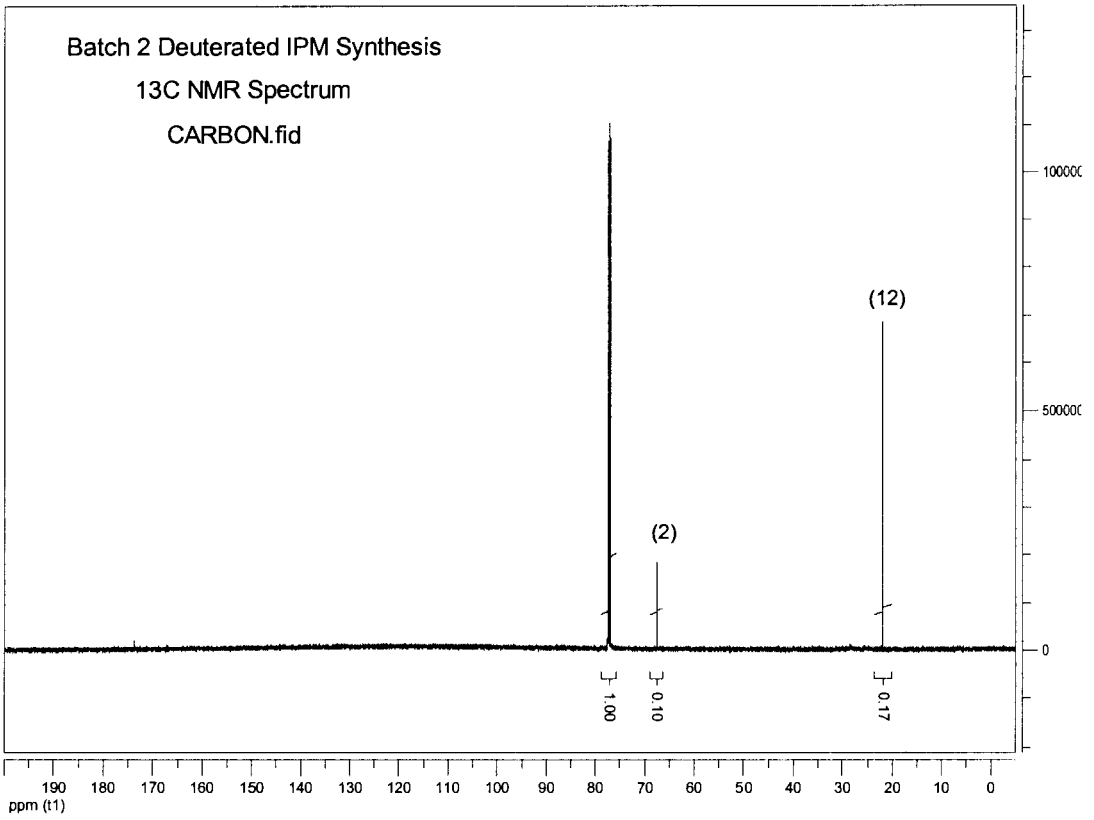
Batch 2 Deuterated IPM Synthesis
13C NMR Spectrum
CARBON.fid
(12)
(2)
1.00
0.10
0.17
100000
500000
0
190 180 170 160 150 140 130 120 110 100 90 80 70 60 50 40 30 20 10 0
ppm (t1)

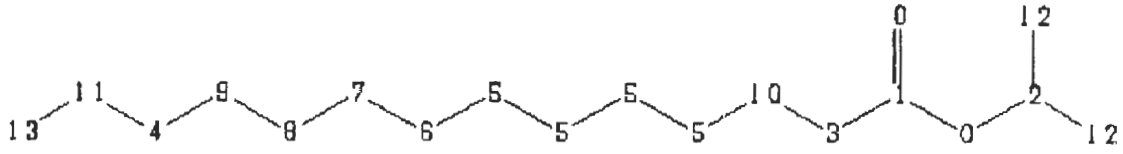

Figure 24: Assignment of ^{13}C-NMR peaks according to Spectral Data Base System (Saito *et al.*, 2005; SDBS, 2005).

Table 2: ^{13}C-NMR data comparison among SDBS data (Saito *et al.*, 2005; SDBS, 2005), synthesized IPM, IPM-d_{27} and MA-d_{27}.

	SDBS Data (IPM)			*Batch 12 IPM*			*Batch 2 IPM-d_{27}*		
Assign.	Shift (ppm)	Int.	# C's	Shift (ppm)	Int.	# C's	Shift (ppm)	Int.	# C's
1	173.31	250	1.00	173.703	0.02	1	—	—	0
2	67.26	420	1.68	67.532	0.02	1	67.492	0.10	1
3	34.77	400	1.60	34.977	0.03	1	—	—	0
4	32.00	335	1.34	32.152	0.03	1	—	—	0
*5**	29.73	1000	4.00	29.875	0.10	3	—	—	0
*6**	29.55	450	1.80	29.701	0.03	1	—	—	0
*7**	29.43	500	2.00	29.587	0.03	1	—	—	0
*8**	29.37	395	1.58	29.505	0.03	1	—	—	0
9	29.22	415	1.66	29.354	0.03	1	—	—	0
10	25.13	370	1.48	25.283	0.03	1	—	—	0
11	22.75	375	1.50	22.924	0.03	1	—	—	0
12	21.88	685	2.74	22.092	0.05	2	22.093	0.17	2
13	14.12	295	1.18	14.359	0.03	1	—	—	0

**Assign. = Assignment
**Int. = Integration
**H = Hydrogen

All of SDBS data, synthesized IPM and IPM-d_{27} have very similar chemical shifts, with negligible offsets in few assignments of peaks. Attention should be paid to IPM-d_{27} data which show ^{13}C signals from the isopropyl group only (Assign. 2 & 12). The integrations of area were used to calculate the number of C's in each peak. The

number of C's is correct for all samples according to the assignments in Figure 24, except some inaccuracies in the SDBS data, and a slight offset in the Batch 12 IPM product data (Assign. 5*).

Through physical examinations, the synthesized IPM has the same odour and colour as the commercial IPM. The odour of the synthesized IPM-d_{27} is slightly different from IPM, but this would indicate the difference in the synthesized deuterated product. Due to the deuteron splitting effect, ^{13}C-NMR spectrum could not be obtained for MA-d_{27}, even with a very large amount of sample ($\geq$ 50 mg/ml $CDCl_3$) and very long acquisition time ($\geq$ 72 hours).

CHAPTER 5: RESULTS

This chapter will present the ^{2}H-NMR results and observations on the effect of IPM as a CPE on MSC in this model study. In this study, individual membrane components, including Cer16, PA and IPM, were deuterated to observe their changes in order parameter (indicated by M_1) and phase behaviour, phase profile and phase composition in MSC as functions of temperature and IPM concentration. ^{2}H-NMR spectra were analyzed to determine the proportions of ^{2}H signals from different lipid phases as functions of temperature and IPM concentration.

This chapter will be divided into three major sections. Each section will present the results obtained from MSC containing a specific deuterated membrane component, namely PA-d_{31}, Cer16-d_{31} or IPM-d_{27}. In each section, the ^{2}H-NMR spectra will be shown first to inform the reader of the significant changes in ^{2}H signals obtained from the deuterated membrane component as a function of IPM concentration at specific temperatures. Then, changes in M_1 and in the proportions of individual phases will be shown to demonstrate the overall order and phase behaviour of the deuterated membrane component as a function of temperature at specific IPM concentrations. The individual phase changes of the deuterated membrane component will also be presented as a function of IPM concentration at specific temperatures. Finally, the phase profile of the deuterated membrane component as a function of temperature at specific IPM concentrations will be displayed.

At the end of this chapter, the phase composition of all deuterated membrane components in the control and 10% IPM samples will be illustrated in pie graphs to show the reader the phase composition changes of MSC with or without IPM at specific temperatures.

5.1 MSC samples containing PA-d_{31} as the deuterated membrane component

In order to determine whether IPM has an effect in MSC containing PA, ^{2}H-NMR spectra were acquired from MSC containing PA-d_{31} as a function of temperature. The following subsections will present a series of ^{2}H-NMR spectra and figures (M_1 trends, phase behaviour and phase profiles) to demonstrate that IPM has significant effects on PA in MSC. The three major effects of adding IPM were: the appearance of the isotropic phase at lower temperatures, the shift of the solid to liquid-crystalline phase transition (the first phase transition) to a higher temperature and the liquid-crystalline to isotropic phase transition (the second phase transition) to a lower temperature. The following section will present the ^{2}H-NMR spectra obtained from MSC containing PA-d_{31} as functions of temperature and IPM concentration.

5.1.1 ^{2}H-NMR spectra from MSC containing PA-d_{31}

This section will show the spectral aspect of the effect of IPM on MSC containing PA-d_{31}. Figure 25 shows the Fourier-transformed ^{2}H-NMR spectra (reptime 50 s) from the control, 1% and 10% IPM samples at 25°C, 32°C, 50°C and 65°C. The spectra containing isotropic peaks were plotted both with their isotropic peaks truncated, and with the non-truncated spectra plotted as insets or, for the 10% IPM sample, as a separate

column. Figure 26 shows the Fourier-transformed ^{2}H-NMR spectra (reptime 50 s) from the control, 1% and 10% IPM samples at 65°C to show the more distinct effect of IPM at higher temperatures. The spectra in Figure 26 were area-normalized and their isotropic peaks were not truncated. Note that the signal from the liquid-crystalline phase is almost invisible in Figure 26.

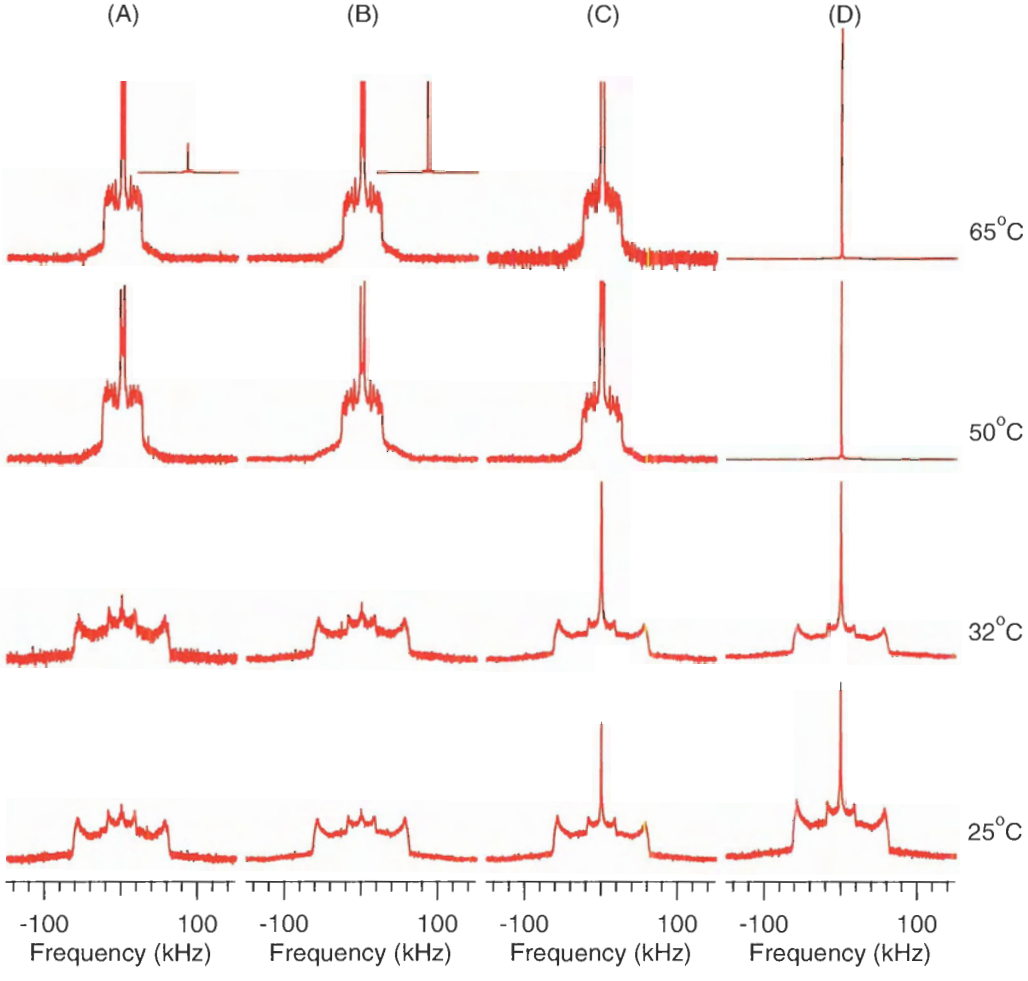

Figure 25: The ^{2}H-NMR spectra (reptime 50 s) demonstrating the effect of IPM on MSC containing PA-d_{31} at different temperatures, pH = 5.2.

(A) 1:1:1 Cer16:Chol:PA-d_{31} (control); (B) 33:33:33:1 Cer16:Chol:PA-d_{31}:IPM (1% IPM); (C) 3:3:3:1 Cer16:Chol:PA-d_{31}:IPM (10% IPM), with isotropic peaks truncated to show the underlying spectra; (D) Non-truncated spectra of (C). Non-truncated spectra of (A) and (B) at 65°C are displayed as insets. The underlying spectra in (A), (B), and (C) are very similar. The spectra of (C) at 50°C, (B) and (C) at 65°C are enlarged 2.0 X, 1.5 X and 3.5 X, respectively to illustrate this.

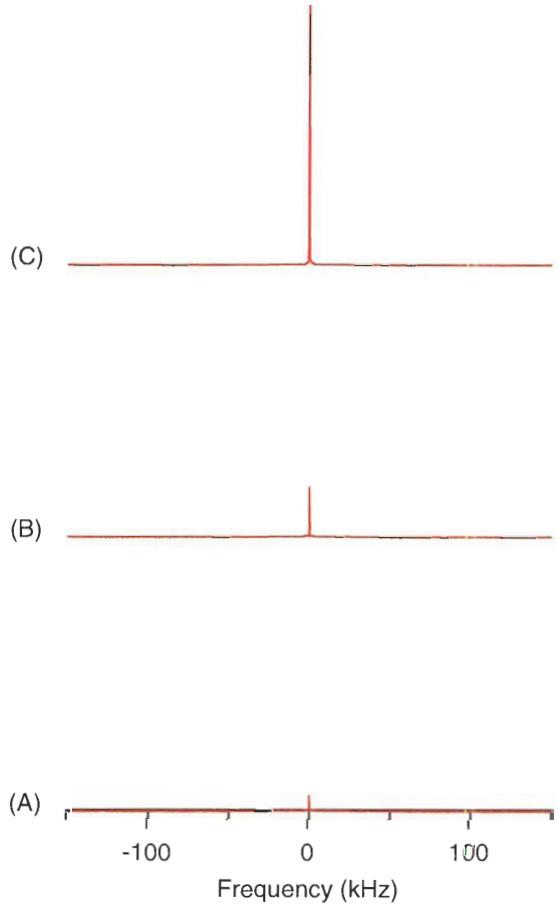

Figure 26: The non-truncated ^{2}H-NMR spectra (reptime 50 s) demonstrating the effect of IPM on MSC containing PA-d_{31} at 65°C, pH = 5.2.

(A) 1:1:1 Cer16:Chol:PA-d_{31} (control); (B) 33:33:33:1 Cer16:Chol:PA-d_{31}:IPM (1% IPM); (C) 3:3:3:1 Cer16:Chol:PA-d_{31}:IPM (10% IPM). Note that these ^{2}H-NMR spectra are area-normalized and the y-axes are displayed in the same scale.

At 25°C, the spectra of all samples exhibit signals from PA-d_{31} in the solid phase, except that in the 10% IPM sample the spectrum has an isotropic peak at its centre. At 32°C, which is close to the physiological temperature of the skin, the spectra of both control and 1% IPM samples still exhibit signals mainly from the solid phase; whereas, that of the 10% IPM sample shows a superposition of signals from the solid phase and a growing isotropic phase. At 50°C (above T_m) in all samples, the signal from the solid

phase has virtually vanished while the signal from the liquid-crystalline phase increases. The amount of signal from the liquid-crystalline phase is the same in both control and 1% IPM samples, but it is decreased in the 10% IPM sample in which the balance of the signal is from the isotropic peak. At 65°C, a signal from the isotropic phase is seen in the control sample; however, there is still a significant amount of signal from the liquid-crystalline phase. At this temperature, IPM enhances the isotropic phase in a concentration-dependent fashion (Figure 26). Both IPM-containing samples show a greater amount of signal from the isotropic phase than the control sample. For any given temperature, the isotropic peak is larger in the spectrum of the 10% IPM sample than in the spectrum of the 1% IPM sample.

In the control sample, no major change in the PA-d_{31} spectrum occurs at temperatures below T_m (25°C and 32°C), where both spectra exhibit signals mainly from the solid phase. At 50°C (above T_m), the Pake doublet at ~ 63 kHz disappears, indicating the disappearance of the solid phase signal, while the liquid-crystalline phase signal now dominates the spectrum, and the isotropic phase signal does not appear until higher temperature (For example, the spectrum at 65°C). In the 1% IPM sample, the ^2H signal changes are similar to those in the control sample, except that the isotropic phase signal is larger in the 1% IPM sample than in the control sample at 65°C. Bigger ^2H signal changes can be observed in the 10% IPM sample, where the signal from PA-d_{31} in the isotropic phase is present at all temperatures. At temperatures above T_m (50°C and 65°C), the liquid-crystalline phase signals are smaller than those in the control and 1% IPM sample. For any given temperature, the isotropic peak is larger in the spectrum of the 10% IPM sample than in the spectrum of the 1% IPM sample.

Generally, the ^{2}H-NMR spectra of PA-d_{31} in the presence or absence of IPM are similar, apart from the isotropic signal. By extracting numerical information from these spectra, temperature-dependent order parameter and phase changes can be analyzed quantitatively. The next section will present a detailed description of the effect of IPM in MSC containing PA-d_{31}.

5.1.2 M_1 and phase behaviour comparison among MSC containing PA-d_{31} as functions of temperature and IPM concentration

By measuring the temperature-dependence of the average width (M_1) of the ^{2}H-NMR spectrum, we found that the addition of IPM had a significant effect. Further analysis of the spectra was performed to determine the temperature-dependence of the percentage of solid, liquid-crystalline and isotropic phases in MSC containing PA-d_{31}. These findings are summarized in Figure 27 which shows M_1 and the percentage of each phase as a function of temperature in the control, 1% and 10% IPM samples.

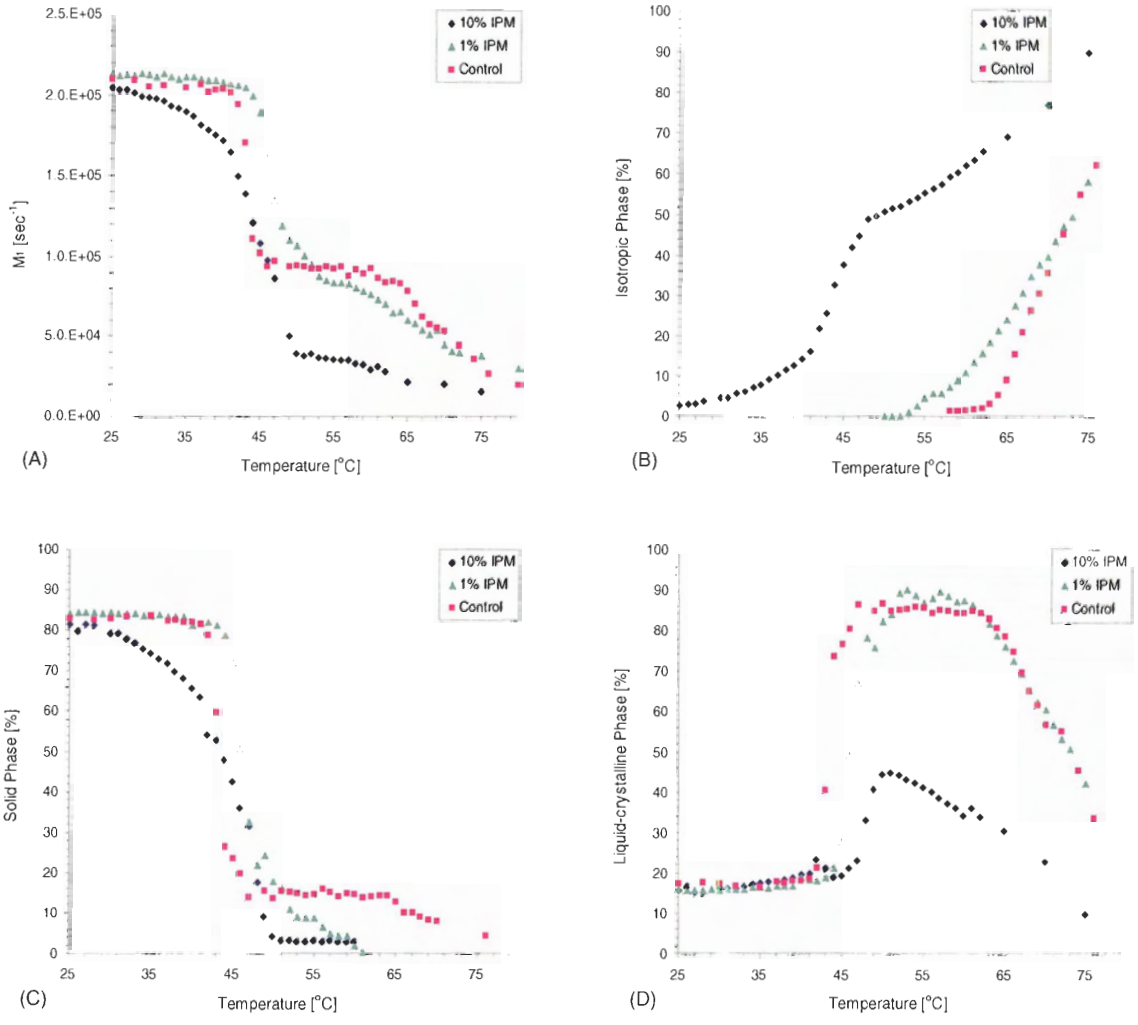

Figure 27: The change in M_1 and phase behaviour of MSC containing different concentrations of IPM.

The (A) M_1 values and percentage of (B) Isotropic; (C) Solid; (D) Liquid-crystalline phase component in the control (1:1:1 Cer16:Chol:PA-d_{31}), 1% IPM (33:33:33:1 Cer16:Chol:PA-d_{31}:IPM) and 10% (3:3:3:1 Cer16:Chol:PA-d_{31}:IPM) IPM samples as a function of temperature, pH = 5.2. Error is estimated to be ± 1% of the value of each phase component for MSC containing PA-d_{31}.

5.1.2.1 M_1

Figure 27A shows the change in M_1 as a function of temperature. The trend for all samples is to start with a plateau at lower temperatures, and then undergo a sharp decrease (~ 45°C) and form a second plateau. In the control and 1% IPM samples, there

is a second decrease in M_1 which takes place at ~ 64°C and ~ 57°C, respectively. In the control sample, M_1 stays constant until ~ 41°C and then decreases rapidly, indicating a sharp decrease in the overall order of PA-d_{31} (41°C ~ 46°C). Between 46°C and 64°C, M_1 remains relatively constant, indicating that the conformational order of PA-d_{31} is maintained at this range of temperatures, and M_1 decreases again at temperatures above 64°C. In the 1% IPM sample, the trend in M_1 as the sample is heated is similar to that in the control sample, but the first decrease starts at a slightly higher temperature (~ 43°C). The second plateau of M_1 in the 1% IPM sample is shorter (54°C ~ 57°C) and with second decrease at a lower temperature (~ 57°C) than that in the control sample (~ 64°C). These differences indicate that the overall order of PA-d_{31} is better maintained in the 1% IPM sample than in the control sample at low temperatures, but less well maintained at high temperatures. In contrast to the MSC behaviour of the control and 1% IPM samples, the 10% IPM sample's M_1 values decline gradually and smoothly from ~ 27°C to 40°C, with no evidence of a plateau. The first abrupt decrease of M_1 in the 10% IPM sample occurs at ~ 40°C, which is lower than that in both the control and the 1% IPM samples. From 50°C to 75°C, M_1 again declines gradually. These differences indicate that the overall order of PA-d_{31} in the 10% IPM sample is reduced at all temperatures.

5.1.2.2 Isotropic phase

Figure 27B shows the change in the percentage of the isotropic phase in the control, 1% and 10% IPM samples as a function of temperature. A general shift of the isotropic phase occurrence to lower temperatures with higher concentrations of IPM can be observed in this figure. The isotropic phase in the control sample does not appear until

~ 61°C. In the 1% IPM sample, the isotropic phase appears at a lower temperature (~ 53°C). The biggest effect can be observed in the 10% IPM sample, where the isotropic phase is already 4% of the signal at 25°C and increases rapidly with temperatures, reaching over 90% at 75°C. Note that the slope of increase in the isotropic phase indicates the rate of increase in the isotropic phase. The rate of increase in the isotropic phase is constant in the control and 1% IPM sample but it changes in the 10% IPM sample. The rate of increase in the isotropic phase is greater in the control sample than in the 1% IPM sample (the slope is steeper for the control sample than for the 1% IPM sample). In the 10% IPM sample, the rate of increase in the isotropic phase stays constant at temperatures below 41°C and becomes greater between 41°C ~ 47°C and returns to the slower rate at temperatures above 47°C.

5.1.2.3 Solid phase

Figure 27C shows the change in the percentage of the solid phase in the control, 1% and 10% IPM samples as a function of temperature. The solid phase shows a similar trend to the M_1 curves. In the control sample, the amount of solid phase decreases at 41°C and then, maintains a plateau (47°C ~ 64°C) and decreases again at temperatures above 64°C. In the 1% IPM sample, the amount of solid phase, which is similar to that in the control sample, decreases at ~ 43°C, remains constant from 53°C to 55°C, and then decreases again at temperatures above 55°C. In the 10% IPM sample, the amount of solid phase starts to decline gradually at 28°C, with a sharper decrease at ~ 41°C, and decreases to a negligible amount at temperatures above 51°C.

The amount of solid phase is steady below the first decrease in both control and 1% IPM samples, but not in the 10% IPM sample. The change in slope of the amount of solid phase as a function of temperature occurs at 41°C for the control sample, 43°C for the 1% IPM sample and 41°C for the 10% IPM sample. These temperatures match the changes in slope associated with T_m in the M_l v.s. Temperature plot (Figure 27A). The second decrease in the amount of solid phase as a function of temperature occurs at 64°C for the control sample, 55°C for the 1% IPM sample and 41°C for the 10% IPM sample. The second decrease in the solid phase occurs at lower temperature in MSC containing higher IPM concentrations.

5.1.2.4 Liquid-crystalline phase

Figure 27D shows the change in the percentage of the liquid-crystalline phase in the control, 1% and 10% IPM samples as a function of temperature. In the control sample, the amount of liquid-crystalline phase increases at ~ 41°C (where the amount of the solid phase decreases) and then is maintained from 47°C to 63°C. At temperatures above 63°C, the amount of liquid-crystalline phase decreases (where the isotropic phase starts to grow). The 1% IPM sample has a similar trend except that the increase in the percentage of liquid-crystalline phase starts at ~ 43°C, and the plateau of constant percentage of liquid-crystalline phase is maintained for a slightly narrower range of temperatures (53°C ~ 61°C). By contrast, the amount of liquid-crystalline phase increases at ~ 45°C to a maximum of ~ 45% at ~ 51°C and at temperatures above 51°C, the amount of liquid-crystalline phase declines steadily in the 10% IPM sample.

The sudden increase in the percentage of liquid-crystalline phase is a reliable measure of T_m. The amount of liquid-crystalline phase is constant in all samples at temperatures below T_m. T_m is higher in MSC containing higher IPM concentrations (control = 41°C; 1% IPM sample = 43°C; 10% IPM sample = 45°C); whereas at high temperatures, the temperature at which the amount of liquid-crystalline phase start to decrease is lower in MSC containing higher IPM concentrations (control = 63°C; 1% IPM sample = 61°C; 10% IPM sample = 51°C)

5.1.3 Concentration-dependent phase changes in MSC containing PA-d_{31}

The temperature-dependent effects of IPM on MSC containing PA-d_{31} (Section 5.1.2) are also clearly dependent on the concentration of IPM. This effect can be determined for individual phases of PA-d_{31} at specific temperatures by plotting the percentage of each phase as a function of IPM concentration. Figure 28 shows the change in the percentages of isotropic, solid and liquid-crystalline phases as a function of the concentration of IPM added at specific temperatures below and above T_m. Figure 28 demonstrates that the isotropic phase increases in a concentration-dependent manner at all temperatures shown, though this is much more pronounced at higher temperatures. At higher temperatures, the liquid-crystalline phase generally decreases with increasing concentration of IPM. The percentage of solid phase experiences only a minor influence from the concentration of IPM.

5.1.4 Temperature-dependent phase profile of MSC containing PA-d_{31} at different IPM concentrations

As previously shown, the behaviour of individual phases of PA-d_{31} changes with temperature and IPM concentration. By plotting the phase profile of each MSC sample, the overall phase changes and transitions within each sample can be viewed as a function of temperature. shows the percentage of all phase components in the control (Figure 29A), 1% IPM (Figure 29B) and 10% IPM (Figure 29C) samples as a function of temperature.

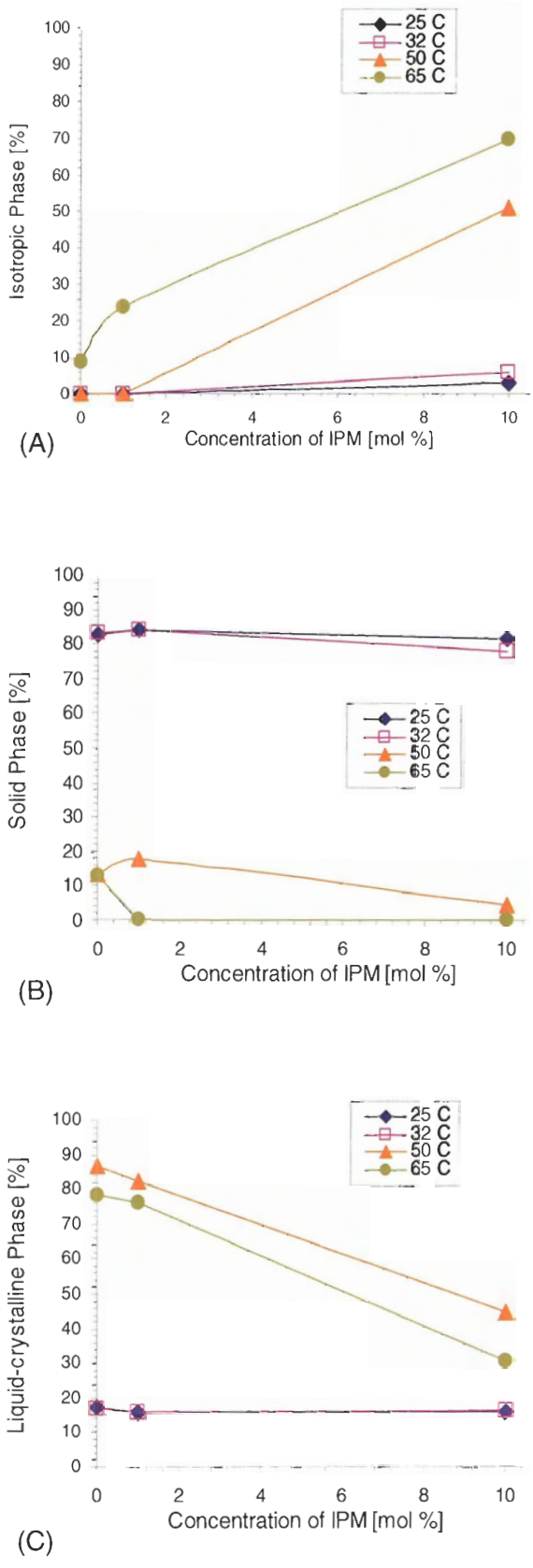

Figure 28:
The variation in phase components as a function of IPM concentration at different temperatures.

The percentage of (A) Isotropic; (B) Solid; (C) Liquid-crystalline phase component as a function of the concentration of IPM added in mol %, pH = 5.2. Error is estimated to be ± 1% of the value of the percentage of each phase component for MSC containing PA-d_{31} (except the percentage of solid phase. The lines are used for visual aid.

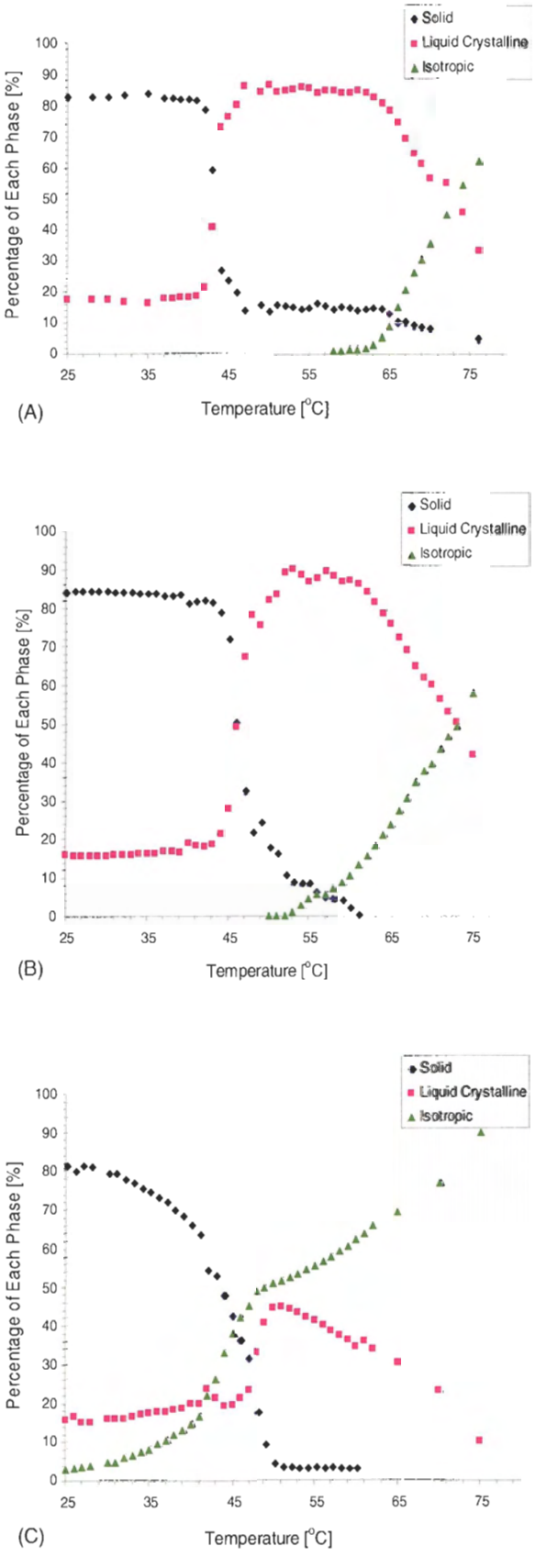

Figure 29:
The phase profiles of PA-d_{31} in MSC containing different concentrations of IPM.

The behaviour of each phase component in the (A) control (1:1:1 Cer16:Chol:PA-d_{31}), (B) 1% IPM (33:33:33:1 Cer16:Chol:PA-d_{31}:IPM) and (C) 10% IPM (3:3:3:1 Cer16:Chol:PA-d_{31}:IPM) samples as a function of temperature, pH = 5.2. Error is estimated to be ± 1% of the value of the percentage of each phase component for MSC containing PA-d_{31}.

The control sample represents the normal phase profile of PA-d_{31} in MSC without IPM. At lower temperatures, the solid phase converts into the liquid-crystalline phase (41°C ~ 47°C). At higher temperatures, the liquid-crystalline phase converts into the isotropic phase (63°C ~ 75°C). These two phase conversions give the characteristic "X-shaped" curve with an increasing linear curve (from the isotropic phase) crossing at the right. Thus, there are two distinct PA-d_{31} lipid phase transitions. The first phase transition is the solid to liquid-crystalline phase conversion and the second phase transition is the liquid-crystalline to isotropic phase conversion.

The 1% IPM sample has a very similar "X-shaped" curve to the control sample, but with a slightly different phase profile. The solid phase in the 1% IPM sample converts into the liquid-crystalline phase at a higher temperature (~ 43°C) than in the control sample (~ 41°C) and this phase conversion continues from 43°C to 53°C. Between 53°C and 61°C, the amount of liquid-crystalline phase has minor fluctuations. At temperatures above 61°C, the liquid-crystalline phase starts converting into the isotropic phase. Thus, the 1% IPM sample has the same two phase transitions as the control sample. The only difference is the temperatures for the two phase transitions. The first phase transition shifts to a higher temperature, and the second phase transition shifts to a lower temperature, when compared to those of the control sample.

The 10% IPM sample has the most significantly different phase profile. The characteristic "X-shaped" curve no longer exists. The integrity of the solid phase is not maintained and it starts converting into the isotropic phase at lower temperatures (~ 28°C) than the control sample (~ 64°C) and 1% IPM sample (~ 55°C). The solid to liquid-crystalline phase conversion is not obvious, but a sharp increase in the proportion

of the liquid-crystalline phase occurs at ~ 45°C. This is a higher T_m than either the control sample (~ 41°C) or 1% IPM sample (~ 43°C). Another major difference is that the liquid-crystalline to isotropic phase conversion shifts to a much lower temperature at ~ 51°C (control = ~ 63°C; 1% IPM sample = ~ 61°C). Thus, the 10% IPM sample has the same two phase transitions as the control and 1% IPM samples. The difference is that the first phase transition shifts to a temperature higher than and the second phase transition shifts to a temperature lower than those in the control and 1% IPM samples.

In summary, all sample phase profiles show that the solid phase converts into the liquid-crystalline phase at the first phase transition and the liquid-crystalline phase converts into the isotropic phase at the second phase transition. The first phase transition occurs at higher temperatures in MSC containing higher IPM concentrations. The second phase transition occurs at lower temperatures in MSC containing higher IPM concentrations. The solid to isotropic phase conversion of PA-d_{31} takes place only in MSC containing a higher IPM concentration. The control and 1% IPM sample phase profiles are similar; whereas, the 10% IPM sample phase profile is significantly different. The integrity of the solid and liquid-crystalline phases is better maintained in the control and 1% IPM samples than that in the 10% IPM sample. The isotropic phase has a greater development in the 10% IPM sample than in the control and 1% IPM samples.

5.1.5 The effect of IPM on PA-d_{31}

Overall, the progressive addition of IPM causes the appearance and increase of the isotropic phase at lower temperatures and the reduced amount of the liquid-crystalline phase at higher temperatures. The first phase transition (solid to liquid-crystalline phase

conversion) shifts to higher temperatures and the second phase transition (liquid-crystalline to isotropic phase conversion) shifts to lower temperatures. The spectral feature, M_1, phase behaviour and phase profile of PA-d_{31} are found to be temperature- and IPM-concentration-dependent.

5.2 MSC samples containing Cer16-d_{31} as the deuterated membrane component

The results in Section 5.1 show that IPM has a pronounced effect on PA in MSC. In order to determine whether IPM has equivalent or different effects on Cer16, ^{2}H-NMR spectra were acquired from MSC containing Cer16-d_{31} as a function of temperature. These spectra were analyzed to determine the phases present and the ^{2}H-NMR data show that IPM has only a minor effect on the first phase transition (solid to liquid-crystalline phase conversion) of Cer16-d_{31} in MSC. However, the addition of IPM to MSC containing Cer16-d_{31} causes the appearance of the isotropic phase at lower temperatures. The following subsections will present a series of ^{2}H-NMR spectra and figures: M_1, phase behaviour and phase profile as functions of temperature and IPM concentration.

5.2.1 ^{2}H-NMR spectra from MSC containing Cer16-d_{31}

This section will show the spectral aspect of the effect of IPM in MSC containing Cer16-d_{31}. Figure 30 shows the Fourier-transformed ^{2}H-NMR spectra (reptime 35 s) from the control, 1% and 10% IPM samples at 25°C, 32°C, 50°C and 65°C. The spectra containing isotropic peaks were plotted with their isotropic peaks truncated, and the non-truncated spectra are plotted as insets. As well, the non-truncated spectra of the 10% IPM sample are plotted in a separate column. Figure 31 shows the Fourier-transformed ^{2}H-

NMR spectra (reptime 35 s) from the control, 1% and 10% IPM samples at 65°C to highlight the effect of IPM on the isotropic phase at higher temperatures. At this temperature, IPM enhances the isotropic phase in a concentration-dependent fashion (Figure 31). The spectra in Figure 31 were area-normalized and their isotropic peaks were not truncated. Note that signals from the solid and liquid-crystalline phases are negligible in Figure 31.

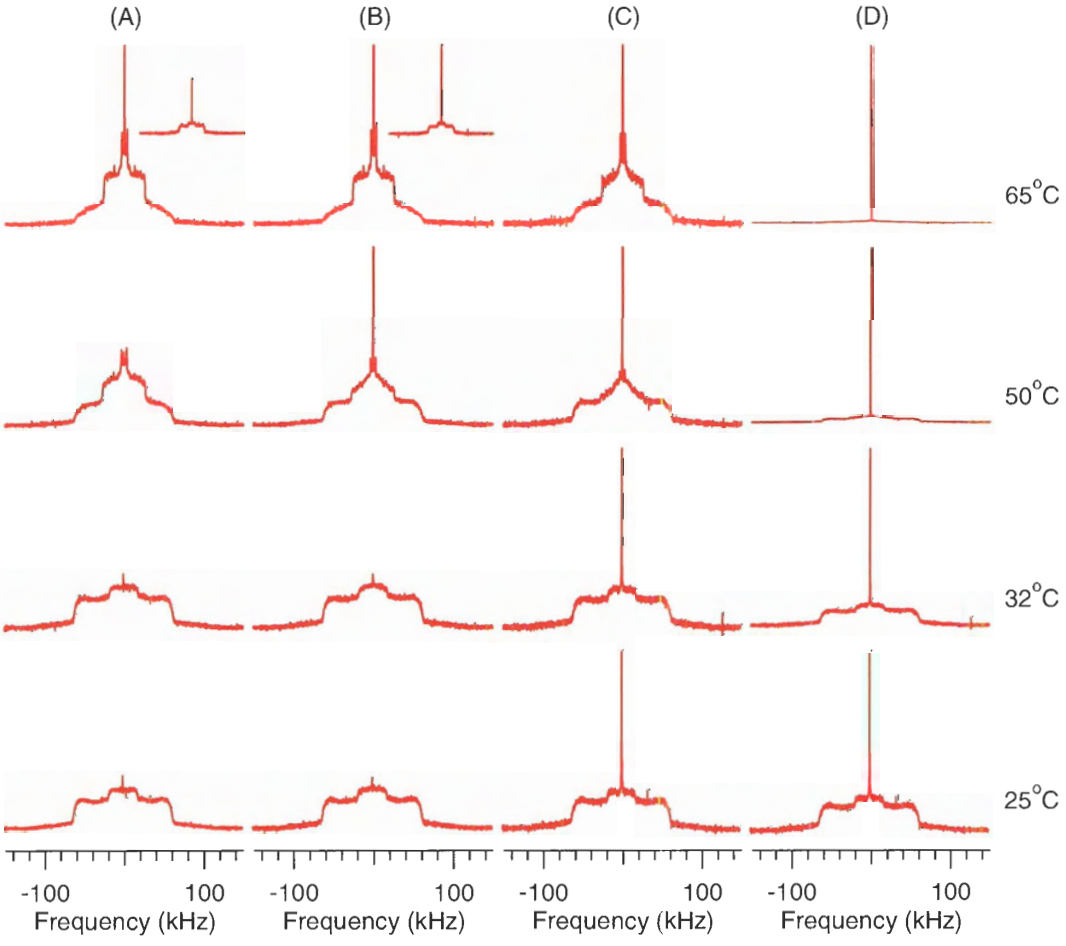

Figure 30: ^{2}H-NMR spectra (reptime 35 s) demonstrating the effect of IPM on MSC containing Cer16-d_{31} at different temperatures, pH = 5.2.

(A) 1:1:1 Cer16-d_{31}:Chol:PA (control); (B) 33:33:33:1 Cer16-d_{31}:Chol:PA:IPM (1% IPM); (C) 3:3:3:1 Cer16-d_{31}:Chol:PA:IPM (10% IPM), with isotropic peaks truncated to show the underlying spectra; (D) Non-truncated spectra of (C). Non-truncated spectra of (A) and (B) at 65°C are displayed inset. The underlying spectra in (A), (B), and (C) are very similar at 25°C, 32°C and 65°C. The spectra of (B) and (C) at 65°C are enlarged 1.1 X and 1.5 X, respectively to illustrate this. Note the disappearance of the liquid-crystalline peaks in the spectrum of (C) at 50°C.

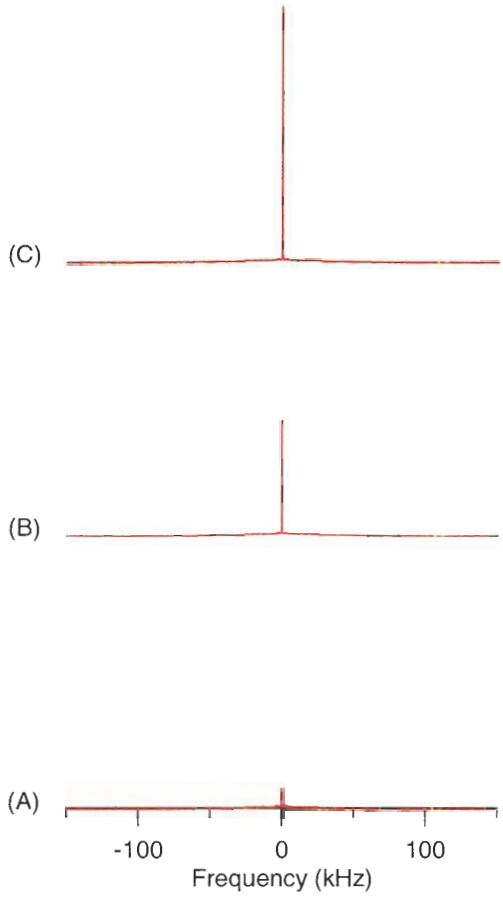

Figure 31: The non-truncated ^{2}H-NMR spectra (reptime 35 s) demonstrating the effect of IPM on MSC containing Cer16-d_{31} at 65°C, pH = 5.2.

(A) 1:1:1 Cer16-d_{31}:Chol:PA (control); (B) 33:33:33:1 Cer16-d_{31}:Chol:PA:IPM (1% IPM); (C) 3:3:3:1 Cer16-d_{31}:Chol:PA:IPM (10% IPM). Note that the ^{2}H-NMR spectra are area-normalized and plotted on the same scale.

At 25°C, the spectra of all samples (Figure 30) exhibit signals from the solid phase and in addition, that of the 10% IPM sample shows an isotropic peak at the centre. At 32°C, which is close to the physiological temperature of the skin, the control and 1% IPM samples still exhibit signals mainly from the solid phase; whereas, the signal from the isotropic phase in the 10% IPM sample has grown (Figure 30D). At 50°C, which is above the main phase transition T_m (the solid to liquid-crystalline phase transition as

reported by the PA-d_{31} (Section 5.1), the amount of signal from the liquid-crystalline phase increases. The liquid-crystalline spectral component of Cer16-d_{31} is most prominent in the control sample and is reduced in the presence of IPM. At this temperature, the signal from the isotropic phase is evident in both IPM samples, and is the largest in the 10% IPM sample, but not observable in the control sample. At 65°C, a signal from the isotropic phase is present in the control sample and increases in both 1% and 10% IPM samples, while the signal from the liquid-crystalline phase decreases with increasing concentration of IPM. In contrast to PA-d_{31} spectra, Cer16-d_{31} spectra exhibit considerable amount of solid phase signals at 50°C and 65°C. For any given temperature, the isotropic peak is the largest in the spectrum of the 10% IPM sample, smaller or absent in the spectrum of the 1% IPM sample, and the smallest or invisible in the spectrum of the control sample.

In the control sample, no major ^2H signal change is evident at temperatures below T_m (25°C and 32°C), where both spectra exhibit signals mainly from the solid phase. Major changes can be observed at temperatures above T_m (50°C and 65°C), where the Pake doublets at ~ 63 kHz decrease in intensity, indicating the decrease in the solid phase signal, while the liquid-crystalline phase signal increases, and the isotropic phase signal appears at higher temperatures (65°C). In the 1% IPM sample, the ^2H signal changes have a similar trend to that in the control sample, but the isotropic phase signal appears at lower temperature (50°C) and is larger in the 1% IPM sample than in the control sample at 65°C. Bigger ^2H-NMR spectral changes can be observed upon the addition of 10% IPM. The isotropic phase signal of Cer16-d_{31} is present at all temperatures at 50°C and

65°C. The liquid-crystalline phase signals are smaller than those in the control and 1% IPM sample.

Generally, below the phase transition, the ^{2}H-NMR spectra of all the MSC samples containing Cer16-d_{31} are similar, apart from the isotropic signal. Above the phase transition, IPM reduces the amount of liquid-crystalline phase and increases the isotropic phase. By extracting numerical information from the spectra, the order parameter (indicated by M_1) and phase changes can be analyzed quantitatively to describe in more detail the effect of IPM in MSC containing Cer16-d_{31}. The next section will present the results of this analysis.

5.2.2 M_1 and phase behaviour comparison among MSC containing Cer16-d_{31} as functions of temperature and IPM concentration

By measuring the temperature-dependence of the average width (M_1) of the ^{2}H-NMR spectrum, we found that the addition of IPM had only a minor effect on Cer16-d_{31}. Further analysis of the spectra was performed to determine the temperature-dependence of the percentage of solid, liquid-crystalline and isotropic phases in MSC containing Cer16-d_{31}. The data showed that the addition of IPM does not cause significant changes in the percentage of the solid phase in MSC containing Cer16-d_{31}. However, the effect of IPM was found to be more pronounced on the percentage of the liquid-crystalline and isotropic phases. This section will present these data in a series of figures to demonstrate these findings. Figure 32 shows the M_1 value and the percentage of each phase component as a function of temperature in the control, 1% and 10% IPM samples.

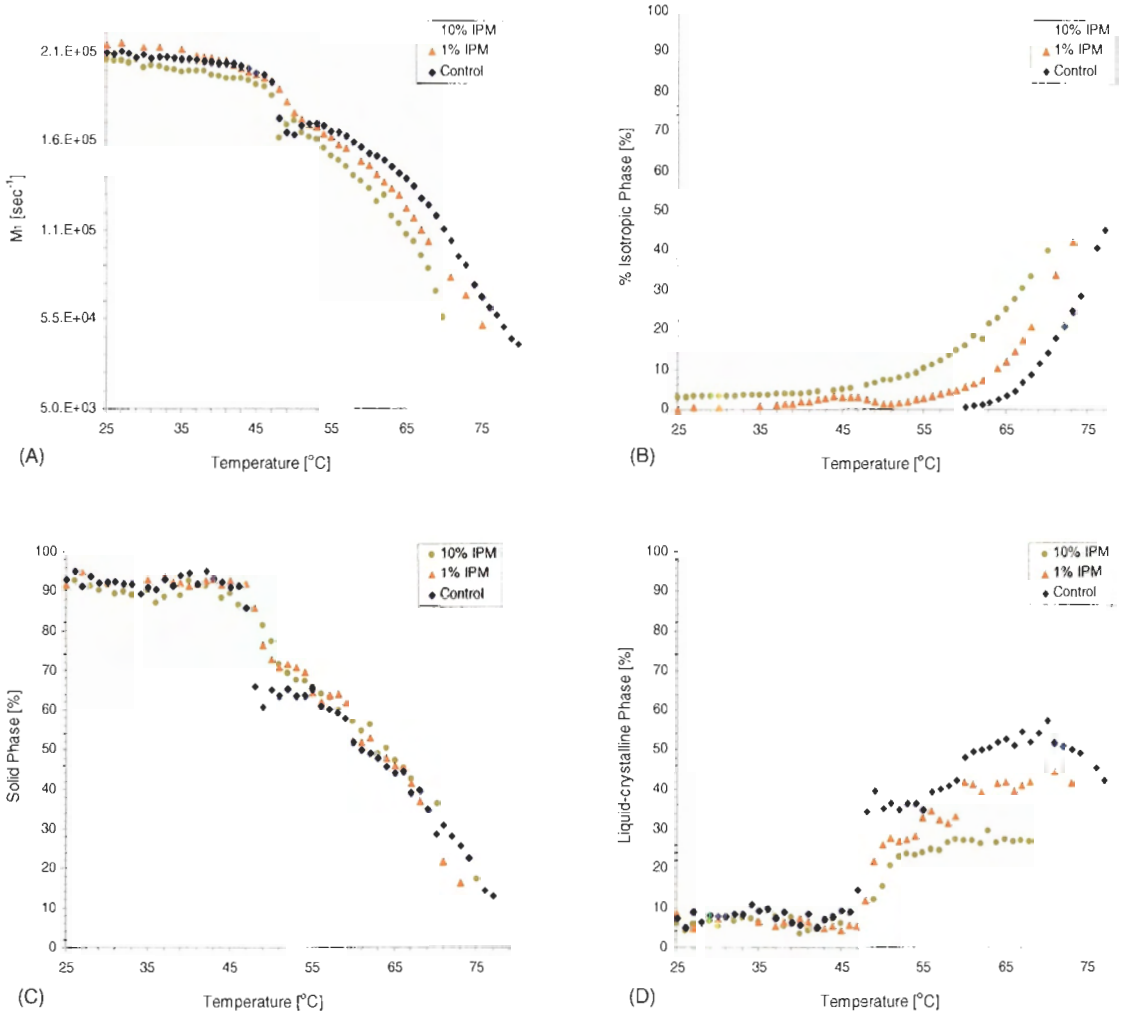

Figure 32: The change in M_l and phase behaviour of MSC containing different concentrations of IPM.

The (A) M_l value and percentage of (B) Isotropic; (C) Solid; (D) Liquid-crystalline phase component in the control (1:1:1 Cer16-d_{31}:Chol:PA), 1% (33:33:33:1 Cer16-d_{31}:Chol:PA:IPM) and 10% (3:3:3:1 Cer16-d_{31}:Chol:PA:IPM) IPM samples as a function of temperature, pH = 5.2. Error is estimated to be ± 1% of the value of the percentage of each phase component for MSC containing Cer16-d_{31}.

5.2.2.1 M_l

Figure 32A shows the change in M_l as a function of temperature. The general trend is a plateau to ~ 46°C and a downward slope above 46°C. The decrease at 46°C is sharper in the control and 10% IPM samples, but rounder for the 1% IPM sample. Above

46°C, the slope in M_1 increases in steepness with increasing IPM concentration. No plateau formation is evident in all samples.

In the control sample, M_1 decreases slowly until 46°C and then decreases rapidly at temperatures between 46°C and 50°C. This indicates a sharp decrease in the overall order of Cer16-d_{31} at this range of temperatures (46°C and 50°C). Then, M_1 increases at temperatures between 50°C and 54°C, which indicates a partial restoration of the overall order of Cer16-d_{31}. At temperatures above 54°C, M_1 declines gradually, which indicates that the overall order of Cer16-d_{31} decreases slowly at temperatures above 54°C.

In the 1% IPM sample, the trend of M_1 is similar to that in the control sample at temperatures below 46°C. The first decrease is delayed and less sharp (48°C ~ 52°C), which indicates a less dramatic change in the overall order of Cer16-d_{31} at this range of temperatures. There is no evidence of the restoration of M_1 values. However, M_1 decreases again gradually at temperatures above 52°C.

In the 10% IPM sample, M_1 shows a similar trend to the control sample. The first decrease of M_1 occurs at temperatures between 46°C and 48°C, and it is a steeper decrease than that in the 1% IPM sample. This indicates that the overall order of Cer16-d_{31} in MSC containing 10% IPM decreases more rapidly than in MSC containing 1% IPM. Then, M_1 increases at temperatures between 48°C and 50°C, which also indicates a partial restoration of the overall order of Cer16-d_{31} in MSC containing 10% IPM. At temperatures above 50°C, M_1 declines gradually, which suggests that the overall order of Cer16-d_{31} decreases slowly at temperatures above 50°C.

At low temperatures, M_1 of the 10% IPM sample is lower than that of the control and 1% IPM samples, which suggests that the overall order of Cer16-d_{31} is less well maintained in the 10% IPM sample than in the control and 1% IPM samples. At higher temperatures (≥ 54°C), M_1 of the 10% IPM sample is the lowest, while M_1 of the 1% IPM sample is the intermediate and M_1 of the control sample is the highest. This suggests that at higher temperatures, the overall order of Cer16-d_{31} is the least maintained in the 10% IPM sample and well maintained in the control sample. The first M_1 decrease is not influenced by the concentration of IPM. The second M_1 decrease shifts to lower temperatures with higher concentration of IPM (control = 54°C; 1% IPM = 52°C; 10% IPM = 50°C).

5.2.2.2 Isotropic phase

Figure 32B shows the change in the percentage of the isotropic phase in the control, 1% and 10% IPM samples as a function of temperature. The isotropic phase in the control sample does not appear until 61°C. In the 1% IPM sample, the isotropic phase appears at a lower temperature (~ 37°C) and increases rapidly at temperatures above 55°C. The most significant effect can be observed in the 10% IPM sample, where the isotropic phase is already 3% of the signal at 25°C and increases gradually to ~ 45°C, and more rapidly upon further heating.

5.2.2.3 Solid phase

Figure 32C shows the change in the percentage of the solid phase in the control, 1% and 10% IPM samples as a function of temperature. The amount of solid phase shows

a similar trend to M_1, and decreases at 46°C, 47°C and 48°C in the control, 1% IPM and 10% IPM samples, respectively. The percentage of the solid phase is similar for all samples above 55°C.

In the control sample, the amount of solid phase maintains a plateau through a narrow range of temperatures (50°C ~ 55°C), and decreases again at higher temperatures (55°C ~ 77°C). In the 1% IPM sample, the amount of solid phase shows a similar trend to that in the control sample, but the decrease at 47°C is smoother. The plateau occurs at a slightly narrower range of temperatures (51°C ~ 54°C) and the amount of solid phase decreases again at temperatures above 54°C. In the 10% IPM sample, the first decrease (~ 48°C) is also smoother than that in the control and there is only a very short plateau (52°C ~ 54°C).

5.2.2.4 Liquid-crystalline phase

Figure 32D shows the change in the percentage of the liquid-crystalline phase in the control, 1% and 10% IPM samples as a function of temperature. In the control sample, the amount of liquid-crystalline phase increases at ~ 46°C, maintains in a plateau to ~ 36% (50°C ~ 55°C) and increases again at temperatures above 55°C. These changes correlate with those in Figure 32C. Thus, the solid phase converts into the liquid-crystalline phase at these temperatures. The 1% IPM sample has a similar trend except that the increase in the liquid-crystalline phase starts at ~ 47°C. However, the plateau proportion of the liquid-crystalline phase is only ~ 26%. In the 10% IPM sample, the

liquid-crystalline phase increases at ~ 48°C to ~ 24% and stays roughly constant upon further heating (53°C ~ 75°C).

The amount of liquid-crystalline phase is steady in all samples before the sharp increase. The increase in the amount of liquid-crystalline phase occurs at higher temperatures in MSC containing higher IPM concentrations (control = 46°C; 1% IPM sample = 47°C; 10% IPM sample = 48°C), which corresponds to the first decrease in the amount of solid phase in all samples at the same temperatures (Section 5.2.2.3). Above 50°C, the maximum percentage of liquid-crystalline phase decreases with increasing IPM concentration.

5.2.3 Concentration dependence phase changes in MSC containing Cer16-d_{31}

Since the temperature-dependent effect of IPM (Section 5.2.2) is also dependent on the concentration, by plotting the percentage of each phase as a function of IPM concentration, the effect of IPM concentrations on MSC containing Cer-d_{31} can be determined in individual phases at specific temperatures. Figure 33 shows the change in the percentage of isotropic, solid and liquid-crystalline phases as a function of the concentration of IPM added at specific temperatures below and above the phase transition. Figure 33 demonstrates that the increase in the isotropic phase and the decrease in the liquid-crystalline phase are concentration dependent. Above T_m, the isotropic phase increases with increased concentration of IPM; whereas, the liquid-crystalline phase decreases with increasing concentration of IPM. The solid phase of Cer16-d_{31} is relatively unaffected by the concentration of IPM.

5.2.4 Temperature-dependent phase profile of MSC containing Cer16-d_{31} at different IPM concentrations

As previously shown, individual phases displayed by Cer16-d_{31} change with temperature and IPM concentration. By outlining the phase profile of each MSC sample, the overall phase transitions within each sample can be viewed as a function of temperature. Figure 34 shows the percentage of all phase components in the control (Figure 34A), 1% (Figure 34B) and 10% IPM (Figure 34C) samples as a function of temperature.

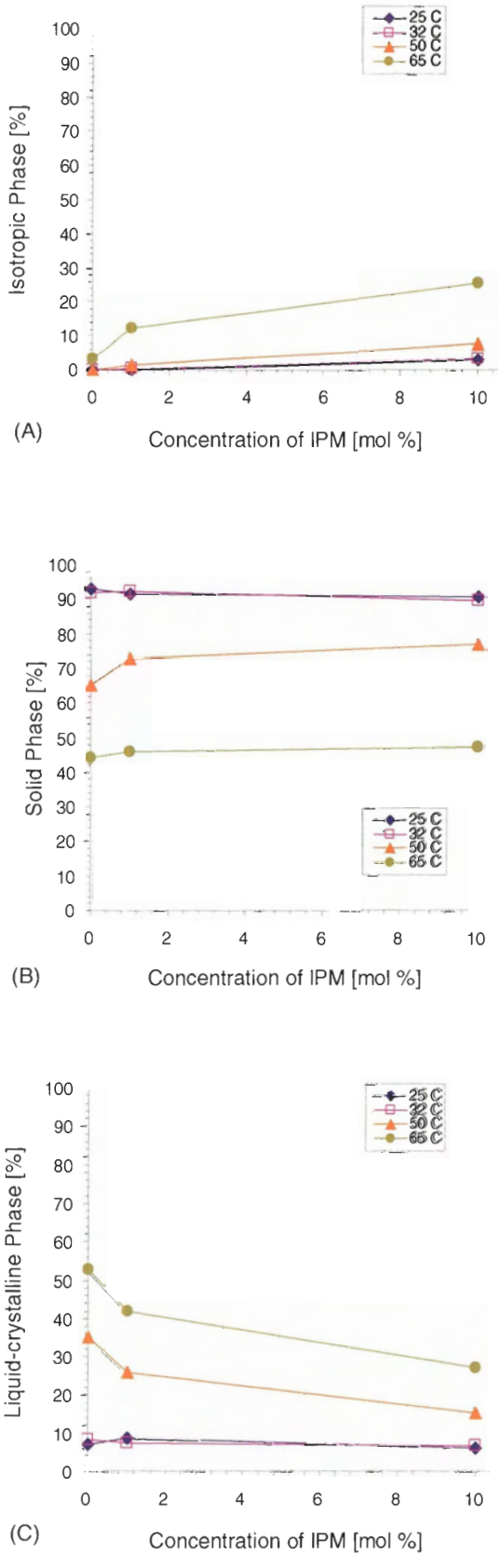

Figure 33:
The variation in phase components as a function of IPM concentration at different temperatures.

The percentage (A) Isotropic; (B) Solid; (C) Liquid-crystalline phase component as a function of the concentration of IPM added in mol %, pH = 5.2. Error is estimated to be ± 1% of the value of the percentage of each phase component for MSC containing Cer16-d_{31}. The lines are used for visual aid.

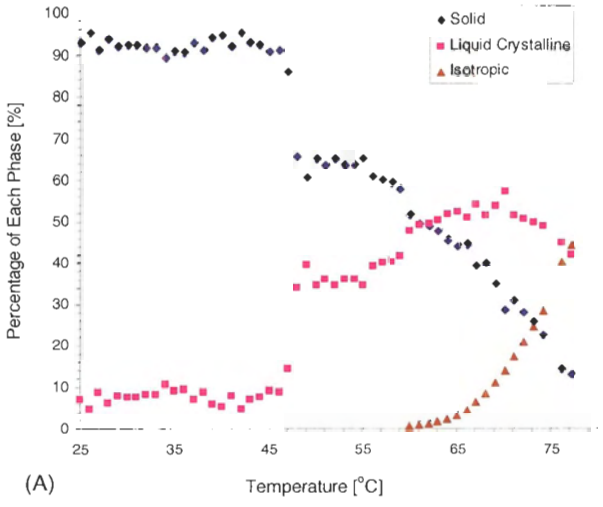

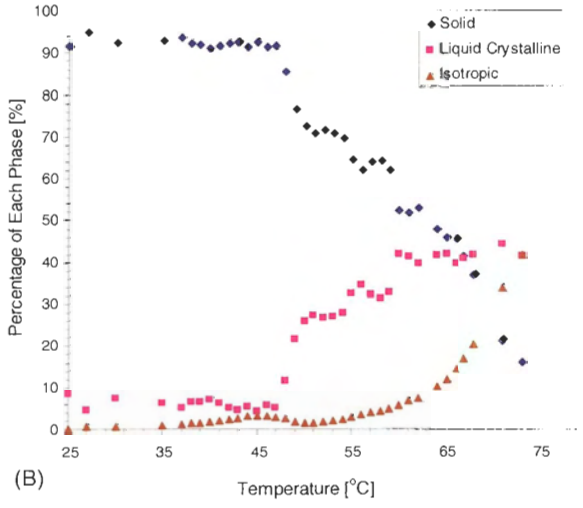

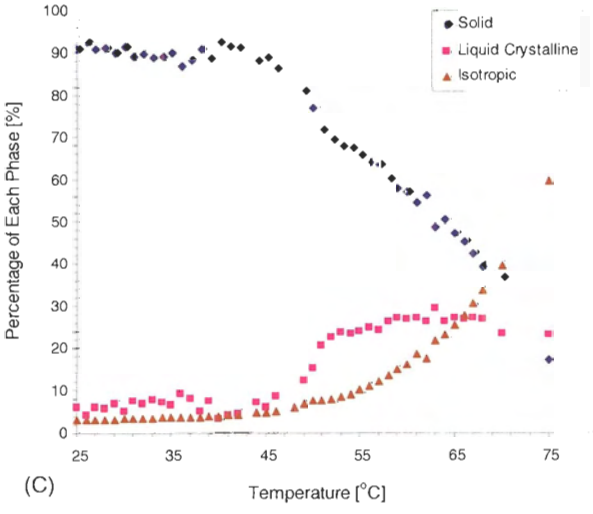

Figure 34:
The phase profiles of Cer16-d_{31} in MSC containing different concentrations of IPM.

The behaviour of each phase component in the (A) control (1:1:1 Cer16-d_{31}:Chol:PA), (B) 1% (33:33:33:1 Cer16-d_{31}:Chol:PA:IPM) and (C) 10% (3:3:3:1 Cer16-d_{31}:Chol:PA:IPM) IPM samples as a function of temperature, pH = 5.2. Error is estimated to be ± 1% of the value of the percentage of each phase component for MSC containing Cer16-d_{31}.

The control sample represents the normal phase profile of Cer16-d_{31} in MSC without IPM. The solid phase converts into the liquid-crystalline phase at two different ranges of temperatures (46°C ~ 48°C; 59°C ~ 63°C, rapid phase conversion at 59°C ~ 60°C). At temperatures above 63°C, the solid phase converts into the isotropic phase. Thus, there are three distinct Cer16-d_{31} lipid phase transitions. The first and second are the solid to liquid-crystalline phase conversion, and the third is the solid to isotropic phase conversion.

The 1% IPM sample has a similar profile to the control sample. The solid phase converts into the liquid-crystalline phase at two different temperature ranges (47°C ~ 51°C; 59°C ~ 60°C). At temperatures above 62°C, the solid phase converts into the isotropic phase. Thus, the three phase transitions are the same in both control and 1% IPM samples. The only difference is that the first phase transition occurs at a higher temperature in the 1% IPM sample than in the control sample.

The 10% IPM sample has the most significantly different phase profile. The isotropic phase appears at a much lower temperature (25°C). The solid phase converts into the liquid-crystalline phase at one temperature range only (48°C ~ 53°C). There is no obvious second phase transition. The solid phase converts into the isotropic phase gradually at temperatures above the first phase transition (53°C ~ 75°C). The liquid-crystalline phase has only one increase in contrast to the control and 1% IPM samples, and maintains a long-lasting plateau at ~ 26% at higher temperatures (53°C ~ 75°C). The first phase transition is the same in the 10% IPM sample as in the control and 1% IPM samples, but the second phase transition is not observable in the 10% IPM sample, although a gradual solid to isotropic phase conversion is evident.

In summary, the control and 1% IPM samples have similar phase profiles. Both phase profiles show that the solid phase converts into the liquid-crystalline phase at the first and second phase transitions, and the solid phase converts into the isotropic phase at the third phase transition. The 10% IPM sample has a very different phase profile: the first phase transition is present but the second phase transition is absent. In all samples, the first phase transition occurs at higher temperatures in MSC containing higher IPM concentrations, and the third phase transition occurs at lower temperatures in MSC containing higher IPM concentrations. The integrity of the solid phase of Cer16-d_{31} is better maintained than that of PA-d_{31}. The isotropic phase has a greater development in the 10% IPM sample than in the control and 1% IPM samples.

5.2.5 The effect of IPM on Cer16-d_{31} in MSC

Overall, the addition of IPM causes the appearance and increase of the isotropic phase of Cer16-d_{31} at lower temperatures as well as reducing the amount of the liquid-crystalline phase of Cer16-d_{31} at higher temperatures. In MSC containing IPM, the first phase transition shifts to higher temperatures and the third phase transition shifts to lower temperatures. The second phase transition is not observable in the 10% IPM sample. 10% IPM has a greater effect than 1% IPM on the phase behaviour of MSC.

5.3 MSC sample containing IPM-d_{27} as the deuterated membrane component

The data obtained from MSC containing PA-d_{31} and Cer16-d_{31} demonstrates that IPM has significant effects on the phase behaviour and profiles of PA and Cer16. However, the nature of IPM's activity in MSC could not be visualized without

deuterating IPM. By obtaining data from MSC containing IPM-d_{27}, the phase behaviour of IPM in MSC can be observed as a function of temperature. This section will present ^{2}H-NMR spectra and information on the phase changes obtained from MSC containing 10% IPM-d_{27} (3:3:3:1 Cer16:PA:Chol:IPM-d_{27}).

5.3.1 ^{1}H-NMR spectra from MSC containing IPM-d_{27}

This section will show the spectral aspect of the behaviour of IPM in MSC. Figure 35 shows the Fourier-transformed ^{2}H-NMR spectra (reptime 2 s) of 10% IPM-d_{27} in MSC (3:3:3:1 Cer16:Chol:PA:IPM-d_{27}) at 32°C, 50°C and 65°C. The spectra containing isotropic peaks were plotted with their isotropic peaks truncated (column A). The isotropic peak was also removed from these spectra to show the underlying spectra (column B). The scale of y-axis is the same within but different across the two columns of spectra, except that the intensity of 32°C spectrum in column (B) is reduced 0.05 X to show the evidence of no remaining isotropic signal. The spectra were apodized (Refer to Section 3.4 for apodization) to remove spectral artefacts from the isotropic truncation effect and to show the signal from the liquid-crystalline phase in the underlying spectra.

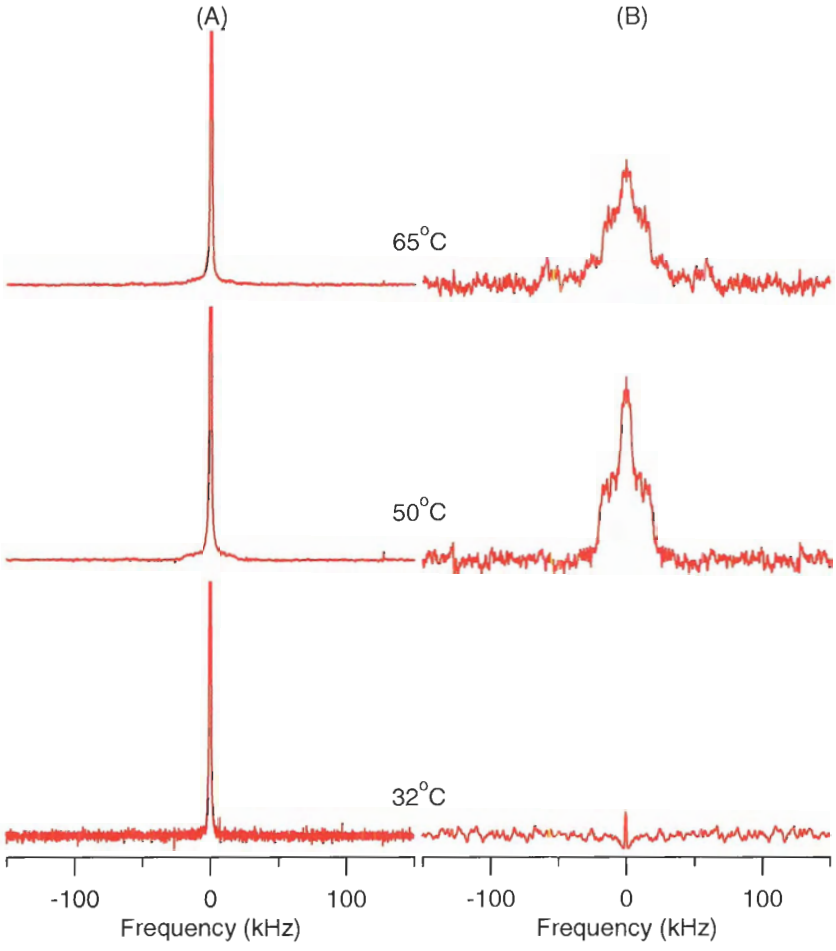

Figure 35: The apodized (A) ^{2}H-NMR spectra (reptime 2 s) with isotropic peaks truncated and (B) ^{2}H-NMR spectra (reptime 2 s) with isotropic peak removed demonstrating the behaviour of IPM in the 10% IPM sample (3:3:3:1 Cer16:Chol:PA:IPM-d_{27}) at different temperatures, pH = 5.2.

Note that the spectra at 32°C were not apodized, and the intensity of the 32°C spectrum in column (B) is reduced 0.05 X to demonstrate the absence of liquid-crystalline and isotropic phase signals. Apodization parameter: (A) 0.50 Hz (50°C), 0.44 Hz (65°C); (B) 0.50 Hz (50°C), 1.00 Hz (65°C). The y-axes of (A) and (B) are not displayed in the same scale, but the same scale within the same column.

At 32°C, which is close to the physiological temperature of the skin, the spectrum exhibits signals from the isotropic phase only. At 50°C, which is above the main phase transition T_m, the signal from the liquid-crystalline phase becomes present. After

apodization, the spectra with isotropic peaks, to a lesser extent, removed clearly display signals from the liquid-crystalline phase at 50°C and 65°C.

Generally, at temperatures below 36°C (data not shown), the spectra are similar, only showing the signal from the isotropic phase. At temperatures above 36°C, the liquid-crystalline phase appears, grows and eventually declines at higher temperatures. By extracting numerical information from these spectra, these phase changes can be analyzed quantitatively. The next section will present the results of this analysis.

5.3.2 Phase behaviour of IPM in MSC containing IPM-d_{27} as a functions of temperature

Further measurement and analysis of the ^{2}H-NMR spectra reveal the amount of IPM in liquid-crystalline and isotropic phases at different temperatures. Figure 36 shows the percentages of isotropic and liquid-crystalline phase components of IPM-d_{27} in MSC as a function of temperature. Since there is no solid phase signal from IPM-d_{27}, changes in the percentages of isotropic and liquid-crystalline phases are directly correlated.

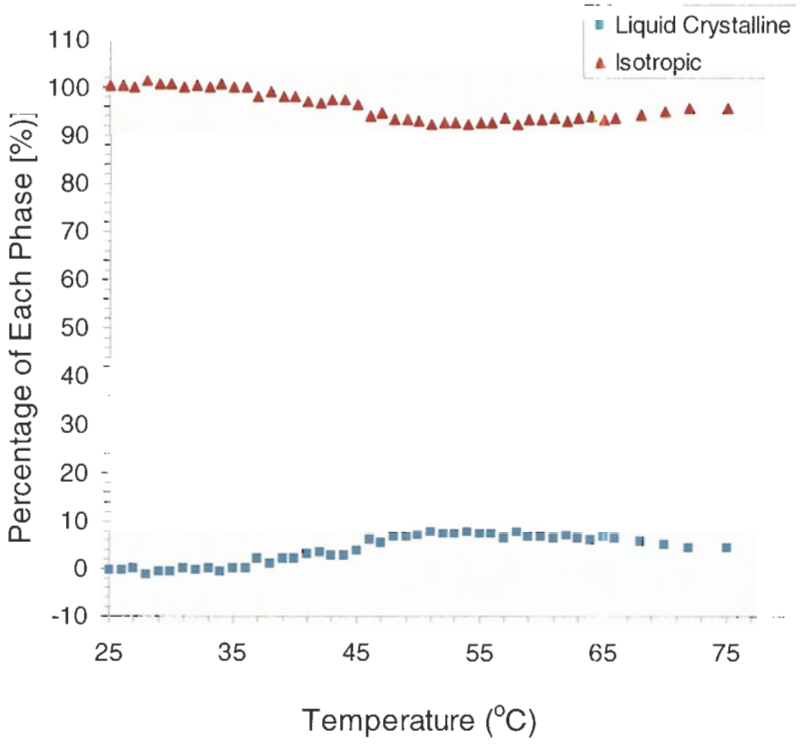

Figure 36: The percentage of the liquid-crystalline and isotropic phase components in the 10% (3:3:3:1 Cer16:Chol:PA:IPM-d_{27}) IPM sample as a function of temperature, pH = 5.2.

Error is estimated to be ± 1% of the value of the percentage of each phase component for MSC containing IPM-d_{27}.

At temperatures below 36°C, IPM-d_{27} in MSC shows 100% isotropic motion. At temperatures above 36°C, the liquid-crystalline phase signal from IPM-d_{27} appears. The proportion of IPM-d_{27} in the liquid-crystalline phase continues growing to a maximum of ~ 8% and declines at temperatures above 61°C. This figure indicates that the amount of liquid-crystalline and isotropic phases of IPM post a slight change initiating at 36°C.

5.3.3 Phase composition comparison

Given all the information on the changes in the phase behaviour and profiles of MSC containing Cer16-d_{31}, PA-d_{31} and IPM-d_{27}, the phase composition of MSC containing 10% IPM can be calculated to compare with that of MSC without IPM. The phase composition of MSC with or without IPM is computed using the data from deuterated membrane components only, which necessarily excludes cholesterol. Note that 30.00% or 33.33% of the total membrane components is cholesterol in MSC with or without IPM, respectively. Thus, the calculation of the phase compositions of deuterated membrane components is based on the remaining 70.00% or 66.67% of the total membrane components in MSC with or without IPM, respectively. Figure 37 shows the phase compositions of all deuterated membrane components in the control and 10% IPM samples at 25°C, 32°C, 50°C and 65°C.

Figure 37: The phase compositions of all deuterated membrane components in MSC containing no IPM and 10% IPM.

The phase compositions of all deuterated membrane components in (A~D) 1:1:1 Cer16:Chol:PA (control) and (E~H) 3:3:3:1 Cer16:Chol:PA:IPM (10% IPM) samples containing either Cer16-d_{31}, PA-d_{31} or IPM-d_{27} at different temperatures, pH = 5.2 {(A) & (E) = 25°C; (B) & (F) = 32°C; (C) & (G) = 50°C; (D) & (H) = 65°C}. Error is estimated to be ± 1% of the value of the percentage of each phase component for MSC containing Cer16-d_{31}, PA-d_{31} or IPM-d_{27}.

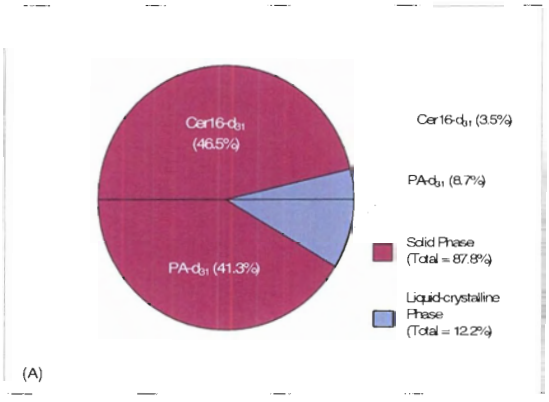
Cer16-d31 (46.5%)
PA-d31 (41.3%)
Cer16-d31 (3.5%)
PA-d31 (8.7%)
Solid Phase (Total = 87.8%)
Liquid-crystalline Phase (Total = 12.2%)

(A)

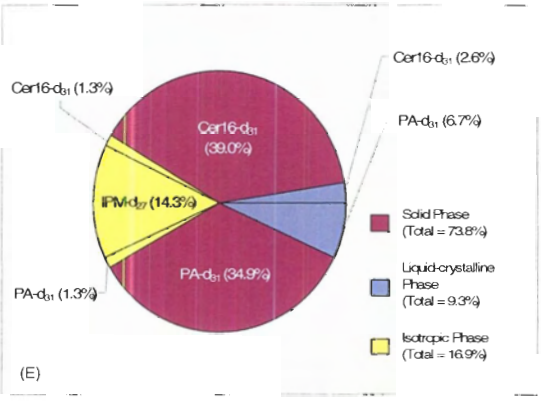
Cer16-d31 (39.0%)
IPM-d27 (14.3%)
PA-d31 (34.9%)
Cer16-d31 (1.3%)
Cer16-d31 (2.6%)
PA-d31 (6.7%)
PA-d31 (1.3%)
Solid Phase (Total = 73.8%)
Liquid-crystalline Phase (Total = 9.3%)
Isotropic Phase (Total = 16.9%)

(E)

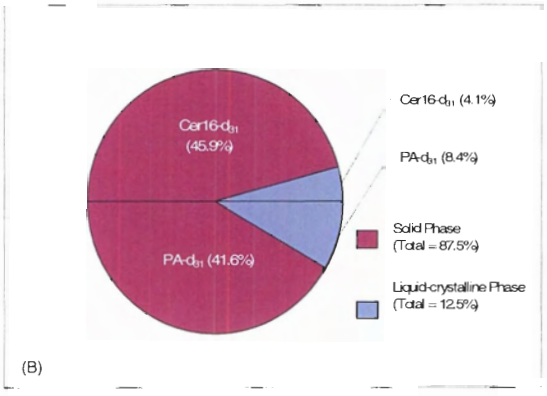
Cer16-d31 (45.9%)
PA-d31 (41.6%)
Cer16-d31 (4.1%)
PA-d31 (8.4%)
Solid Phase (Total = 87.5%)
Liquid-crystalline Phase (Total = 12.5%)

(B)

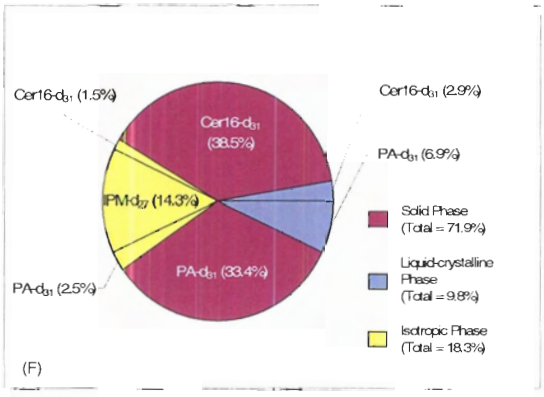
Cer16-d31 (38.5%)
IPM-d27 (14.3%)
PA-d31 (33.4%)
Cer16-d31 (1.5%)
Cer16-d31 (2.9%)
PA-d31 (6.9%)
PA-d31 (2.5%)
Solid Phase (Total = 71.9%)
Liquid-crystalline Phase (Total = 9.8%)
Isotropic Phase (Total = 18.3%)

(F)

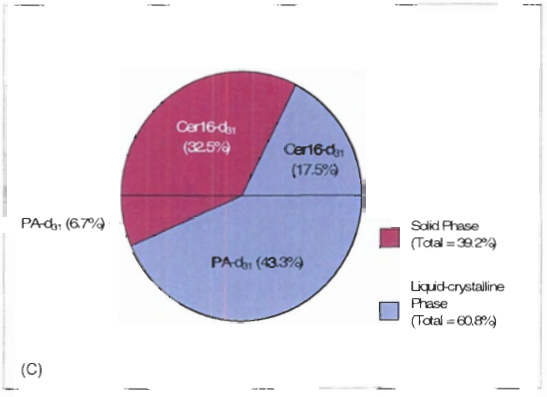
Cer16-d31 (32.5%)
Cer16-d31 (17.5%)
PA-d31 (43.3%)
PA-d31 (6.7%)
Solid Phase (Total = 39.2%)
Liquid-crystalline Phase (Total = 60.8%)

(C)

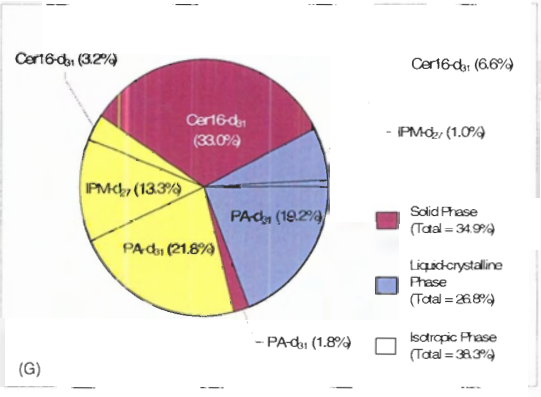
Cer16-d31 (33.0%)
IPM-d27 (13.3%)
PA-d31 (19.2%)
PA-d31 (21.8%)
Cer16-d31 (3.2%)
Cer16-d31 (6.6%)
IPM-d27 (1.0%)
PA-d31 (1.8%)
Solid Phase (Total = 34.9%)
Liquid-crystalline Phase (Total = 26.8%)
Isotropic Phase (Total = 38.3%)

(G)

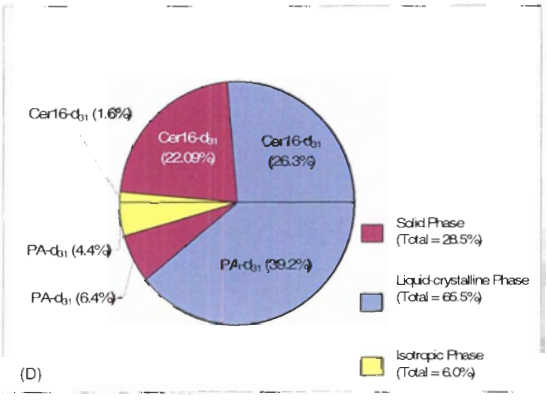
Cer16-d31 (22.09%)
Cer16-d31 (26.3%)
PA-d31 (39.2%)
Cer16-d31 (1.6%)
PA-d31 (4.4%)
PA-d31 (6.4%)
Solid Phase (Total = 28.5%)
Liquid-crystalline Phase (Total = 65.5%)
Isotropic Phase (Total = 6.0%)

(D)

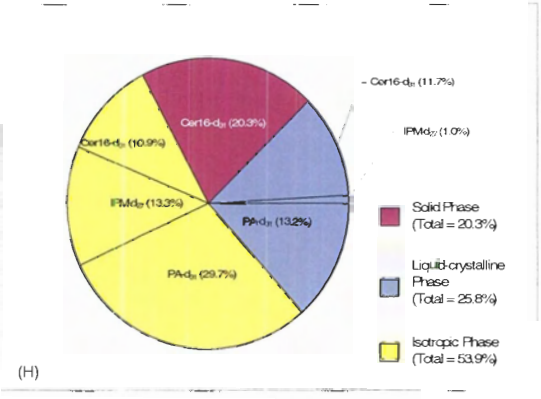
Cer16-d31 (20.3%)
IPMd27 (13.3%)
PA-d31 (29.7%)
Cer16-d31 (11.7%)
IPMd27 (1.0%)
PA-d31 (13.2%)
Solid Phase (Total = 20.3%)
Liquid-crystalline Phase (Total = 25.8%)
Isotropic Phase (Total = 53.9%)

(H)

In the absence of IPM, the phase composition of MSC consists of only solid and liquid-crystalline phases below the phase transition (25°C and 32°C). Above T_m, at 50°C, the overall proportion of the liquid-crystalline phase increases. The isotropic phase appears as a part of the phase composition only at higher temperatures (65°C) and is only a small proportion (~ 6%).

In the 10% IPM sample, the phase composition consists of solid, liquid-crystalline and isotropic phases below the phase transition (25°C and 32°C). At these temperatures (25°C and 32°C), the solid and liquid-crystalline phases include PA-d_{31} and Cer16-d_{31}, but not IPM-d_{27}. Just above the phase transition (50°C), the remaining solid phase is nearly all Cer16-d_{31}. The liquid-crystalline phase now includes IPM-d_{27} as well as Cer16-d_{31} and PA-d_{31}. The isotropic phase (~ 38% of the membrane) is now chiefly composed of PA-d_{31} and contains only a small amount of Cer16-d_{31}. At higher temperatures (65°C), the phase composition consists of small amount of solid phase and liquid-crystalline phase with a large proportion of isotropic phase. The solid phase consists of only Cer16-d_{31}. The liquid-crystalline phase consists of Cer16-d_{31}, PA-d_{31} and IPM-d_{27}. The isotropic phase consists of Cer16-d_{31}, PA-d_{31} and IPM-d_{27} as well.

5.4 Overall effect of IPM on MSC

The addition of IPM has a dramatic effect on MSC. The PA-d_{31} and Cer16-d_{31} develop an isotropic phase in the presence of IPM at lower temperatures than in the control sample. By contrast, the solid to liquid-crystalline phase transition temperature (T_m) in both PA-d_{31} and Cer16-d_{31} samples increases slightly. IPM shows an evidence of localizing into and out of the liquid-crystalline phase domain.

Table 3 shows the summary of the temperature history of MSC at different concentrations of IPM. This summary provides the quantitative information of the increase/decrease in different phase components of individual deuterated membrane lipids as a function of temperature. By inspecting this summary, we are able to draw the information of physical, molecular and phase interactions among lipids in MSC, which will be discussed in more detail in Chapter 6.

Table 3: The temperature history of MSC containing PA-d_{31}, Cer16-d_{31} or IPM-d_{27} at different concentrations of IPM.

This is a summary of all the phase conversions that occur in MSC as a function of temperature at different IPM concentrations. The first phase transition labelled yellow (PA-d_{31} and Cer16-d_{31}). The second phase transition is labelled green (PA-d_{31} and Cer16-d_{31}). The third phase transition is labelled pink (PA-d_{31} and Cer16-d_{31}). The fourth phase transition is labelled light green (Cer16-d_{31}). All other phase conversions are labelled white. The shaded area between 56°C and 60°C in the IPM-d_{27} column indicates the temperature range at which the initiation of the liquid-crystalline to isotropic phase conversion occurs.

Temperature History of MSC							
	PA-d_{31}			Cer16-d_{31}			IPM-d_{27}
[IPM]/ Temp (°C)	0%	1%	10%	0%	1%	10%	10%
25							
26							
27							
28			S→I				
29			S↓ 77.7%				
30			I↑ 47.7%				
31							
32							
33							
34							
35							
36							I→L
37							I↓ 6.5%
38							L↑ 6.5%
39							
40							
41	S→L						
42	S↓ 67.7%						
43	L↑ 67.7%	S→L					
44		S↓ 72.3%					
45		L↑ 71.4%	S→L				
46			L↑ 30.0%	S→L			
47				S↓ 25.5%	S→L		
48				L↑ 25.5%	S↓ 20.9%	S→L	
49					L↑ 22.4%	S↓ 18.6%	
50						L↑ 15.3%	
51			L→I				
52			L↓ 34.5%				
53			I↑ 37.7%				

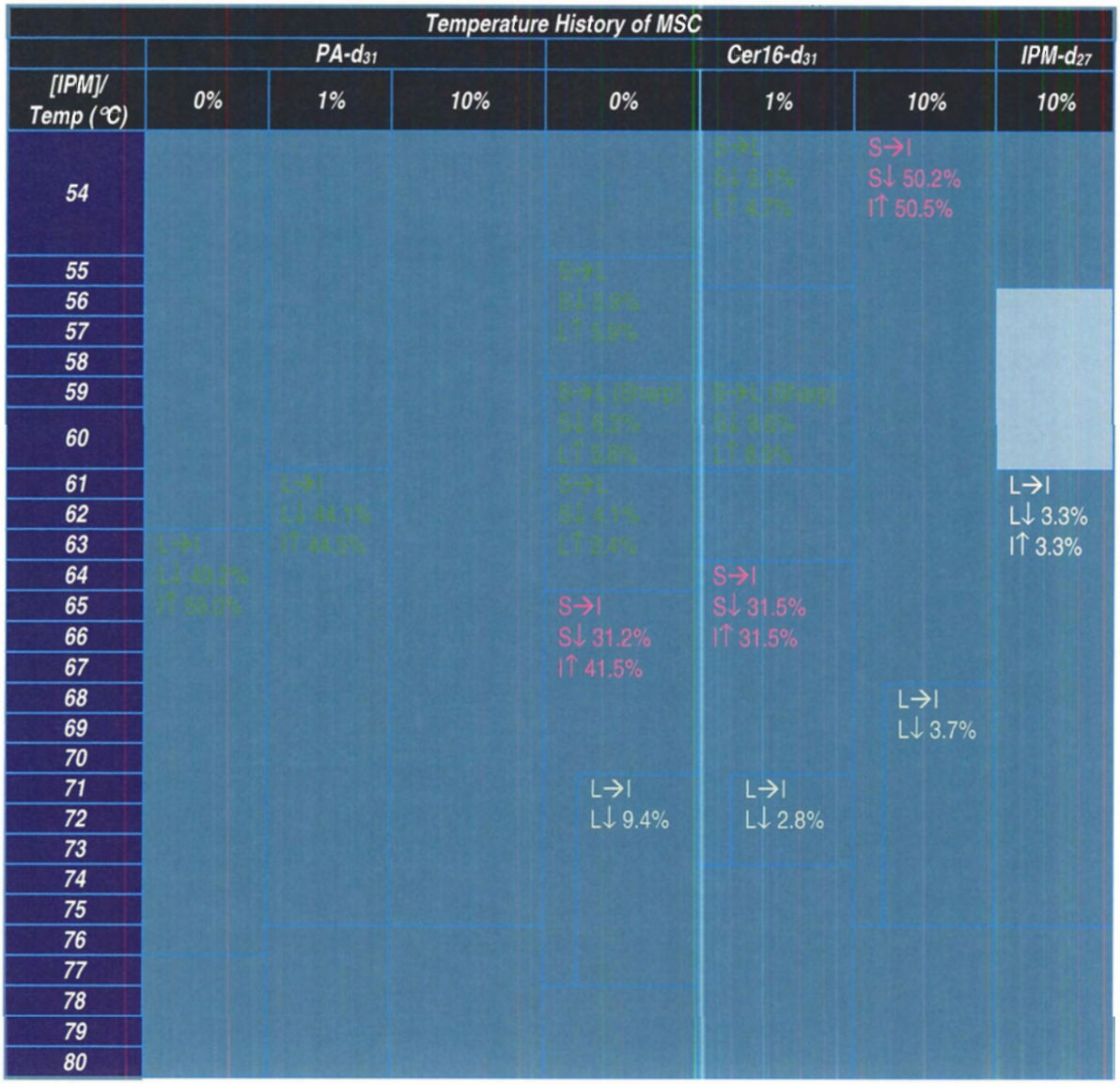

** S = Solid phase component; L = Liquid-crystalline phase component; I = Isotropic phase component

** → = Phase conversion. Note that each phase transition consists of a type of phase conversion.

** ↑ = Increase in the percentage of the specific phase component; ↓ = Increase in the percentage of the specific phase component.

CHAPTER 6: DISCUSSIONS

Even though transdermal drug delivery (TDD) has been investigated for decades, only a few studies were completed to observe the penetration enhancement of IPM in TDD, since IPM is a very recently found chemical penetration enhancer (CPE). Most of these studies focus on whether the drug permeation efficiency could be enhanced by IPM or IPM in binary/ternary CPE systems where IPM is used in combination with one or two additional CPE to complement the effect of IPM. These studies were mostly conducted *ex vivo* or *in vitro* in real stratum corneum (SC). In order to gain more understanding of the effect of IPM in SC, it would be ideal to study the penetration enhancement of IPM in a model system. Until now, no complete study of IPM in model systems is available. Thus, by conducting this ^{2}H-NMR study of IPM in a model stratum corneum (MSC), we were able to achieve more knowledge about the behaviour of IPM in MSC and biophysical responses of individual membrane components of MSC to IPM. Since no other model study of IPM is available, we are only able to compare our results to the few relevant studies of IPM in real SC that have investigated IPM as the CPE without additional combinatory CPEs.

This chapter begins with the summary of MSC phase property changes in the presence of IPM. Since 10% IPM (mol/mol) has a significant effect on MSC phase properties, we closely examine and compare the phase behaviour of Cer16-d_{31}, PA-d_{31}, and IPM-d_{27} in MSC containing 10% IPM in order to gain more understanding of how Cer16-d_{31} and PA-d_{31} behave in response to IPM and the behaviour of IPM in MSC, and

then compare our study to previous studies of IPM as a CPE in real SC. Finally, the roles of IPM as a CPE in various TDD systems/studies are outlined, and we demonstrate that the mechanisms of penetration enhancement by IPM are very specific and consistent with our ^{2}H-NMR findings.

6.1 Phase property changes of MSC and deuterated membrane components upon the addition of IPM

This section will summarize the results and discuss the general effects of IPM in perturbing the phase properties of MSC. By comparing the phase information of the three deuterated membrane components (Cer16-d_{31}, PA-d_{31} and IPM-d_{27}), this section will recapitulate the phase behaviour of Cer16, PA and IPM in MSC containing 10% IPM, since 10% IPM causes greater perturbations of the phases of MSC than 1% IPM. These phase property changes were dependent on the differences in the physical and molecular structure of membrane components. The concentration dependence of these phase perturbations will also be discussed. Finally, the similarity in phase perturbation mechanisms between IPM and oleic acid (OA), another CPE that has been studied in our lab (Rowat *et al.*, 2005), will be discussed.

6.1.1 Summary of ^{2}H-NMR results: temperature-dependent phase composition, behaviour and transitions of MSC with or without IPM

The phase compositions of MSC with and without IPM are significantly different from each other. The phase composition of MSC without IPM does not include the isotropic phase until at higher temperatures (65°C); whereas, the phase composition of MSC with IPM includes all phases at all temperatures (Figure 37).

The phase behaviour is different in MSC with or without IPM as well. Below T_m, the solid phase component of MSC without IPM is well maintained; whereas, that of MSC with IPM is reduced and an isotropic phase component appears (Figure 27 and Figure 32). Above T_m, the liquid-crystalline phase component of MSC without IPM is stable; whereas, that of MSC with IPM is reduced and the isotropic phase component is enlarged (Figure 27 and Figure 32).

These observations indicate that the presence of IPM causes poorly retained solid phase component, large changes in the amount of liquid-crystalline phase and appearance of isotropic phase component at low temperatures.

The type of phase transition is lipid-specific and concentration-dependent. In MSC with or without IPM, the first phase transition consists of a major solid to liquid-crystalline phase conversion (PA-d_{31} and Cer16-d_{31}); however, the subsequent phase transitions are different in MSC containing PA-d_{31} and Cer16-d_{31} and are dependent at different concentrations of IPM (Figure 28 and Figure 33). Table 4 illustrates these differences:

Table 4: Summary of phase transitions in MSC with or without IPM.

The phase transitions are labelled # 1 ~ 4. The type of each phase transition is listed for MSC containing different deuterated membrane lipids at different concentrations of IPM.

# Phase transition	PA-d_{31}			Cer16-d_{31}			IPM-d_{27}
[IPM]	0%	1%	10%	0%	1%	10%	10%
1	S → L	S → L	S → L	S → L	S → L	S → L	I → L
2	L → I	L → I	L → I	S → L	S → L	—	L → I
3			S → I	S → I	S → I	S → I	
4				L → I	L → I	L → I	

** S = Solid phase component; L = Liquid-crystalline phase component; I = Isotropic phase component

** → = Phase conversion. Note that each phase transition consists of a type of phase conversion.

The fact that Cer16-d_{31} has a delayed liquid-crystalline to isotropic phase transition compared to PA-d_{31} indicates that IPM preferentially influences the liquid-crystalline phase domain of PA-d_{31} more than that of Cer16-d_{31}. 10% IPM causes an additional solid to isotropic phase transition in MSC containing PA-d_{31} and the absence of the second solid to liquid-crystalline phase conversion in MSC containing Cer16-d_{31}. These differences also suggest that the effect of IPM on the type of phase transition is concentration-specific.

The phase transition temperatures are different in MSC with or without IPM as well. In the presence of IPM, the first phase transition (T_m) shifts to a higher temperature in MSC containing either PA-d_{31} or Cer16-d_{31}; whereas, the second phase transition in MSC containing PA-d_{31} (the liquid-crystalline to isotropic phase conversion) and the third phase transition in MSC containing Cer16-d_{31} (the solid to isotropic phase conversion) shift to lower temperatures (Figure 29 and Figure 34, Table 3 and Table 4). The change in the phase transition temperatures indicates that IPM disrupts the phase structure of MSC.

6.1.2 Phase behaviour and phase composition of deuterated membrane components in MSC

This section will outline comparisons of the spectral features, phase behaviour and phase composition among all deuterated membrane components in the 3:3:3:1 Cer16:Chol:PA:IPM sample.

6.1.2.1 The ^{2}H-NMR spectra of Cer16-d_{31}, PA-d_{31} and IPM-d_{27} in MSC containing 10% IPM

Figure 38 shows the ^{2}H-NMR spectra of individual deuterated membrane components at 25°C, 32°C, 50°C and 65°C.

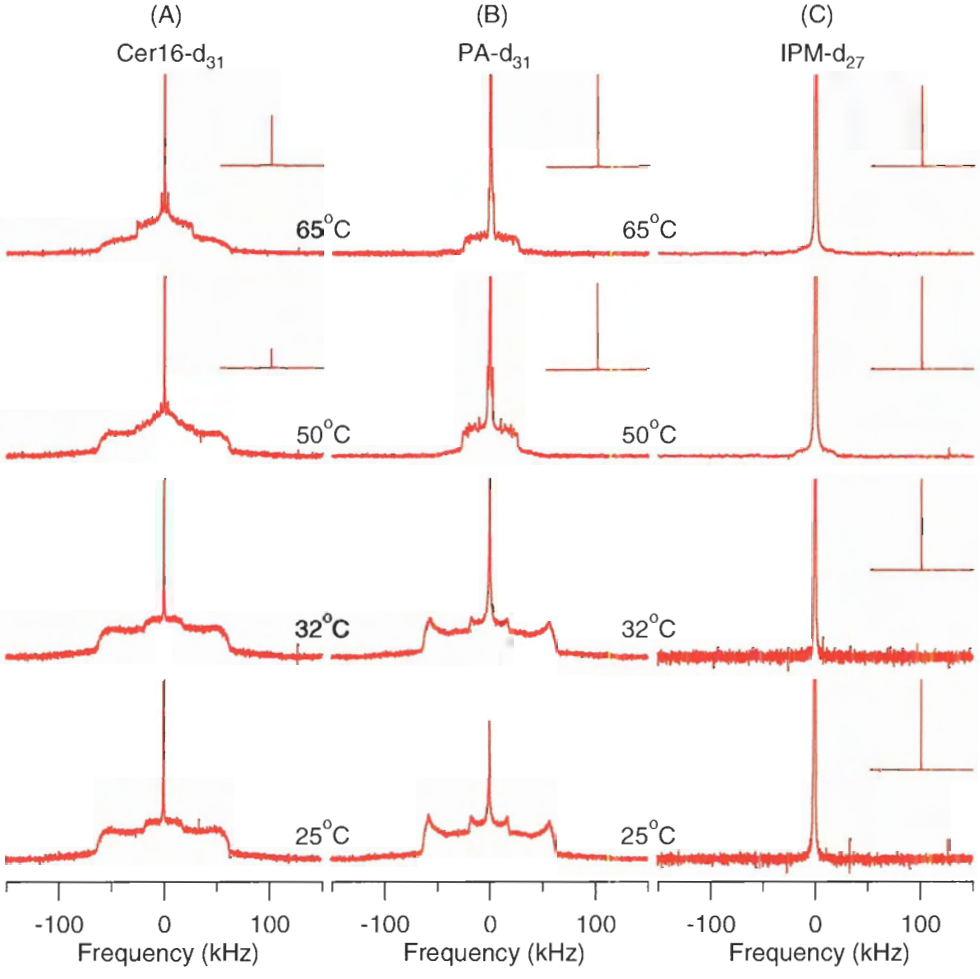

Figure 38: The ^{2}H-NMR spectra demonstrating the effect and behaviour of 10% IPM in MSC containing Cer16-d_{31}, PA-d_{31} or IPM-d_{27} at different temperatures, pH = 5.2.

(A) 3:3:3:1 Cer16-d_{31}:Chol:PA:IPM; (B) 3:3:3:1 Cer16:Chol:PA-d_{31}:IPM; (C) 3:3:3:1 Cer16:Chol:PA:IPM-d_{27}. Non-truncated spectra are displayed as insets. The spectra of (C) at 50°C and 65°C are apodized to reveal the spectral features obscured by the isotropic truncation effect. All spectra are area-normalized for comparison.

All ^{2}H-NMR spectra in Figure 38 are area-normalized for comparison of signal intensity and quantity from different phases. At temperatures below T_m (25°C and 32°C), Cer16-d_{31} and PA-d_{31} mainly exhibit signals from the solid phase with a relatively small signal from the isotropic phase, whereas IPM-d_{27} exhibits 100% isotropic phase signal. Note that both Cer16-d_{31} and PA-d_{31} spectra have similar solid phase signals, consisting of two characteristic Pake doublets with quadrupolar splitting of 38 kHz and 126 kHz approximately. Cer16 has a more "rounded" spectrum and thus the Pake doublets are not as well-defined as those in the PA-d_{31} spectrum. This is also observed in the absence of IPM and has been attributed to the shorter T_1 relaxation time found for Cer16-d_{31} compared to PA-d_{31} (Moore *et al.*, 1997). Both the rounded spectrum and the shorter T_1 imply that Cer16-d_{31} experiences some molecular motion and is not packed as tightly as PA-d_{31}. At temperatures above T_m (50°C and 65°C), Cer16-d_{31} still exhibits signals mainly from the solid phase, while PA-d_{31} displays signals mainly from the liquid-crystalline phase signal, and IPM-d_{27} shows signals from the isotropic phase and a developing liquid-crystalline phase.

6.1.2.2 M_1 and the phase behaviour of Cer16-d_{31}, PA-d_{31} and IPM-d_{27} in MSC

Figure 39 compares M_1 and the phase behaviour of individual deuterated membrane components as a function of temperature.

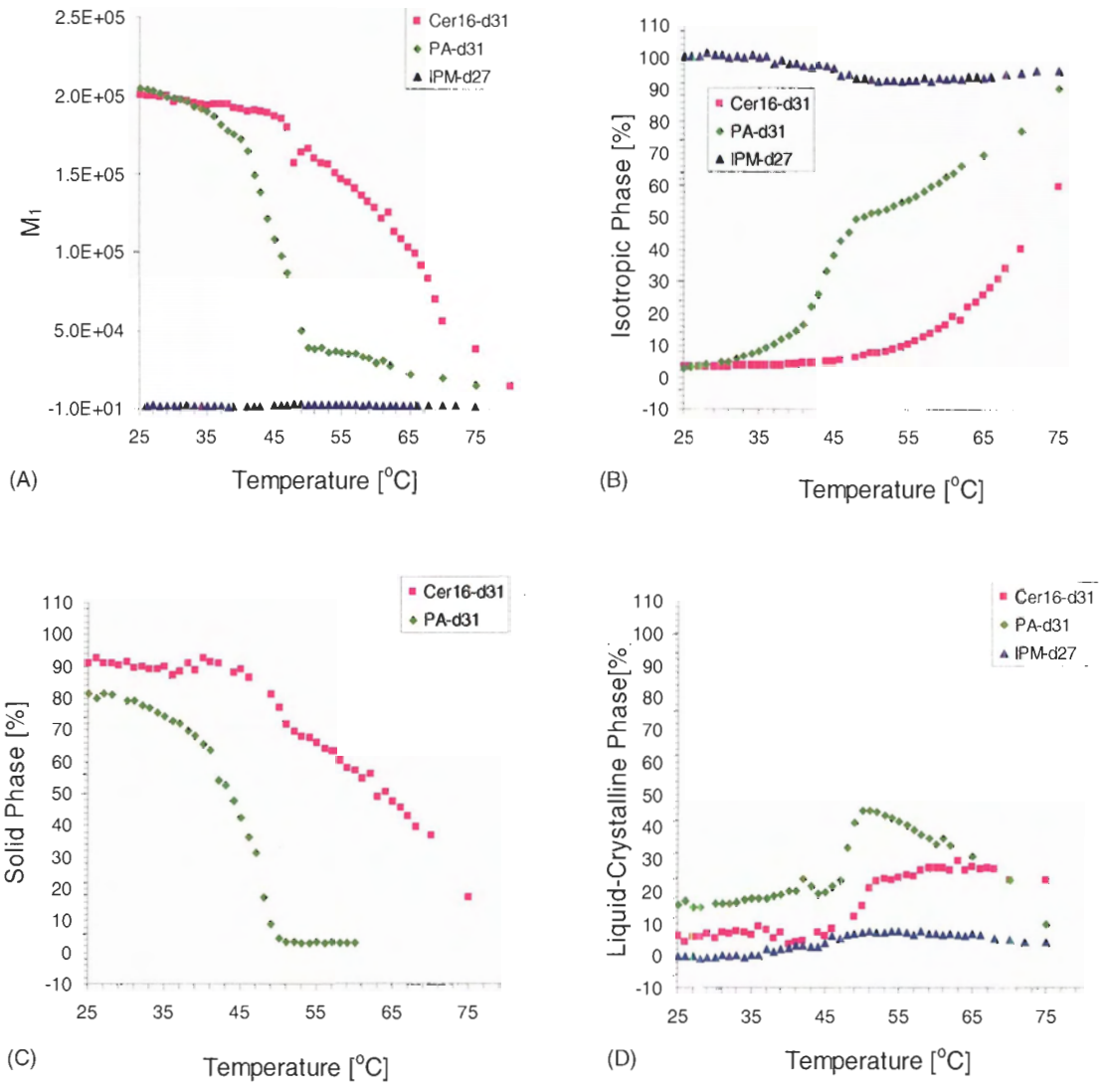

Figure 39: The M_1 and phase behaviour of Cer16-d_{31}, PA-d_{31} and IPM-d_{27} in MSC containing 10% IPM.

The (A) M_1 value (sec^{-1}) and percentage of (B) Isotropic; (C) Solid; (D) Liquid-crystalline phase component in the 10% IPM sample (3:3:3:1 Cer16:Chol:PA:IPM) containing Cer16-d_{31}, PA-d_{31} or IPM-d_{27} as a function of temperature, pH = 5.2. Error is estimated to be ± 1% of the value of the percentage of each phase component for MSC containing Cer16-d_{31}, PA-d_{31} or IPM-d_{27}.

Figure 39A shows M_1 of individual deuterated membrane components as a function of temperature. M_1 is the average spectral width which is proportional to the average order of the membrane lipid component (Refer to Section 3.5.3 for M_1). The

gradual, low-temperature (28°C ~ 41°C) and sharp, high-temperature (41°C ~ 50°C) decreases of M_1 of PA-d_{31} than that of Cer16-d_{31} (25°C ~ 47°C; 47°C ~ 48°C) indicates that the order of PA-d_{31} is not well maintained as that of Cer16-d_{31}. Since IPM-d_{27} is largely isotropic at all temperatures, its M_1 is near zero.

Figure 39B shows the percentage of the isotropic phase of individual deuterated membrane components as a function of temperature. PA-d_{31} shows a faster increase in the isotropic phase component at a lower temperature than Cer16-d_{31}. Cer16-d_{31} does not display a major increase in the isotropic phase until higher temperatures. This indicates that PA-d_{31} is more influenced and undergoes more isotropic motion than Cer16-d_{31}. At temperatures between 36°C and 48°C, IPM-d_{27} shows a minor decline in the isotropic phase (and a minor increase in the liquid-crystalline phase) which is restored partially at higher temperatures ($\geq$ ~ 61°C).

Figure 39C shows the percentage of the solid phase of individual deuterated membrane components as a function of temperature. The solid phase of MSC containing 10% IPM, interestingly, consists of Cer16 and PA only. IPM-d_{27} never shows signals of partitioning into the solid phase domain. PA-d_{31} shows a lower-temperature (25°C ~ 41°C) and faster (41°C ~ 51°C) decrease of the solid phase component than Cer16-d_{31}, and the amount of PA-d_{31} solid phase is reduced to nearly zero percent at temperatures above 51°C. This indicates that the integrity of the solid phase in MSC with IPM is retained mostly by Cer16, since above 51°C any remaining solid phase is composed of Cer16 with or without cholesterol.

Figure 39D shows the percentage of the liquid-crystalline phase of individual deuterated membrane components as a function of temperature. The liquid-crystalline phase initially consists of Cer16 and PA only. The major increase of PA-d_{31} liquid-crystalline phase occurs at a lower temperature than that of Cer16-d_{31} (45°C and 48°C, respectively). This indicates that PA-d_{31} partitions into the liquid-crystalline phase domain at a lower temperature than Cer16-d_{31}. The decrease in the amount of liquid-crystalline phase of PA-d_{31} occurs at a much lower temperature than that of Cer16-d_{31} (51°C and 68°C, respectively). This suggests that PA-d_{31} only stays in the liquid-crystalline phase domain for a narrow range of temperatures and then, partitions into the isotropic phase domain faster than Cer16-d_{31}. The increase in the amount of IPM-d_{27} liquid-crystalline phase (36°C ~ 48°C) indicates that IPM partition into the liquid-crystalline domain at this temperature range.

6.1.2.3 The phase domain competition among membrane lipid components is temperature-dependent

These observations suggest a temperature-dependent correlation of phase domain partitions of membrane lipids. First, PA partitions from the solid into the isotropic phase domain during which IPM partitions from the isotropic into the liquid-crystalline phase domain. When PA starts partitioning from the solid into the liquid-crystalline phase domain, the partitioning of IPM into the liquid-crystalline phase domain increases. When Cer16 starts partitioning from the solid into the liquid-crystalline phase domain, the partitioning of IPM into the liquid-crystalline phase domain stops. During the progress of Cer16 partitioning into the liquid-crystalline phase domain, PA stops partitioning into the liquid-crystalline domain, but rather starts partitioning from the liquid-crystalline into the

isotropic phase domain. At higher temperatures, due to thermal effect, Cer16 starts partitioning from the solid and partially from the liquid-crystalline into the isotropic phase domain, and IPM partitions back to the isotropic phase domain as well. Thus, we could speculate that at lower temperatures, IPM extracts PA and to a lesser extent Cer16 until PA solid phase melts and converts into PA liquid-crystalline phase. IPM partitions into this PA-rich liquid-crystalline phase and extracts PA from the liquid-crystalline phase domain. At higher temperatures, the IPM extraction of PA leads to enhanced phase separation containing PA and IPM (thus, partially regained isotropic phase component of IPM). Cer16 partitioning into the liquid-crystalline phase domain apparently reduces the solubility of PA and IPM in this domain. Possible reasons for this include the larger physical structure of Cer16 than PA and IPM which limits them from staying in the liquid-crystalline phase domain, higher solubility or partition coefficient of PA and IPM in the isotropic than in the liquid-crystalline phase domain, and less solubility of PA and IPM in a Cer16-rich phase domain. These observations suggest a competition among membrane lipids in the liquid-crystalline and isotropic phase domains, and the competition is temperature-dependent.

6.1.2.4 Summary

These figures demonstrate that IPM, at 10% (mol/mol) concentration, influences the phase composition and behaviour of MSC by mainly affecting PA and partially influencing Cer16, leading to an overall decrease in the solid/liquid-crystalline phases and increase in the isotropic phase. IPM partitions between liquid-crystalline and isotropic phase domains which may also contribute to the disruption of MSC phase

composition/domains. The overall integrity of MSC solid phase is primarily sustained by Cer16.

The change in the membrane phase composition, behaviour and transition upon addition of IPM indicates that IPM disrupts the membrane molecular packing. The disruptions could be the result of either IPM extracting the lipids from the membrane or IPM intercalating between membrane components (Suhonen *et al.*, 1999). If IPM extracts lipids, then intermolecular spaces can be created. On the other hand, if IPM intercalates between the lipids, then there will be weaker molecular bonds among the lipid species, also leading to increased membrane fluidity. The extraction of membrane lipid components leading to the formation of pores and/or the intercalation of IPM leading to weakened intermolecular bonding would result in an increased disorder in MSC. We have shown that the action of IPM on MSC is lipid-specific and concentration-specific. This will be further discussed in Section 6.1.3 and Section 6.1.4.

6.1.3 Physical and molecular comparisons among PA, Cer16 and IPM

The fact that Cer16-d_{31} and PA-d_{31} display different phase behaviour could demonstrate that membrane components are affected individually by IPM and independently from each other. Cer16 is more ordered than PA and less affected by IPM, which is shown by the similar M_1 values with or without IPM, insignificant changes in the solid phase, and less reduced liquid-crystalline phase in MSC containing Cer16-d_{31} (Figure 32 and Figure 34). The different responses of Cer16-d_{31} and PA-d_{31} to IPM could be due to the different physical and molecular structures between Cer16 and PA, or the similar physical and molecular structures between PA and IPM.

The different molecular structures of Cer16 and PA may explain the higher M_1 values and minor changes measured in Cer16-d_{31} compared to PA-d_{31}. Cer16 has a hydrophilic head group attached with a fatty acyl chain and an amide-linked acyl chain on a hydrocarbon backbone, which makes Cer16 a very large molecule; whereas, PA has a small hydrophilic head group (carbonyl group) and one fatty acyl chain, which allows PA to move more freely in the bilayer. The head groups of Cer16 molecules may hydrogen-bond with each other (Pascher, 1976) when they rearrange at different temperatures and thus form a much more ordered membrane structure preventing IPM from intercalating. The small increase in the M_1 value during the phase transition in MSC containing Cer16-d_{31} suggests that the order of the membrane bilayer may have been restored by the rearrangement of Cer16 molecules (Figure 32A).

The similar structure of IPM to that of PA allows IPM to be in rapid motions and its close association with PA. The 14-carbon acyl chain of IPM has a stabilizing effect on its integration into 16-carbon PA bilayers (deep into the hydrophobic core of the lipid bilayers). Both IPM and PA include a carbonyl group in their head group. These similar physical natures permit greater degrees of IPM solvation and extraction of PA. Simple IPM movements would be allowed into and out of the MSC/SC bilayers, particularly PA domains, leading to possible spontaneous formation of micelles or micellar structures consisting of IPM and PA. These micelles may form either inside or outside the MSC/SC membranes, similar to the semi-micellar formation of single-chained lysolipids inside pure dipalmitoylphosphatidylcholine (DPPC) bilayers (Mills *et al.*, 2005), or the micellar formation of lipids outside the bilayers (Bouwstra *et al.*, 2003). Although IPM is shown to extract Cer16 in our study as well (causing it to undergo isotropic motion at low

temperatures), the uncommon physical natures between the two may inhibit IPM from extracting Cer16 until at a higher concentration, where a higher number of available IPM molecules would eventually have impact on Cer16.

The fact that the structure of IPM is more similar to that of PA than that of Cer16 permits a better association between IPM and PA, which allows IPM to have a more pronounced effect on PA than Cer16. The similar structure of IPM to FFA contributes to higher FFA content (mainly the liquid-crystalline phase domain) and causes greater solvation effect on the MSC and SC membranes (Nelson and Cox, 2000). Thus, the fact that the effect of IPM on MSC is lipid-specific can be rationalized.

6.1.4 The phase property changes of MSC are IPM-concentration-dependent

Higher concentrations of IPM result in greater perturbations of the phase composition and behaviour in MSC. 1% IPM does not have a pronounced effect on MSC. This phenomenon is also observed in the study of ethanol (EtOH) as a CPE. A higher concentration of EtOH increases the skin permeability by extracting lipids from SC membrane such that intermolecular spaces become larger which leads to the pore formation in SC membrane (Suhonen *et al.*, 1999). A lower concentration of EtOH is found to increase the membrane fluidity but only cause slight disorder in the acyl chain region of SC membrane (Suhonen *et al.*, 1999). In similar ways, a higher concentration of IPM would extract SC lipids (which undergoes a greater degree of isotropic motion) to increase intermolecular spaces. A lower concentration of IPM, on the other hand, would have less effect of extraction and only interdisperse in SC membrane due to fewer

molecules, which may not result in enhanced pore formation, but may increase membrane fluidity.

Talk about IPM, indicating that it does not matter whether at high or low concentrations of IPM, at low including physiological temperature, IPM creates a minor fluidization effect, but not so dramatic as observed at high temperatures which is suggested to be less harmful to SC membrane components.

6.1.5 Comparing the effect and behaviour of IPM with the effect and behaviour of oleic acid in MSC

Oleic acid (OA) is an 18-carbon FFA with a cis double bond at carbon 9. The effect of OA as a CPE in MSC was observed in a previous ^{2}H-NMR study in MSC containing PA-d_{31}, Chol-d_6 (deuterated cholesterol) or OA-d_2 (deuterated oleic acid) (Rowat *et al.*, 2005). The effect and phase behaviour of IPM are found to be similar to those of OA. First, in the presence of IPM or OA, PA-d_{31} develops an isotropic phase component at lower temperatures. Second, the phase behaviour of IPM-d_{27} is similar to that of OA-d_2. Third, a competition mechanism in the liquid-crystalline phase domain of MSC containing either IPM or OA is observed. Finally, the similar physical nature between IPM and OA allow them to extract PA from the solid phase domain at lower temperatures, and from the liquid-crystalline phase domain at higher temperatures. Since OA was added to MSC in large amount (16.67% and 25.00% in 2:2:1:1 and 1:1:1:1 BBCer:Chol:PA:OA, respectively, mol/mol; BB = Bovine Brain), we would compare the effect and behaviour of OA to those of 10% IPM primarily.

The addition of OA causes changes in the phase composition of MSC containing PA-d_{31}. In the presence of OA, at temperatures below T_m (~ 42°C), an isotropic phase of PA-d_{31} is observed and at T_m, it reaches 90% and 94% (2:2:1:1 and 1:1:1:1 BBCer:Chol:PA-d_{31}:OA, respectively). At temperatures just above T_m, the amount of PA-d_{31} isotropic phase decreases to 52% and 88%, respectively. At higher temperatures, the amount of PA-d_{31} isotropic phase increases again to a maximum of 90% and 100%, respectively, while both the liquid-crystalline phase component of PA-d_{31} is reduced (Rowat *et al.*, 2005). The observation of reduced onset temperature of PA-d_{31} isotropic phase in MSC containing OA is consistent with the behaviour of PA-d_{31} in MSC containing IPM. However, in the presence of IPM, the amount of PA-d_{31} isotropic phase does not decrease at any temperature (Figure 27B). Also, T_m of PA-d_{31} in MSC containing IPM and OA are different. T_m is increased in the presence of IPM, but unchanged in the presence of OA (Figure 27 and Figure 29; Rowat *et al.*, 2005). Lastly, the amount of PA-d_{31} isotropic phase in MSC containing IPM never reaches 100%.

The phase behaviour of IPM and OA are similar in MSC. Both IPM-d_{27} and OA-d_2 show 100% isotropic motion at temperatures below T_m (Figure 37 and Figure 39B; Rowat *et al.*, 2005). The fast isotropic motion of IPM and OA may influence the physical environment around PA and causes PA to undergo isotropic motion. It is also suggested that OA solubilizes and extracts PA from MSC membranes leading to increased isotropic phase component and induced phase separation (Rowat *et al.*, 2005). The fast isotropic motion of IPM may influence Cer16 and PA with same mechanisms as well, in which IPM is suggested to extract Cer16 and PA from MSC membrane (Figure 27, Figure 29, Figure 32 and Figure 34). At temperatures just above T_m, the amount of OA-d_2 isotropic

phase decreases dramatically to a minimum of 60%. At higher temperatures, the isotropic motion of OA-d_2 is completely restored (Rowat *et al.*, 2005). IPM-d_{27} shows a decrease in its isotropic phase component at temperatures near T_m, but this is not as dramatic as OA-d_2. The decrease in the isotropic phase component corresponds to the increase in the liquid-crystalline phase component in both IPM-d_{27} and OA-d_2 (Figure 37 and Figure 39B; Rowat *et al.*, 2005).

In MSC containing OA, a competition among membrane lipid components in the liquid-crystalline phase domain is also observed, although it is slightly different from that in MSC containing IPM. Below T_m, a significant amount of PA partitions into the isotropic phase domain in MSC containing OA; whereas, only a small amount of PA does so in MSC containing IPM. At temperatures near T_m, a significant amount of both PA and OA partition from the isotropic into the liquid-crystalline phase domain in MSC containing OA; whereas, only a small amount of IPM does so in MSC containing IPM. At higher temperatures, PA is extracted from the liquid-crystalline phase domain and phase separated with OA or IPM in MSC containing OA or IPM, respectively. However, there is no data obtained from deuterated BBCer, so we are not able to speculate the competition of BBCer in the liquid-crystalline phase, and compare to that of Cer16 in MSC containing IPM.

OA and IPM have similar molecular structures. They are both lipid-soluble which enables them to intercalate into the membrane and extract lipid components. OA is suggested to induce phase separation from the MSC lipid bilayers (Rowat *et al.*, 2005). IPM may induce phase separation like OA as well.

Several differences between the effect and phase behaviour of IPM and those of OA can be explained. First, the minimum percentage of isotropic phase is lower in OA than in IPM, which shows that OA partitions more into the liquid-crystalline phase domain. This may be due to the higher OA concentrations applied than the IPM concentration (2:2:1:1 or 1:1:1:1 BBCer:Chol:PA:OA), which might enhance the ability of OA to partition into the liquid-crystalline phase domain. It could also be due to the use of BBCer by Rowat *et al.* which is a mixture of ceramides and includes a range of chain lengths and even some unsaturated chains (e.g. nervonic acid). This may create a liquid-crystalline phase domain more susceptible to OA intercalation/partitioning. Also, OA is likely more chemically & physically similar to PA (lack of the isopropyl group) than IPM, since both OA and PA are fatty acids. This may make OA physically more able to intercalate into the liquid crystalline phase domain.

The unchanged T_m in the presence of OA may be due to the BBCer composition. Since it contains various ceramides including some unsatuarated ceramides, BBCer may have a poorly defined, broad melting transition compared to the pure Cer16. If the solid phase is primarily composed of a mixture of ceramides (including some having lower T_m) instead of pure Cer16 (higher T_m), the T_m of this solid phase could be envisioned to remain constant.

Lastly, both IPM and OA partition into the liquid-crystalline phase domain. At higher temperatures, a small amount of IPM remains in this domain, whereas OA regains 100% isotropic motion.

Since the effect and behaviour of IPM and OA are similar, we can speculate the behaviour of cholesterol in MSC containing IPM based on the ^{2}H-NMR data from Rowat

et al. In the presence of OA, Chol-d_6 shows an isotropic phase component at lower temperatures (Rowat *et al.*, 2005). At T_m (~ 42°C), the Chol-d_6 solid phase converts into the Chol-d_6 liquid-crystalline phase but not completely, and the amount of Chol-d_6 isotropic phase increases (Rowat *et al.*, 2005). At higher temperatures, the amount of Chol-d_6 isotropic phase increases gradually with increasing temperatures (Rowat *et al.*, 2005). The continuous increase of Chol-d_6 isotropic phase component indicates that Chol does not partition from the isotropic into solid or liquid-crystalline phase domains at any temperature (permanently phase separated). These observations suggested that Chol is gradually extracted from MSC membranes. The same mechanism may occur in MSC containing IPM as well, where IPM could extract Chol and induce phase separation of Chol from MSC membranes.

6.2 Comparison of the behaviour and actions of IPM in MSC and SC

In Section 6.1, we discussed the phase property changes of MSC and deuterated membrane components (PA-d_{31}, Cer16-d_{31} and IPM-d_{27}) in the presence of IPM. We observed that these changes are temperature-, concentration- and lipid-specific. In Section 6.2, we will summarize these changes into four major behaviours/actions of IPM and carefully compare these ^{2}H-NMR findings with the results from previous studies of IPM as CPE in SC. In particular, we will discuss the comparison with the results from the *in vitro* study by Brinkmann and Müller-Goymann (Brinkmann and Müller-Goymann, 2003) in more details as it is the basis of our ^{2}H-NMR study of IPM in the model system. Then, we will look into other factors that may contribute to the behaviours/actions of IPM in both SC and MSC. We found that IPM, has a similar role/mechanism of

penetration enhancement in both SC and MSC and its behaviour is, surprisingly, independent of the presence of a second or a third CPE.

6.2.1 The behaviour and actions of IPM in MSC and SC

The four behaviours/actions of IPM are found to be specific and consistent in MSC and SC systems. First, IPM has strong association with MSC lipids, particularly PA domains. Second, IPM insertion into the MSC lipid bilayers causes increased fluidity of the MSC structure. Third, IPM extraction of MSC lipids creates additional and enlarged intermolecular spacing which contributes to even greater disorder in the MSC structure. Lastly, IPM causes a shift of the two phase transitions to different temperatures, which indicates the disruption of the phase domain structure in MSC.

^{2}H-NMR data suggested a strong interaction between IPM and MSC lipids, which was demonstrated by the change in phase behaviour and profile of PA-d_{31} and Cer16-d_{31} in MSC with IPM (Figure 27, Figure 29, Figure 32 and Figure 34). These changes indicate an alteration and disordering in the phase domains and molecular packing of PA-d_{31} and Cer16-d_{31}. This is consistent with WAXD/SAXD and DSC data on SC pretreated with formulation containing IPM (Brinkmann and Müller-Goymann, 2003). WAXD data showed that in the presence of IPM, the peak of hexagonally packed lipids shifted (0.413 nm to 0.405 nm) and the peak of corneocyte-bonded lipids disappeared (0.467 nm). This demonstrates that IPM highly associates with hexagonally packed and corneocyte-bonded lipid fractions in SC through integration and disruption. SAXD data showed a minor decrease in the peak intensity of the lipid bilayer packing (6.4 nm), which indicates that the lipid bilayer packing is disrupted in the presence of IPM. DSC data showed that the

second and the third phase transitions shifted to lower temperatures in SC pretreated with IPM (70°C to 60°C and 80°C to 75°C, respectively). The second and third phase transitions correspond to hexagonally packed lipids and corneocyte-bonded lipids, respectively. Since a shift to lower phase transition temperatures suggests increased disorder of the lipid bilayers (Hirvonen *et al.*, 1995), these DSC observations would suggest the loss of order in hexagonally packed and corneocyte-bonded lipid matrices. As MSC simulates the intercellular lipid portion of SC, the loss of order in MSC lipid microstructure also indicates the loss of order in SC intercellular lipid microstructure. The more disordered MSC and SC lipid microstructure in the presence of IPM shows that IPM and its effect of penetration enhancement are highly associated with MSC and SC lipids.

IPM associates with MSC lipids in two mechanisms: integration/insertion and extraction. ^{2}H-NMR data showed that in MSC with IPM, the isotropic phase of PA and Cer16 has an onset at a lower temperature than in MSC without IPM, causing reduced solid (at lower temperatures) and liquid-crystalline (at higher temperatures) phases which leads to increased membrane fluidity. Note that previous research has shown that the solid phase is composed of orthorhombically packed lipids and the liquid-crystalline phase is composed of hexagonally packed lipids (Bouwstra *et al.*, 1997). ^{2}H-NMR data also showed that M_1 is lowered in MSC containing IPM. Remember that M_1 is the average spectral width and is proportional to the order of MSC structure (Refer to Section 3.5.3). These results indicate that the IPM presence causes a more fluidic and disordered MSC structure which could be explained by the IPM insertion into the MSC lipid bilayers. This is consistent with WAXD/SAXD data on SC pretreated with IPM

(Brinkmann and Müller-Goymann, 2003). WAXD data showed that the peak of hexagonally packed lipids shifted to a lower spacing value in the presence of IPM. This indicates that the hexagonal lipid packing distance is reduced as a result of IPM insertion, which is also shown by the ^{2}H-NMR observation of IPM localization into the liquid-crystalline phase domain (Figure 39B & Figure 39D). The WAXD peak of orthorhombically packed lipids did not show any change which suggested that IPM does not affect the order of the solid phase. The ^{2}H-NMR data showed consistent results, where the solid phase component of MSC is reduced but the order is not influenced in the presence of IPM. This suggests that IPM would only reduce the orthorhombically packed lipid portion in SC. SAXD data showed that the peak intensity of the SC bilayer packing was reduced in the presence of IPM, which indicates that the bilayer packing is also disrupted as a result of IPM insertion. These data demonstrated that IPM associates with MSC and SC lipids by reducing the lipid lateral packing distance and disrupting the lipid bilayer packing structure through integration/insertion, which causes increased membrane fluidity in both MSC and SC.

IPM also associates with MSC lipids through extraction. ^{2}H-NMR data showed that in the presence of IPM, a small percentage of both PA and Cer16 undergo isotropic motion already at 25°C (Figure 27, Figure 29, Figure 32 and Figure 34). This indicates that at lower temperatures, IPM extracts PA and Cer16 (from the solid phase domain) and causes increased isotropic phase component of MSC lipids. At higher temperatures, IPM extracts PA (from the liquid-crystalline phase domain) and Cer16 (mainly from the solid and partially from the liquid-crystalline phase domains) causes increasing isotropic phase of MSC lipids. Greater intermolecular spaces are created as a result, leading to a highly

disordered MSC structure. Both SAXD and DSC data on SC pretreated with IPM (Brinkmann and Müller-Goymann, 2003) support this ^{2}H-NMR finding. The decrease in the SAXD peak intensity of the lipid bilayer packing (6.4 nm) could be due to the IPM extraction of lipids from the SC lipid bilayers in addition to the IPM insertion, since IPM extraction would also disrupt the lipid bilayer packing. The shift of the second and third phase transitions to lower temperatures in the DSC thermogram could also be due to the IPM extraction of hexagonally packed lipids (in addition to IPM integration) and corneocyte-bonded lipids in SC, respectively, since the IPM extraction of SC lipids would contribute to even greater fluidity and disorder of the SC lipid bilayers. However, the IPM extraction effect is not observed in WAXD data. The WAXD peaks did not shift to greater lipid lateral packing spaces, which does not provide support for the proposed IPM extraction of SC lipids to create a less densely packed SC lipid structure.

Both ^{2}H-NMR and DSC data showed the shift of phase transitions to different temperatures in MSC or SC containing or pretreated with IPM. IPM causes the shift of the solid to liquid-crystalline phase transition to a higher temperature, and the shift of the liquid-crystalline to isotropic phase transition (PA-d_{31}) and the solid to isotropic phase transition (Cer16-d_{31}) to a lower temperature in MSC. The shift of the solid to liquid-crystalline phase transition to a higher temperature in MSC with IPM containing either PA-d_{31} (Figure 27 and Figure 29, Table 3) or Cer16-d_{31} (Figure 32 and Figure 34, Table 3) agrees with the IPM extraction model supported by SAXD data in SC pretreated with IPM, despite of the lack of DSC data support. DSC results did not provide detectable data on the first phase transition (the solid to liquid-crystalline phase transition) due to variation in SC compositions from individual donors. The shift of the solid to liquid-

crystalline phase transition to a higher temperature may be due to the initial IPM extraction of the MSC/SC lipids (primarily PA, and mostly from the solid phase domain in MSC or orthorhombically packed lipid fractions in SC), leading to a solid phase or orthorhombic lipid matrix consisting of primarily Cer16. Since Cer16 has a higher melting temperature than PA, the solid phase consisting of primarily Cer16 would have an increased solid to liquid-crystalline phase transition temperature. We suggest that the same mechanism may occur in SC as well.

The liquid-crystalline to isotropic phase transition of PA-d_{31} occurs at 61°C and 51°C in MSC containing 1% IPM and 10% IPM, respectively (Figure 29, Table 1). This phase transition corresponds to the second phase transition in SC (hexagonally packed lipids) since the third phase transition in SC corresponds to corneocyte-bonded lipids which are not included in the MSC lipid composition. The shift of the liquid-crystalline to isotropic phase transition to a lower temperature observed in MSC is consistent with the decrease in the second phase transition temperature shown by the DSC thermogram obtained in SC. The shift of the liquid-crystalline phase transition temperature indicates that both MSC and SC structures are more disordered (Hirvonen *et al.*, 1995). A similar reduction of the phase transition temperature was also observed in the DSC study of human cadaver skin treated with IPM (Leopold and Lippold, 1995). The shift of the liquid-crystalline to isotropic phase transition to a lower temperature may be due to the IPM integration into and extraction of the MSC lipids (primarily PA since IPM does not show an evidence of extracting Cer16 from the liquid-crystalline phase domain until at a much higher temperature) from the liquid-crystalline phase domain, or the SC lipids from

hexagonally packed lipid fractions. This would result in increased membrane fluidity and disorder in MSC and SC structures.

Note that the shifted liquid-crystalline to isotropic phase transition temperatures in MSC are 1°C and 11°C lower than that in SC (~ 62°C). The possible reason could be the higher disorder observed (and thus lower phase transition temperatures) in PA-d_{31} as an individual membrane component in MSC than that in SC as a whole, since SC also has other components such as keratins resisting the disordering effect of IPM on the phase transition (Suhonen *et al.*, 1999). It could also be due to the difference in the carbon chain length between MSC and SC lipids. MSC contains 16-carbon chains primarily, whereas SC contains more long-chained FFA (C22 ~ C28) (Norlén *et al.*, 1998). Since the carbon chain length is directly proportional to the phase transition temperature (X. Chen, Unpublished data), the shifted liquid-crystalline phase transition temperature in MSC would be lower than the shifted second phase transition temperature in SC. The shifts of the first (MSC only) and second (MSC and SC) phase transition temperatures suggest that the phase structures of both MSC and SC are modified by IPM.

These four IPM behaviours/actions are unique and consistent in MSC and SC. With these specific mechanisms, IPM is able to reduce the order and increase the membrane fluidity of MSC and SC structures. By doing so, IPM enhances the SC permeability and thus better drug permeation.

6.2.2 New findings of behaviour and actions of IPM in MSC and SC

^{2}H-NMR study of IPM in MSC provides new aspects to the understanding of IPM as a CPE in the previous study. First, the IPM extraction mechanism is discovered in

addition to the IPM integration model. Second, the temperature-dependent effect of IPM is carefully analyzed. Third, the IPM concentration dependence of molecular interactions is well characterized. Fourth, the IPM concentration dependence of phase quantity changes is clearly described. Last, ^{2}H-NMR allows observations of the response of individual MSC membrane components to IPM, and the molecular motion and behaviour of IPM in MSC.

Previous studies proposed the IPM insertion model and suggested that it is the major cause for decreased permeability in SC pretreated with IPM, despite of increased SC membrane fluidity and disorder (Brinkmann and Müller-Goymann, 2003). However, our ^{2}H-NMR study discovered that IPM extracts MSC lipids, and the IPM extraction results in disrupted phase behaviour, profile, composition and structure of MSC (Figure 27, Figure 29, Figure 32 and Figure 34). Thus, we propose the IPM extraction model in addition to the IPM insertion model and suggested that both IPM extraction and insertion cause an overall fluidizing and disordering effect on MSC and SC lipid microstructures.

We found that IPM effects are temperature-dependent. In previous studies, the first phase transition was not observable in SC (Brinkmann and Müller-Goymann, 2003). Our ^{2}H-NMR observations were carefully analyzed and we were able to characterize this phase transition in MSC (the solid to liquid-crystalline phase transition). We found that the increase in the first phase transition temperature (Figure 27, Figure 29, Figure 32 and Figure 34) may be caused by the initial IPM extraction of PA, resulting in a solid phase consisting of Cer16 primarily, leading to the shift of the first phase transition to a higher temperature. At higher temperatures, the effect of IPM is more pronounced. The liquid-crystalline to isotropic phase transition of PA-d_{31} in MSC, which corresponds to the

second phase transition in SC, shifts to a lower temperature (Figure 29 and Figure 34; Brinkmann and Müller-Goymann, 2003). The effect of IPM integration into the liquid-crystalline phase domain of MSC (primarily PA) or hexagonally packed lipid fractions of SC is not apparent until higher temperatures, where a significant melting of the solid phase (MSC) or orthorhombically packed lipid fractions (SC) occurs. However, since IPM is applied topically in SC, IPM may need to intercalate into the lipid bilayers at lower temperatures to penetrate through SC in order to initiate the extraction of SC lipids. Through these findings, we propose that the effect of IPM is temperature-dependent in both MSC and SC.

The concentration dependence of molecular interactions is well characterized in our ^{2}H-NMR study. A higher concentration of IPM is found to extract MSC lipids. This is evident from the observation that at temperatures between 25°C and 37°C, the isotropic phase component of PA and Cer16 increases in the presence of IPM, but the isotropic phase component of IPM does not decrease with increasing isotropic phase component of PA and Cer16 (Figure 39). This indicates that at low temperatures, a higher concentration of IPM interacts with PA and Cer16 closely via extraction (mainly from the solid phase/orthorhombically packed lipid fractions). At temperatures above 37°C, a noticeable amount of IPM localizes and integrates into the liquid-crystalline phase domain (hexagonally packed lipid fractions) to dissolve and extract more PA; whereas, IPM does not extract Cer16 in the liquid-crystalline phase domain, but it extracts Cer16 from the solid phase domain (orthorhombically packed lipid fractions) (Figure 39). This suggests that at higher temperatures, a higher concentration of IPM extracts PA (from the liquid-crystalline phase/hexagonally packed lipid fraction) and Cer16 (from the solid

phase/orthorhombically packed lipid fraction) to cause a higher disorder and a reduction of the second phase transition temperature in MSC and SC.

A lower concentration of IPM is found to have less extraction effect on the MSC lipids. This is evident from the increase in PA and Cer16 isotropic phase component at higher temperatures in the presence of a lower IPM concentration than in the presence of a higher IPM concentration (Figure 27B and Figure 32B). Since the isotropic motion of PA and Cer16 takes place at temperatures above T_m, the effect of IPM extraction at a lower concentration is not pronounced at lower temperatures. This suggests that at higher temperatures, the effect of IPM extraction at a lower concentration becomes more prominent. A lower concentration indicates fewer IPM molecules available to dissolve and extract the MSC/SC lipids, and the effect can be enhanced at higher temperatures, where a considerable amount of solid phase (MSC) or orthorhombically packed lipid fractions (SC) melt. Fewer IPM molecules may be only sufficient to be interdispersed in the lipid bilayers (particularly in the liquid-crystalline phase domain) as observed in SC treated with EtOH (Suhonen *et al.*, 1999). The IPM interdispersion may result in greater membrane fluidity, but not as significant as the IPM extraction. Previous studies did not investigate the relationship between lipid interactions and IPM concentrations. Thus, we proposed that the molecular interaction between IPM and MSC/SC lipids is concentration-dependent as well as temperature-dependent.

The concentration dependence of phase quantity changes is well described. ^{2}H-NMR data shows that the IPM concentration is inversely proportional to the amount of liquid-crystalline phase and directly proportional to the amount of isotropic phase, but it does not have effect on the amount of solid phase (Figure 28 and Figure 33). The effect is

more distinct at higher temperatures than lower temperatures. Previous studies did not look into the IPM concentration dependence of phase quantity changes nor did they suggest about the relationship between phase quantity changes and the order of SC structure. Thus, we propose that the changes in liquid-crystalline and isotropic phase quantities are concentration-dependent.

Lastly, our ^{2}H-NMR study characterized the response of individual MSC lipids to IPM, as well as the molecular motion and behaviour of IPM in MSC. ^{2}H-NMR data showed clearly that IPM has a greater effect and interacts more with PA than Cer16. The constant isotropic motion of IPM explains its high and close interactions with MSC lipids and its disruption of MSC phase properties. Previous studies provided insights into only the possible interaction mechanisms of IPM with SC, for example, the IPM integration into SC lipids. With our ^{2}H-NMR results, we proposed that the effect and interaction of IPM with each MSC/SC lipid is different and independent of each other.

These new findings provide different insights into the understanding of IPM interactions with MSC/SC lipids. While previous studies suggested the IPM integration model, we propose the IPM integration/extraction model. We have also shown that the molecular interaction between IPM and MSC/SC lipids, phase quantity changes and lipid responses to IPM are temperature-, concentration- and lipid-dependent.

6.2.3 Other factors influencing the mechanism of IPM penetration enhancement

In addition to the four IPM behaviour/actions in MSC/SC, other factors may play important roles in the improvement of SC permeability. Three major factors are

hydrophilicity/lipophilicity, solubility and pH/ionization effect. The effect of these factors can be demonstrated from drug permeation studies using IPM in combination with a second CPE or chemical to make a binary CPE system to further improve TDD. These factors show that IPM, independent of the study and CPE systems used, shows a significant and unique enhancement of the skin permeability.

To make a binary CPE system, IPM (a lipophilic CPE) is usually added with another hydrophilic CPE such as EtOH (Alberti *et al.*, 2001; Fang *et al.*, 2003; Jin *et al.*, 2000). These studies have shown that EtOH/IPM greatly improves the drug permeation. Because of its high lipophilicity, IPM is able to associate more with the lipophilic regions of lipid bilayers through integration to form a continuous phase of vehicles (^{2}H-NMR data; Brinkmann & Müller-Goymann, 2003; Fang *et al.*, 2003). Thus in this binary CPE system, IPM is suggested to play the role of fluidizing the lamellar-gel phase of SC (Leopold and Lippold, 1995) and increasing the effective free volume and diffusivity in the lipophilic region (Suh and Jun, 1996). EtOH, on the other hand, is suggested to play the role of disrupting the hydrophilic regions of lipid bilayers (Suhonen *et al.*, 1999). Because of its hydrophilicity, EtOH is able to move a hydrophilic drug (for example, Mefenemic acid (MH)) through its solvent drag effect, which was supported by the linear correlation between the solubility of MH in EtOH and MH flux through the skin. (Fang *et al.*, 2003). Since the hydrophilic MH is much less soluble in the lipophilic environment, IPM was suggested to form a continuous phase of vehicles to create pathways for the EtOH-MH complex to permeate through the lipophilic regions of SC, so that the mobility of MH through this region can be improved (Fang *et al.*, 2003). This is also consistent

with the previously proposed mechanism of IPA/IPM penetration enhancement of hydrocortisone (Brinkmann & Müller-Goymann, 2003)

In addition to hydrophilicity/lipophilicity, the solubility/polarity property is also critical to the drug permeation efficiency. Two aspects should be considered: the solubility of the drug and CPE in the lipid bilayers and the solubility of the drug in the CPE. The semipolar property of IPM leads to its better solubility in the lipid bilayers and is suggested to enable IPM to modify SC to create more membrane flux of the drug that is significantly less soluble in SC, which enhances permeation (Jiang *et al.*, 1998). The solubility of the drug in the CPE also determines the membrane flux of the drug. The higher solubility of the drug in the CPE increases the amount of drug permeated through SC, but does not affect the drug solubility in SC (Brinkmann & Müller-Goymann, 2003; Fang *et al.*, 2003). In fact, only a minimal amount of the CPE with similar solubility to the drug is needed for the maximal drug permeation (Pardo *et al.*, 1990)

In addition to solubility, pH and ionization effect also play important roles in drug permeation. The solubility of hydrophilic drug is found to be positively correlated to the pH of vehicles/CPEs (due to the ionization of drug at higher pH). The increase in drug solubility in the vehicles/CPEs could compensate the slow permeation rate of hydrophilic drug through the lipophilic intercellular transport route, and the maximum permeation rate may occur at the maximum ionization of the drug (Hadgraft *et al.*, 1985). However, previous studies have shown that pH and ionization do not have effect and become unimportant on the drug permeation when IPM is present (Singh *et al.*, 2005; Suh and Jun, 1996). Suh and Jun suggested that IPM delipidizes and severely impairs SC through extraction of SC lipids (Suh and Jun, 1996), which is consistent with our ^{2}H-NMR

observations. The delipidization of SC would create spatial effect rather than pH and ionization effects for enhanced drug permeation.

These studies have shown that in a binary CPE system, the lipophilic CPE integrates into the lipophilic regions to create lipophilic pathways in SC (lipophilic transport), and the hydrophilic CPE disrupts the hydrophilic regions to create entrances into SC (hydrophilic transport). The role of IPM as a lipophilic CPE does not change in binary CPE systems containing different hydrophilic CPEs, and the role of hydrophilic CPEs is consistent in these binary CPE systems. The increase in diffusion coefficient of the drug by IPM (Suh and Jun, 1996) and the increase in partition coefficient of the drug by hydrophilic CPEs enhance TDD. The higher solubility of the drug in the CPE is found to improve the drug permeation through individual or synergistic effects, in addition to hydrophilicity/lipophilicity factor. pH and ionization effect are not prominent in the presence of IPM.

6.2.4 Comparing IPM with OA as a CPE

The similarity in the molecular structure and behaviour between OA and IPM was described earlier (Section 6.1.5). OA has been used as a CPE in various drug and permeant delivery studies, such as melatonin (Gwak *et al.*, 2002), terbinafine (Alberti *et al.*, 2001), isosorbide dinitrate (ISDN) (Gabiga *et al.*, 2000), and a very large polar molecule fluorescein isothiocyanate-dextrans (FTIC) (Ogiso *et al.*, 1995). OA is demonstrated to be a better CPE than IPM in these studies. In addition to MSC/SC lipid extraction, OA and IPM can enhance the SC permeability through dissolving and removing cholesterol.

OA is able to facilitate the drug permeation more efficiently than IPM, which is shown by a less amount of OA treatment than IPM to achieve the same drug permeation rate (Jenner *et al.*, 1995) and the OA ability to carry the drug fully through SC more efficiently than IPM (Gabiga *et al.*, 2000). The difference in the drug permeation efficiency may be due to the slightly different phase behaviour and penetration mechanism between OA and IPM. The previous ^{2}H-NMR study of OA in MSC showed that OA participates in the liquid-crystalline phase transiently at the solid to liquid-crystalline phase transition, but maintains a full isotropic motion at temperatures below and above the phase transition (Rowat *et al.*, 2005). The motion of IPM, on the other hand, is partially restricted to the liquid-crystalline phase at temperatures above 37°C (Figure 36). The high and persistent isotropic motion allows OA to extract MSC/SC lipids and continuously carry the drug through the SC lipid bilayers, without having its motion being restricted constantly. This suggests that OA is able to facilitate the drug permeation more efficiently and thus a better CPE than IPM.

OA and IPM may also improve the SC permeability by dissolving cholesterol. This was demonstrated by an exponential increase in the isotropic phase component of cholesterol in MSC (Rowat *et al.*, 2005). This would create a more disordered MSC/SC lipid microstructure since cholesterol acts as a membrane stabilizer, and thus lead to enhanced drug permeation.

OA and IPM can change the phase composition of SC structure by dramatically removing ceramides, as supported by the linear relationship between the drug flux and removal of ceramides from SC membranes in the presence of OA or IPM (Ogiso *et al.*, 1995). The removal of ceramides would create dilations between adherent cornified cells,

which would enhance the penetration through the intercellular pathways. This is consistent with our ^{2}H-NMR data where IPM was shown to actively extract Cer16 (Figure 32 and Figure 34; no ^{2}H-NMR data provided for OA).

Comparing to OA, IPM is less efficient in drug permeation. Besides the MSC/SC lipid extraction, OA and IPM may improve the SC permeability through an additional mechanism: solvation and removal of cholesterol.

6.3 Summary: IPM in overall skin permeation and transdermal drug delivery studies

As mentioned before, various studies have utilized IPM in combination with other CPEs to achieve better drug permeation through synergistic effects. IPM has also been demonstrated to have capability of being used as a vehicle for drug delivery in addition to its CPE function. Many new technologies use IPM as a component to study TDD such as therapeutic ultrasound, microemulsion and cosmetic vehicles. Through these studies, a number of molecular interaction mechanisms between IPM and SC lipids have been proposed, which would help us understand IPM as a CPE more in depth. These molecular interaction mechanisms are also found to correlate to the behaviour of IPM in MSC.

The disruptive behaviour of IPM enables it to be an effective CPE in TDD and improve the overall skin permeability. Its ability to perturb the structural and phase compositional order in the lipophilic regions of SC allows the incorporation of additional hydrophilic CPE/CPEs (binary or ternary CPE systems) to disrupt the hydrophilic region of SC. The combinatory effect of a hydrophilic CPE and IPM can disrupt the order of both hydrophilic and lipophilic regions of SC lipid bilayers. In addition, the lipophilic

property of IPM allows it to act as a vehicle for lipophilic drug delivery, or create intercellular passages for hydrophilic drug delivery.

The ability of IPM to disrupt the lipophilic region of the lipid bilayers is not dependent upon the choice of permeant or complementary CPE. This allows IPM to be a very useful CPE in transdermal permeation studies, since its functions and behaviour do not change whether the study is conducted *in vivo*, *in vitro*, *ex vivo* or in model systems. When using binary or ternary CPE systems in TDD studies, additional effects observed other than those of IPM would be due to effects from other CPEs. Thus, IPM can be used as a fundamental CPE for TDD studies.

Lastly, the structural similarity of IPM to fatty acids may make it less harmful and a more ideal CPE. Azone, EtOH, IPA and many other hydrophilic CPEs are more volatile and thus exert greater effects on the skin permeability. However, the high volatility may cause unwanted skin irritation and to a further extent, fully and undesirably compromise the skin barrier function. Since they are not naturally existent in SC, they are not likely biodegradable and would delay skin recovery after application. Although IPM does not have dramatic perturbing effect, it does not cause severe fluidization of SC leading to damages to the skin.

6.4 Proposed physical/molecular models

The results from the ^{2}H-NMR and various studies have provided a good picture of the molecular mechanisms involved in IPM-facilitated transdermal drug delivery. This section will start with a summary of each model and then attempt combining all the models proposed earlier into a generic model of IPM in a single-CPE system in MSC.

A comparison of the chemical structures of Cer16, PA and IPM (Section 6.1.3) can help us formulate the molecular association model. IPM is more structurally similar to PA so it may associate with PA more by integrating into PA domains, dissolving and extracting PA. The smaller size of PA than Cer16 allows PA with faster motion and greater isotropic effect. These two observations suggested more effect of IPM on PA than Cer16.

The concentration dependence model mentioned earlier (Section 6.1.4) states that at low concentrations, fewer IPM molecules may be only enough to cause the integration effect and minor-extraction effect on MSC/SC lipid bilayer, leading to increased fluidity of MSC/SC. At high concentrations, sufficient IPM molecules could dissolve and extract MSC/SC lipids in addition to integration, and cause an even greater perturbation of the phase composition and order of MSC/SC.

Previous studies have proposed the hydrophilicity/lipophilicity model. The model suggests that the lipophilic property of IPM allows it to interact with the lipophilic region of SC lipids (Jiang *et al.*, 1995); whereas, the hydrophilic property of a hydrophilic CPE allows it to interact with the hydrophilic region of SC lipids. In the absence of a lipophilic CPE such as IPM, a hydrophilic CPE is found to be incapable of carrying the drug through the lipophilic regions of SC (Baker and Hadgraft, 1995).

The structural model can be described in three aspects: micellar formation, intermolecular/intercellular space expansion, and molecular domain separation. The fast isotropic motion of IPM indicates that IPM may form the highly mobile micellar structure (Bouwstra *et al.*, 2003). These micelles may consist of IPM, IPM/extracted MSC lipids or IPM/extracted SC lipids, tumbling outside or embedded in MSC/SC lipids

to create openings/leakage through the bilayers (Mills *et al.*, 2005). Extraction of MSC/SC lipids results in intermolecular space expansion and may lead to intercellular space expansion between corneocytes as the further effect. Lastly, molecular domain separations have been observed by FTIR and confocal Raman microscopy study of lipid behaviours in MSC (Moore *et al.*, 1997; Arseneault *et al.*, 2005), which provides insights into the preferential partitioning of IPM into PA domain. Note that these speculations include the partial PA/Cer16 domain separations, the higher association of IPM with PA and its preference to reside in the lipophilic regions of MSC.

Summing up these models, a generic model of IPM in MSC can be constructed. Figure 40 shows the speculation of IPM in MSC at high concentrations and low temperatures, since we are interested mostly in the effect of higher concentrations of IPM at the physiological temperature, where the IPM integration, extraction, and micellar formation come in combinatory effect to increase the fluidity, lesions, and even passages through MSC/SC membrane bilayers.

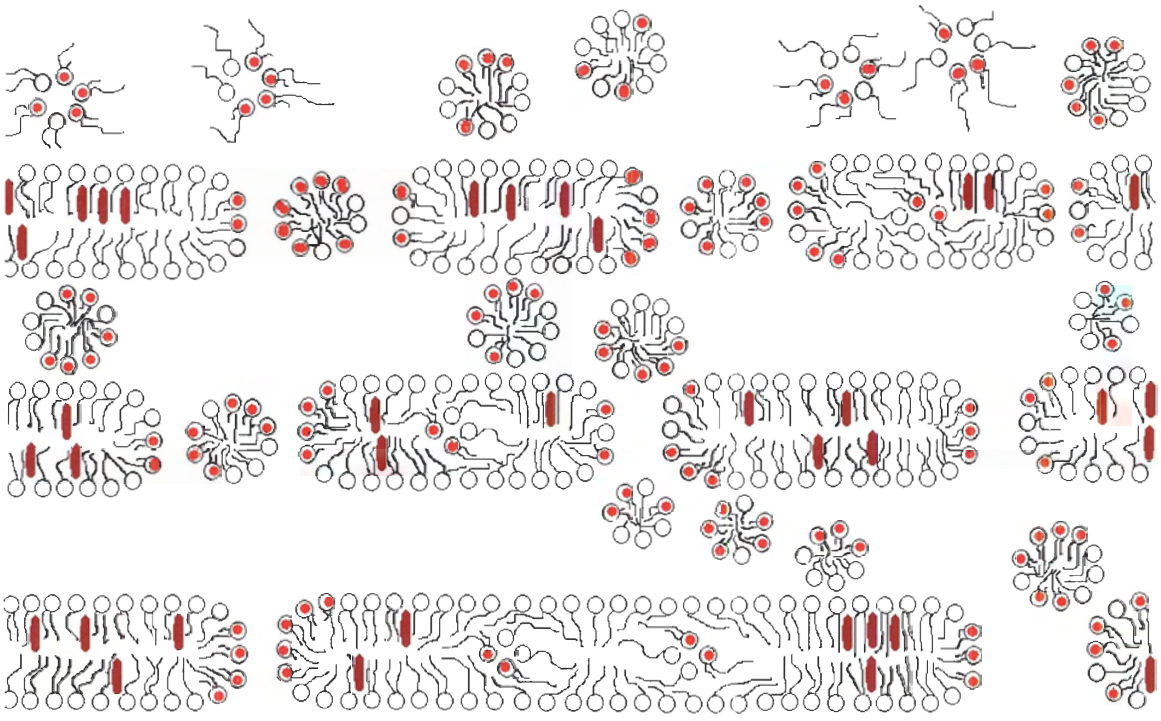

Figure 40: The proposed IPM model.

This computer-drawn diagram depicts the IPM extraction model, semi-micellar and micellar formation models proposed in our ^{2}H-NMR study of IPM in MSC. Each unit consisting of a circle and either one or two lines represents a lipid (Cer16, PA or IPM). The circles represent the polar headgroups of the lipids, and the lines represent the acyl chains (or amide-linked chains in Cer16). The brown capsule represents cholesterol. The lipid with headgroup coloured in red represents IPM. The lipid with one acyl chain represents PA, while all others represent Cer16. Note that there could be inverted micelles as well, which is indistinguishable in ^{2}H-NMR spectra since both micelles and inverted micelles would show isotropic phase signal. Micelles may form either outside or between the lipid bilayers. Inverted micelles may form either outside or within the lipid bilayers.

CHAPTER 7: CONCLUSION

Our ^{2}H-NMR study of IPM in MSC has provided data that are consistent with the results from previous *in vitro* and *ex vivo* studies to show that IPM has a significant influence on the phase behaviour and composition of MSC, and it effectively disrupts the structural order of MSC through intercalation into or extraction of lipid components from membrane bilayers. Our study provides an explanation at the molecular level regarding how Ceramide and Palmitic Acid are differently affected and how increased IPM leads to increased disruptive effect. This study in the model system also suggests that by changing the phase behaviour, composition and transition, IPM is able to reduce the integrity of MSC lipid microstructure (an indication of possible compromised barrier function and enhanced permeability of SC).

We applied a new procedure developed by Dr. E. E. Brief for analyzing the percentage of the solid phase component in MSC containing Cer16-d_{31}. This method accounts for the solid phase component found in short-reptime spectral data.

Brinkmann *et al.* (2003) suggested that IPM disrupts the lipid arrangement in corneocytes, and it inserts into intercellular lipids and causes a denser lipid packing which reduces permeation of drug; whereas, Isopropyl Alcohol (IPA) and IPM together alter the ordered structure of intercellular lipids of SC which results in faster transdermal drug permeation. By contrast, we have shown that IPM alone is able to disorder lipid

membrane packing in MSC. We suggest that IPM disrupts intercellular lipid structure of SC as well, which is not consistent the interpretation given by Brinkmann *et al.* (2003).

To better understand the model SC system, we plan to measure deuterated cholesterol. Rowat *et al.* (2005) has examined the phase behaviour of Chol-d_6 and has shown that in MSC containing OA, Chol-d_6 undergoes isotropic motion, and the Chol-d_6 isotropic phase component increases steadily, while both solid and liquid-crystalline phases of Chol-d_6 are reduced with increasing temperature (Rowat *et al.*, 2005). We would expect similar results with deuterated cholesterol in MSC containing IPM.

BIBLIOGRAPHY

Works Cited

Abraham, W. and Downing, D. T. 1991. Deuterium NMR investigation of polymorphism in stratum corneum lipids. *Biochim. Biophys. Acta.* 1068 (2): 189-194.

Abraham, W., Kitson, N., Bloom, M. and Thewalt, J. L. 1997. "*Investigation of Membrane Structure and Dynamics by Deuterium NMR: Application to the Stratum Corneum.*" In Mechanism of Transdermal Drug Delivery, Edited by Russell O. Potts and Richard H. Guy, 163-198. New York: Marcel Dekker, NY, USA.

Alberti, I., Kalia, Y. N., Naik, A., Bonny, J. D. and Guy, R. H. 2001. In vivo assessment of enhanced topical delivery of terbinafine to human stratum corneum. *Control Release.* 71 (3): 319-327.

Alberti, I., Kalia, Y. N., Naik, A., Bonny, J-D. and Buy, R. H. 2001. Effect of ethanol and isopropyl myristate on the availability of topical terbinafine in human stratum corneum. *Int. J. Pharm.* 219: 11-19.

Al-Saidan, S. M., Krishnaiah, Y. S., Chandrasekhar, D. V., Lalla, J. K., Rama, B., Jayaram, B. and Bhaskar, P. 2004. Formulation of an HPMC gel drug reservoir system with ethanol-water as a solvent system and limonene as a penetration enhancer for enhancing in vitro transdermal delivery of nicorandil. *Skin Pharmacol. Physiol.* 17 (6): 310-320.

Arseneault, M, Kwak, S. and Lafleur, M. 2005. Organization and domain formation in stratum corneum lipids: a FT-IR and confocal Raman microspectroscopy investigation. *Lipids, Liposomes & Biomembranes 2005.* The University of British Columbia. Vancouver, B.C. Canada.

Baker, E. J. and Hadgraft, J. 1995. In vitro percutaneous absorption of arildone, a highly lipophilic drug, and the apparent no-effect of the penetration enhancer Azone in excised human skin. *Pharm Res.* 12 (7): 993-997.

Benson, H. A. E. 2005. Transdermal Drug Delivery: Penetration Enhancement Techniques. *Current Drug Delivery.* 2 (1): 23-33(11).

Blank I. H. 1965. Cutaneous barriers. *J. Invest. Dermatol.* 45: 249-256.

Bouwstra, J. A. 1997. The skin barrier, a well-organized membrane. *Colloids Surf.* A. 123-124: 403-413.

Bouwstra, J. A., Gooris, G. S., Salomons-de Vries, M. A., van der Spek, J. A. and Bras, W. 1992. Structure of human stratum corneum as a function of temperature and hydration: A wide-angle X-ray diffraction study. *Int. J. Pharm.* 84 (3): 205-216.

Bouwstra, J. A., Gooris, G. S., Cheng, K., Weerheim, A., Bras, W. and Ponec, M. 1996. Phase behaviour of isolated skin lipids. *J. Lipid Res.* 37(5): 999-1011.

Bouwstra, J. A., Thewalt, J., Gooris, G. S. and Kitson, N. 1997. A Model Membrane Approach to the Epidermal Permeability Barrier: An X-ray Diffraction Study. *Biochemistry.* 36: 7717-7725.

Bouwstra, J., Honeywell-Nguyen, P.L., Gooris, G.S. and Ponec, M. 2003. Structure of the skin barrier and its modulation by vesicular formulations. *Prog. Lipid Res.* 42: 1-36.

Brief, E. E. NMR Probe Picture Collection. Department of Physics. Simon Fraser University. Burnaby, B.C. Canada. 2004.

Brinkmann, I. and Müller-Goymann. 2003. Role of Isopropyl Myristate, Isopropyl Alcohol and a Combination of Both in Hydrocortisone Permeation across the Human Stratum corneum. *Skin Pharmacol. Appl. Skin Physiol.* 16: 393-404.

Chakrabarti, A. and Sharma, M. M. Anhydrous Esterification of Myristic Acid with Propylene: Ion Exchange Resin and Acid-Treated Clay as Catalysts. *JAOCS.* 12, 1251-1253. 1992.

Davis, J. H., Jeffrey, K. R., Bloom, M., Valic, M. I. and Higgs, T. P. 1976. Quadrupolar echo deuterium magnetic resonance spectroscopy in ordered hydrocarbon chains. *Chem. Phys. Lett.* 42: 390-394.

Dharap, S. S., Wang, Y., Chandna, P., Khandare, J. J., Qiu, B., Gunaseelan, S., Sinko, P. J., Stein, S., Farmanfarmaian, A. and Minko, T. 2005. Tumor-specific targeting of an anticancer drug delivery system by LHRH peptide. *Proc. Natl. Acad. Sci. USA.* 102 (36): 12962-12967.

Elias, P. M. 1983. Epidermal lipids, barrier function, and desquamation. *J. Invest. Dermatol.* 80: 44s-49s.

Elias, P. M. and Friend, D. S. 1975. The permeability barrier in mammalian epidermis. *J. Cell. Biol.* 65: 180-191.

Fang, L., Kobayashi, Y., Numajiri, S., Kobayashi, D., Sugibayashi, K., Morimoto, Y. 2002. The Enhancing Effect of a Triethanolamine-Ethanol-Isopropyl Myristate Mixed System on the Skin Permeation of Acidic Drugs. *Biol. Pharm. Bull.* 25 (10): 1339-1344.

Fang, L., Numajiri, S., Kobayashi, D. and Morimoto, Y. 2003. The use of complexation with alkanolamines to facilitate skin permeation of mefenamic acid. *Int J. Pharm.* 262: 13-22.

Farrar, T. C. and Becker, E. D. 1971. Pulse and Fourier Transform NMR. Introduction to Theory and Methods. New York: Academic Press, Inc., NY, USA.

Fenske, D. B., Thewalt, J. L., Bloom, M. and Kitson N. 1994. Models of stratum corneum intercellular membranes: ^{2}H NMR of macroscopically oriented multilayers. *Biophys. J.* 67: 1562-1573.

Finnin, B.C. and Morgan, T.M. 1999. Transdermal Penetration Enhancers: Applications, Limitations, and Potential. *J. Pharm. Sci.* 88 (10): 955-958.

Forslind B. 1994. A domain mosaic model of the skin barrier. *Acta Derm. Venereol.* 74 (1): 1-6.

Fukushima, E. and Roeder, S. B. W. 1994. Experimental Pulse NMR. A Nuts and Bolts Approach. Massachusetts: Addison-Wesley Publishing Company, Massachusetts, USA.

Gabiga, H., Cal, K. and Janicki, S. 2000. Effect of penetration enhancers on isosorbide dinitrate penetration through rat skin from a transdermal therapeutic system. *Int J Pharm.* 199 (1): 1-6.

Ghanem, A. H., Mahmoud, H., Higuchi, W. I., Liu, P. and Good, W. R. 1992. The effects of ethanol on the transport of lipophilic and polar permeants across hairless mouse skin: Methods/validation of a novel approach. *Int. J. Pharm.* 78: 137-156.

Golden, G. M., Guzek, D. B., Harris, R. R., McKie, J. E. and Potts, R. O. 1986. Lipid thermotropic transitions in human stratum corneum. *J. Invest. Dermatol.* 86 (3): 255-259.

Golden, G. M., Guzek, D. B., Kennedy, A. E., McKie, J. E. and Potts, R. O., 1987. Stratum corneum lipid phase transitions and water barrier properties. *Biochemistry.* 26(8), 2382-2388.

Gwak, H. S., Kim, S. U. and Chun, I. K. 2002. Effect of vehicles and enhancers on the in vitro permeation of melatonin through hairless mouse skin. *Arch Pharm Res.* 25 (3): 392-396.

Hadgraft, J., Walters, K. A. and Wotton, P. K. 1985. Facilitated transport of sodium salicylate across an artificial lipid membrane by Azone. *J. Pharm. Pharmacol.* 37 (10): 725-727.

Harada, S., Nakada, Y., Yamashita, F. and Hashida, M. 2005. Biopharmaceutical considerations on antihistamine effects of topically adiministered emedastine. *J. Pharm. Sci.* 94 (1): 17-24.

Hirvonen, J. Rajala, R., Vihervaara, P., Laine, E., Paronen, P. and Urtti, A. 1995. Mechanism and reversibility of penetration enhancer action in the skin – a DSC study. *Eur. J. Pharm. Biopharm.* 40: 81-85.

Ito, Y., Ogiso, T. and Iwaki, M. 1988. Thermodynamic study on enhancement of percutaneous penetration of drugs by Azone. *J. Pharmacobiodyn.* 11 (11): 749-757.

Jenner, J., Saleem, A. and Swanston, D. 1995. Transdermal delivery of physostigmine. A pretreatment against organophosphate poisoning. *J Pharm Pharmacol.* 47 (3): 206-212.

Jiang, R., Benson, H. A., Cross, S. E. and Roberts, M. S. 1998. In vitro human epidermal and polyethylene membrane penetration and retention of the sunscreen benzophenone-3 from a range of solvents. *Pharm Res.* 15 (12): 1863-1868.

Jin, Y., Seki, T., Morimoto, Y. and Juni, K. 2000. Effect of application volume of ethanol-isopropyl myristate mixed solvent system on permeation of zidovudine and probenecid through rat skin. *Drug Dev. Ind. Pharm.* 26 (2): 193-198.

Kanikkannan, N., Kandimalla, K., Lamba, S. S., Singh, M. 2000. Structure-activity Relationship of Chemical Penetration Enhancers in Transdermal Drug Delivery. *Curr. Med. Chem.* 7 (6): 593-608(16).

Kitson, N., Thewalt, J., Lafleur, M. and Blooms, M. 1994. A Model Membrane Approach to the Epidermal Permeability Barrier. *Biochemistry.* 33: 6707-6715.

Knutson, K., Potts, R. O., Guzek, D. B., Golden, G. M. Mckie, J. E. Lambert, W. J. and Higuchi, W. I. 1985. Macro- and molecular physical-chemical considerations in understanding drug transport in the stratum corneum. *J. Controlled Release.* 2: 67-87.

Lafleur, M. 1998. Phase behaviour of model stratum corneum lipid mixtures: an infrared spectroscopic investigation. *Can. J. Chem.* 76: 1501-1511.

Lampe, M. A., Burlingame, A. L. Whitney, J., Williams, M. L., Brown, B. E., Roitman, E. and Elias, P. M. 1983. Human stratum corneum lipids: characterization and regional variations. *J. Lipid Res.* 24: 120-130.

Leopold, C. S. and Lippold, B. C. 1995. An attempt to clarify the mechanism of the penetration enhancing effects of lipophilic vehicles with differential scanning calorimetry (DSC). *J. Pharm. Pharmacol.* 47 (4): 276-281.

Mills, J. K. and Needham, D. 2005. Lysolipid incorporation in dipalmitoylphosphatidylcholine bilayer membranes enhances the ion permeability and drug release rates at the membrane phase transition. *Biochim Biophys Acta.* 1716 (2): 77-96.

Moore, D. J., Rerek, M. E. and Mendelsohn, R. 1997. Lipid domains and orthorhombic phases in model stratum corneum: evidence from Fourier transform infrared spectroscopy studies. *Biochem. Biophys. Res. Commun.* 231 (3): 797-801.

Morimoto, Y., Hayashi, T., Kawabata, S., Seki, T. and Sugibayashi, K. 2000. Effect of1 menthol-ethanol-water system on the systemic absorption of flurbiprofen after repeated topical applications in rabbits. *Biol. Pharm. Bull.* 23 (10): 1254-1257.

Nelson, D. L. and Cox, M. M. 2000. Lehninger Principles of Biochemistry. 3rd Edition. New York: Worth Publishers, NY, USA.

Norlén, L., Nicander, I., Lundsjö, A., Cronholm, T. and Forslind, B. 1998. A new HPLC-based method for the quantitative analysis of inner stratum corneum lipids with special reference to the free fatty acid fraction. *Arch. Dermatol. Res.* 290: 508-516.

Ogiso, T., Iwaki, M., Bechako, K. and Tsutsumi, Y. 1992. Enhancement of percutaneous absorption by laurocapram. *J. Pharm. Sci.* 81 (8): 762-767.

Ogiso, T., Paku, T., Iwaki, M. and Tanino, T. 1995. Percutaneous penetration of fluorescein isothiocyanate-dextrans and the mechanism for enhancement effect of enhancers on the intercellular penetration. *Biol Pharm Bulll.* 18 (11): 1566-1571.

Okamoto, K-I., Yamamoto, M., Otoshi, Y., Semoto, T., Yano, M. and Tanakaan, K. Pervaporation-aided Esterification of Oleic Acid. *J. Chem. Eng. Jpn.* 26(5), 475-481. 1993.

Ongpipattanakul, B., Francoeur, M. L. and Potts, R. O. 1994. Polymorphism in stratum corneum lipids. *Biochim. Biophys. Acta.* 1190 (1): 115-122.

Pardo A, Shiri Y, Cohen S Percutaneous absorption of physostigmine: optimization of delivery from a binary solvent by thermodynamic control. *J Pharm Sci.* 1990 Jul;79(7):573-8

Pascher, I. 1976. Molecular arrangements in sphingolipids. Conformation and hydrogen bonding of ceramide and their implication on membrane stability and permeability. *Biochim Biophys Acta.* 455 (2): 433-51.

Pavia, D. L., Lampman, G. M. and Kriz, G. S. Introduction to Organic Laboratory Techniques. A Microscale Approach. 3rd Edition. Saunders College Publishing, Philadelphia, PA, USA. 1999.

Pillai, O., Nair, V. and Panchagnula, R. 2004. Transdermal iontophoresis of insulin: IV. Influence of chemical enhancers. *Int. J. Pharm.* 269(1): 109-120.

Potts, R. O. and Francoeur, M. L. 1990. Lipid biophysics of water loss through the skin. *Proc. Natl. Acad. Sci. USA.* 87 (10): 3871-3873.

Priborsky, J., Takayama, K., Nagai, T., Waitzova, D. and Elis, J. 1987. Combination effect of penetration enhancers and propylene glycol on in vitro transdermal absorption of insulin. *Drug Des. Deliv.* 2 (2): 91-97.

Rowat, A. C. 1996. Deuterium NMR Spectrometer Manual. Chapter 2. Section 11. Magnet. Department of Physics. Simon Fraser University. Burnaby, B.C. Canada.

Schurer, N. Y. and Elias P. M. 1991. The biochemistry and function of stratum corneum lipids. *Adv Lipid Res.* 24: 27-56.

Seeley, R. R., Stephens, T. D. and Tate, P. 2005. Essentials of Anatomy & Physiology, 74-109. 5th Edition. New York: McGraw-Hill Companies, Inc., NY, USA.

Singh, B. N., Singh, R. B. and Singh, J. 2005. Effects of ionization and penetration enhancers on the transdermal delivery of 5-fluorouracil through excised human stratum corneum. *Int. J. Pharm.* 298: 98–107.

Smith, E. W. ad Maibach, H. I. 1995. "Percutaneous Penetration Enhancers," 125-126. Boca Raton: CRC Press Inc., Florida, USA.

Song, Y., Xiao, C., Mendelsohn, R., Zheng, T., Strekowski, L. and Michniak, B. 2005. Investigation of Iminosulfuranes as Novel Transdermal Penetration Enhancers: Enhancement Activity and Cytotoxicity. *Pharm Res.* Epub ahead of print.

Stoughton, R. B. and Fritsch, W. 1964. Influence of dimethyl sulfoxide on human percutaneous absorption. *Arch. Dermatol.* 90: 512-517.

Sugibayashi, K., Nakayama, S., Seki, T., Hosoya, K. and Morimoto, Y. 1992. Mechanism of skin penetration-enhancing effect by laurocapram. *J. Pharm. Sci.* 81: 58-64.

Sugibayashi, K., Sakanoue, C. and Morimoto, Y. 1989. Utility of topical formulations of morphine hydrochloride containing azone and N-methyl-2-pyrrolidone. *Sel Cancer Ther. 5* (3): 119-28.

Suh, H. and Jun, H. W. 1996. Effectiveness and mode of action of isopropyl myristate as a permeation enhancer for naproxen through shed snake skin. *J Pharm Pharmacol.* 48 (8): 812-816.

Suhonen, T. M., Bouwstra, J. A. and Urtti, A. 1999. Chemical enhancement of percutaneous absorption in relation to stratum corneum structural alterations. *J. Control Release* 59: 149-161.

Sweeney T. M. and Downing, D. T. 1970. The Role of Lipids in the Epidermal Barrier to Water Diffusion. *J. Invest. Dermatol.* 55 (2): 135-140.

Thewalt, J., Kitson, N., Araujo, C., MacKay, A. and Bloom, M. 1992. Models of stratum corneum intercellular membranes: The sphingolipid headgroup is a determinant of

phase behaviour in mixed lipid dispersions. *Biochem. Biophys. Res. Commun.* 188 (3): 1247-1252.

Tortora, G. J. 1995. Principles of Human Anatomy, 88-98. 7th Edition. New York: HarperCollins College Publishers, NY, USA.

Van De Graff, K. M. 2002. Human Anatomy, 106-119. 6th Edition. New York: McGraw-Hill Companies, Inc., NY, USA.

Van Duzee, B. F. 1975. Thermal analysis of human stratum corneum. *J. Invest. Dermatol.* 65: 404-408.

Wertz, P. W. 2000. Lipids and barrier function of the skin. *Acta Derm. Venereol Suppl. (Stockh).* 208: 7-11.

Wertz, P. W. and Downing, D. T. 1989. *Drugs Pharm. Sci.* 35: 1.

Wertz, P. W., Swartzendruber, D. C., Abraham, W., Madison, K. C. and Downing, D. T. 1987. Essential fatty acids and epidermal integrity. *Arch Dermatol.* 123 (10): 1381-1384.

White, S. H., Mirejovsky, D. and King, G. I. 1988. Structure of Lamellar Lipid Domains and Corneocyte Envelopes of MurineStratum Corneum. An X-ray Diffraction Studyt. *Biochemistry.* 27: 3725-3732.

Wiechers, J. W. and de Zeeuw, R. A. 1990. Transdermal drug delivery: efficacy and potential applications of the penetration enhancer Azone. *Drug Des Deliv.* 6 (2): 87-100.

Wiechers, J. W., Drenth, B. F., Jonkman, J. H. and de Zeeuw, R. A. 1987. Percutaneous absorption and elimination of the penetration enhancer Azone in humans. *Pharm. Res.* 4 (6): 519-523.

Yardley, H. J. and Summerly, R. 1981. Lipid composition and metabolism in normal and diseased epidermis. *Pharmacol. Ther.* 13 (2): 357-383.

Website References

Clausen, K., 1993-2004. "The Aikido FAQ," Clausen, K. http://aikidofaq.com/bilder/anatomy/Skin.jpg.html

Department of Chemistry & Biochemistry, "CU Boulder Organic Chemistry Undergraduate Courses Lab Techniques - Thin Layer Chromatography - TLC," University of Colorado, Colorado, USA. http://orgchem.colorado.edu/hndbksupport/TLC/TLC.html

Department of Chemistry & Biochemistry, "Thin Layer Chromatography," Worcester Polytechnic Institute, MA, USA. http://www.wpi.edu/Academics/Depts/Chemistry/Courses/General/tlc.html. 2004

Electrical Engineering Training Series, "Table 2-1. Radio Frequency Bands," Integrated Publishing, http://www.tpub.com/content/neets/14182/css/14182_67.htm

Gray, J. 1997. "The World of Skin Care – Preventing infection," P&G Beauty Science. http://www.pg.com/science/skincare/Skin_tws_40.htm

Reusch, W. 2004. "Nuclear Magnetic Resonance Spectroscopy," Department of Chemistry, Michigan State University. http://www.cem.msu.edu/~reusch/VirtualText/Spectrpy/nmr/nmr1.htm.

Reusch, W. 2004. "Nuclear Magnetic Resonance Spectroscopy," Department of Chemistry, Michigan State University. http://www.cem.msu.edu/~reusch/VirtualText/Spectrpy/nmr/nmr2.htm.

Saito, T., Hayamizu, K., Yanagisawa, M., Yamamoto, O., Wasada, N., Someno, K., Kinugasa, S., Tanabe, K., Tamura, T., Tanabe, K. and Hiraishi, J. 2005. "Spectral Database for Organic Compounds SDBS," National Institute of Advanced Industrial Science and Technology (AIST), Japan. http://www.aist.go.jp/RIODB/SDBS/menu-e.html.

Sigma-Aldrich Co., "Sigma-Aldrich," Sigma-Aldrich Co. St. Louis, MO, USA. http://www.sigmaaldrich.com.

APPENDICES

Appendix A: Computer program procedures and scripts (developed and written previously by Dr. Y. W. Hsueh, X. Chen and Dr. E. E. Brief, Thewalt Laboratory, Department of Physics, Simon Fraser University)

Appendix A-1: "Origin 7.0" graphing analysis program

"Origin 7.0" graphing analysis program was received from courtesy of Philipus J. Patty, Department of Physics, Simon Fraser University. This program is licensed to Thewalt Laboratory, Department of Molecular Biology and Biochemistry, Simon Fraser University.

The following are the "Origin 7.0" analysis procedures for fitting the isotropic phase signal in the FID, using the Gaussian equation. The Gaussian function is as follows:

$$y = y_o + Ae^{-\frac{(x-x_c)^2}{2w^2}}$$

By obtaining the value of the echo signal (Echo Height, EH) and the value of the Gaussian fit of the isotropic phase signal at EH, the percentage of the isotropic phase can be calculated. The isotropic phase signal is removed only for the calculation of the percentage of the solid phase component in MSC containing Cer16-d_{31}.

The signal artifacts as a result of the isotropic truncation effect in ^{2}H-NMR spectra acquired from MSC containing IPM-d_{27} can be removed using the apodization procedure, using the exponential decay function:

$$y = e^{-x}$$

The followings are the procedures for analyzing the FID obtained from MSC containing PA-d_{31}, Cer16-d_{31} or IPM-d_{27} using "Origin 7.0" graphing analysis program.

Procedure 1: The "Origin 7.0" graphing analysis program analysis procedure for the non-linear Gaussian fitting. Step 7 ~ 9 is performed only for calculating the percentage of the solid phase component in MSC containing Cer16-d_{31}.

Step	Procedure
1	Import data file as an ASCII file
2	Plot the FID using the NMR tool function
3	Perform auto zero phasing and baseline correction (use default value)
4	Perform non-linear fitting using the "Origin 7.0" basic Gaussian function Perform the Gaussian fitting of the FID between 50^{th} ~ 4096^{th} points Set appropriate values for parameters y_o, x_c, w, A Perform the non-linear fit with repeating 100 iterations or 100 Simplex-iterations until the χ^2 value is constant
5	Record the Echo Height value and the corresponding Gaussian fit value at the same data point
6	Calculate the percentage of the isotropic phase component
7	Subtract the value of the Gaussian fit from the value of FID and save the data as a new ASCII file
8	Set the baseline value (secondary y values) = 0
9	Export the data as a new ASCII file
10	Repeat the procedure for both long and short reptime data (τ_L and τ_S)

Procedure 2: The "Origin 7.0" graphing analysis program analysis procedure for the apodization of FID data obtained from MSC containing IPM-d_{27}.

Step	Procedure
1	Import data file as an ASCII file
2	Plot the FID using the NMR tool function
3	Perform auto zero phasing and baseline correction (use default value)
4	Set the appropriate value for the application of the exponential decay function to the FID
5	Repeat until the FID signal decays to zero as time $\rightarrow \infty$
6	Save the processed FID as a new data file

Appendix A-2: "Igor 4.0" spectral analysis program

"Igor 4.0" spectral analysis program was received from courtesy of Xin Chen, Department of Physics, the University of British Columbia. This program is licensed to Thewalt Laboratory, Department of Molecular Biology and Biochemistry, Simon Fraser University.

The followings are the "Igor 4.0" spectral analysis procedures for plotting/analyzing ^{2}H-NMR spectra, averaging the long reptime FID data (for better ^{2}H signal-noise ratio), and calculating the percentage of the solid phase component in MSC containing Cer16-d_{31}. Note that prior to plotting a ^{2}H-NMR spectrum, it is necessary to change the number of scans to the correct value corresponding to the selected data file.

Procedure 3: The "Igor 4.0" spectral analysis program analysis procedure for plotting ^{2}H-NMR spectra of FID data acquired from MSC containing PA-d_{31}, Cer16-d_{31} or IPM-d_{27}.

Step	Procedure
1	Perform the command "Macro" – "spectrum"
2	Select the data file to be plotted
3	The followings information would be displayed: the temperature, the ^{2}H-NMR spectrum, the FID, and the value of EH, M_0 and M_1

Procedure 4: The "Igor 4.0" spectral analysis program analysis procedure for averaging the long reptime FID data acquired from MSC containing PA-d_{31}, Cer16-d_{31} or IPM-d_{27}.

Step	Procedure
1	Perform the command "Macro" – "add_FID".
2	Select the long reptime FID data files to be added for averaging
3	Check and confirm the consistency of FID data signals
4	Perform the command "Macro" – "Save_CombinedFID" to average the FID data
5	Save the averaged FID data as a new data file

Procedure 5: The "Igor 4.0" spectral analysis program analysis procedure for plotting and examining the apodized ^{2}H-NMR spectra of FID data acquired from MSC containing IPM-d_{27}.

Step	Procedure
1	Perform the command "Macro" – "spectrum"
2	Select the data file to be plotted
3	The followings information would be displayed: the temperature, the ^{2}H-NMR spectrum, the FID, and the value of EH, M_0 and M_1
4	Observe the spectrum to see if artifacts from the isotropic truncation effect still exist. Repeat the apodization procedure in "Origin 7.0" graphing analysis program if the spectrum still has the artifact.

Procedure 6: The "Igor 4.0" spectral analysis program analysis procedure for calculating the percentage of the solid phase component in MSC containing Cer16-d_{31}.

Step	Procedure
1	Perform the command "Macro" – "prestep"
2	Perform the command "Macro" – "all_in_one"
3	Select the corresponding short and long reptime FID data files (with the isotropic phase signal removed as described in Procedure 1, Step 7 ~ 10)
4	The followings information would be displayed: the temperature, the name of selected short and long reptime files, the value of the constant "*c*" (Refer to Equation 13 and Equation 14), M_0, M_1 and the percentage of the solid phase component in MSC containing Cer16-d_{31}
5	Record the values

Program Script 1: The "Igor 4.0" spectral analysis program script for the program *Macro spectrum* (Plotting ^{2}H-NMR spectrum).

```
Macro spectrum()
//Rdbc()
//Save/G/M="\r\n"/W rvec,ivec as "bc.dat"
variable icb=0
load()
// making table with filename (GetDataFolder(1)), peakheight (dataV_peakheight)
// M0 (moments[0]) and M1 (moments[1])
make /N=5 /T cbfile
make /N=5 cbeh, cbm0, cbm1
String label = GetDataFolder(1)
        label = label[strsearch(label,":",0)+1,strlen(label)-2] // strip 'root:' and final ':'
cbfile[icb]=label
cbeh[icb]=dataV_peakheight
cbm0[icb]=moments[0]
cbm1[icb]=moments[1]
DoWindow /K Table0
Edit /W=(20,300,600,300) cbfile, cbeh, cbm0, cbm1 as "SpectrumOutput"
//Edit /W=(20,300,600,300) cbfile, cbeh, cbm1 as "SpectrumOutput"
End
```

Program Script 2: The "Igor 4.0" spectral analysis program script for the program *Macro Read* (Plotting ^{2}H-NMR spectrum)

```
Macro Read()
//      paths("d:dppc-d_erg:dp725:","d:dppc-d_erg:dp725:")
        val2("",2)
        r2(0)
        vd()
        zo(5)
Cursor/p A,rvec,14

End
```

Program Script 3: The "Igor 4.0" spectral analysis program script for the program *Macro Read_little* (Plotting ^{2}H-NMR spectrum)

```
Macro Read_little()
        paths("d:Elana:SKIN:Ceramide:IPM:temp_run:","d:Elana:SKIN:Ceramide:IPM:te
mp_run:")
        val2("",2)
        r2(0)
End
```

Program Script 4: The "Igor 4.0" spectral analysis program script for the program *Macro Rdbc* (Baseline correction).

```
Macro Rdbc()
//      paths("d:dppc-d_erg:dp725:","d:dppc-d_erg:dp725:")
        val2("",2)
        r2(0)
        vd()
        zo(5)
//      print sum(rvec,pnt2x(rvec,7680),pnt2x(rvec,8191))/512
//      print sum(ivec,pnt2x(rvec,7680),pnt2x(ivec,8191))/512
//      print sum(rvec,pnt2x(rvec,3840),pnt2x(rvec,4095))/256
//      print sum(ivec,pnt2x(rvec,3840),pnt2x(ivec,4095))/256
        vbc(3840,4095)
//      vbc(3000,4000)
Cursor/p A,rvec,14

End
```

Program Script 5: The "Igor 4.0" spectral analysis program script for the program *Macro PhFt* (Plotting ^{2}H-NMR spectrum).

```
Macro PhFt()
//        variable tt
          vcaspline()
          vcph()
          vcls()
//        Redimension/N=4096 rvec,ivec
//        Redimension/N=(4096,1) rmat,imat
          w()
          mvft()
      vbc(250,234.5)
      vd()
      vmoma(1,50);vmomd(1,50)
          vax_vmoma(1,50);variable m1=momn;vax_vmomd(1,50)
          vax_vmoma(2,50);variable m2=momn;vax_vmomd(2,50)
//        tt=m2/m1/m1
//        print "tt=";print tt
     CalcMoments(150e3) // elana change
//      CalcMoments(75e3)
End
```

Program Script 6: The "Igor 4.0" spectral analysis program script for the program *Function Load* (Loading FID data).

```
Function Load()

     SetDataFolder root:  //set current folder to root

        String df,savedf,spec_fullname

        df = LoadNewFID("","")
        if (strlen(df) ==0)
                print "aborted"
                return 1
        endif
        print "working in "+df
        savedf = GetDataFolder(1)
        SetDataFolder $df
        DisplayFID()
        ConvertFIDtoSpectrum()
        DisplaySpec()
        CalcMoments(150e3) // elana changes moments
//      CalcMoments(75e3)
//      do_depake(rspec)

//   added by Xin on May 20, 2003, copied each spectrum to folder Spectra
        SetDataFolder $savedf
        newDataFolder/O/S Spectra
        spec_fullname=savedf + "'" + df + "'" +":rspec"
        duplicate $spec_fullname $df
        setDataFolder root:
        setDataFolder $df
End
```

Program Script 7: The "Igor 4.0" spectral analysis program script for the program *Function CalcMoments* (Calculating M_1).

```
Function CalcMoments(width)
        Variable        width;

        Variable        x1,x2;
        Variable        M,Mr,Mi;
        Variable        M0,M1;
        String          foo

        x1 = -width
        x2 = width

        print "Calculating moments between (",x1,",",x2,")"
        // zero moment
        Mi = CalcPartialMoment(rspec,0,-width,0)
        Mr = CalcPartialMoment(rspec,0,0,+width)
        M = 0.5*(Mi+Mr)
        print "M0 = ",M," (",Mi,",",Mr,")"
        M0 = M

        // first moment
        //Mi = CalcPartialMoment(rspec,1,-width,-1200) //elana changes the limits
        //Mr = CalcPartialMoment(rspec,1,1200,+width) //elana changes the limits
        Mi = CalcPartialMoment(rspec,1,-width,0)
        Mr = CalcPartialMoment(rspec,1,0,+width)
        M = 0.5*(Mi+Mr)
        print "M1 = ",M," (",Mi,",",Mr,")"
        M1 = M

        sprintf foo "M\\B0\\M = %6.4f\rM\\B1\\M = %6.1f", M0, M1
        Textbox/C/N=moments/F=2/A=RC foo

        // Normalize spectrum  Elana Took this Out
        sprintf foo "rspec /= %g", M0
        Execute foo

        // save the results
        make/o/d/n=2 moments
        moments[0] = M0
        moments[1] = M1
End
```

Program Script 8: The "Igor 4.0" spectral analysis program script for the program *Macro fid_add5* (Averaging the long reptime FID data).

```
Macro fid_add5()

Read_little()  // load 1st set of data
display rvec
setaxis bottom 0,0.0001
rename rvec, rvec1
rename ivec, ivec1
Read_little()  // load 2nd set of data
display rvec
setaxis bottom 0,0.0001
rename rvec, rvec2
rename ivec, ivec2
Read_little()  // load 3rd set of data
display rvec
setaxis bottom 0,0.0001
rename rvec, rvec3
rename ivec, ivec3
Read_little()  // load 4th set of data
display rvec
setaxis bottom 0,0.0001
rename rvec, rvec4
rename ivec, ivec4
Read_little()   //load 5th set of data
display rvec
setaxis bottom 0,0.0001
duplicate rvec f0
duplicate rvec f1
rename rvec, rvec5
rename ivec, ivec5
f0=(rvec1+rvec2+rvec3+rvec4+rvec5)/5
f1=(ivec1+ivec2+ivec3+ivec4+ivec5)/5

End
```

Program Script 9: The "Igor 4.0" spectral analysis program script for the program *Macro Save_CombinedFID* (Saving the averaged long reptime FID data).

```
Macro Save_CombinedFID()
    Save/G/M="\r\n"/W f0,f1
    ExecuteCmdOnList("DoWindow/K %s", WinList("*",";","WIN:1") )
    killwaves /A
    paths()
End
```

Program Script 10: The "Igor 4.0" spectral analysis program script for the program *Macro pre-step* (Prestep prior to calculating the % solid in MSC containing Cer16-d_{31}).

```
Macro pre_step()
  newDataFolder/O/S Spectra
  setDataFolder root:Spectra
//  make /N=61 temp_C, eb_con, eb_md, eb_m0, eb_solid, eb_m1
  make /N=61 temp_C, eb_con, eb_ehs, eb_ehl, eb_solid, eb_m1, eb_md, eb_m0
  make /N=61 /T eb_name1, eb_name2
  setDataFolder root:
End
```

Program Script 11: The "Igor 4.0" spectral analysis program script for the program *Macro all_in_one* (Calculating the % solid in MSC containing Cer16-d_{31}).

```
Macro all_in_one(temperature,long_rt,short_rt)
  variable temperature
  variable long_rt
  variable short_rt
  String name1,name2
  print "choose short reptime"
  name1=spectrum_f()
  print "choose long reptime"
  name2=spectrum_f()
// The spectra must be processed with the correct number of scans
// Normalization must be turned off (search for "normalize")
setDataFolder root:Spectra
variable const_val = .4
variable solid
//variable ieb = 20
variable ieb = 0
eb_name1[ieb] = name1
eb_name2[ieb] = name2
//make /N=61 temp_C
//temp_C[temperature-ieb] = temperature
temp_C[ieb] = temperature
//rename 'L59.txt' long
//rename 'F59_300B.TXT' short
duplicate $name1 short
duplicate $name2 long
long=long/long_rt
short=short/short_rt
duplicate long difference
duplicate long const
const = const_val
difference = short - const*long
WaveStats/Q/R=[2600,3000] difference
display difference
do
    //print V_avg
    const_val = const_val - 0.001
    const = const_val
    difference = short - const*long
    WaveStats/Q/R=[2600,3000] difference
    //print const(0)
//while(abs(V_avg) > 0.000000001)
```

```
while(abs(V_avg) >  0.00000001)
print const(0)
//duplicate difference rspec
//CalcMoments(150e3)
//duplicate moments moments_diff
//KillWaves rspec
//duplicate short rspec
//CalcMoments(150e3)
//duplicate moments moments_short
//KillWaves rspec
//duplicate long rspec
//CalcMoments(150e3)
//KillWaves rspec
//solid = 100 * (1 - moments_diff[0]/((1-const[0])*moments[0]))
//solid = 100 * (31/(28 - 31*const[0]))*(1 - const[0] -((moments_diff[0])/moments[0]))
eb_ehs[0] = root:$eb_name1[0]:dataV_peakheight
eb_ehl[0] = root:$eb_name2[0]:dataV_peakheight
eb_ehs[0] = eb_ehs[0]/short_rt
eb_ehl[0] = eb_ehl[0]/long_rt
solid = 100 * (((31/(28 - 31*const[0]))*(eb_ehl[0] - eb_ehs[0])/eb_ehl[0]))
print "percent solid " , solid
//make /N=61 eb_con, eb_md, eb_m0, eb_solid, eb_m1
//eb_con[temperature-ieb]  = const[0]
//eb_md[temperature-ieb] = moments_diff[0]
//eb_m0[temperature-ieb] = moments[0]
//eb_m1[temperature-ieb] = moments[1]
//eb_solid[temperature-ieb] = solid
eb_con[ieb]  = const[0]
//eb_md[ieb] = moments_diff[0]
//eb_m0[ieb] = moments[0]
//eb_m1[ieb] = moments[1]
eb_solid[ieb] = solid
DoWindow /K Table0
Edit /W=(20,300,600,300) temp_C, eb_name1, eb_name2, eb_con, eb_ehs, eb_ehl, eb_solid as
"SpectrumOutput"
KillWaves short, long, const
//KillWaves moments moments_diff, moments_short
string dif_name="difference" + num2str(temperature)
rename difference $dif_name
End
```

Appendix A-3: Mathematical derivation of the formula for calculating the percentage of the solid phase component in MSC containing Cer16-d_{31}. Adapted from Dr. E. E. Brief (Based on comments from Dr. J. L. Thewalt)

This appendix is intended to show a series of mathematical derivations of the formula developed by Dr. E. E. Brief for calculating the percentage of the solid phase component in MSC containing Cer16-d_{31}. Note that the information presented here is adapted directly from Dr. E. E. Brief. For convenience, we take the 25°C spectra as an example.

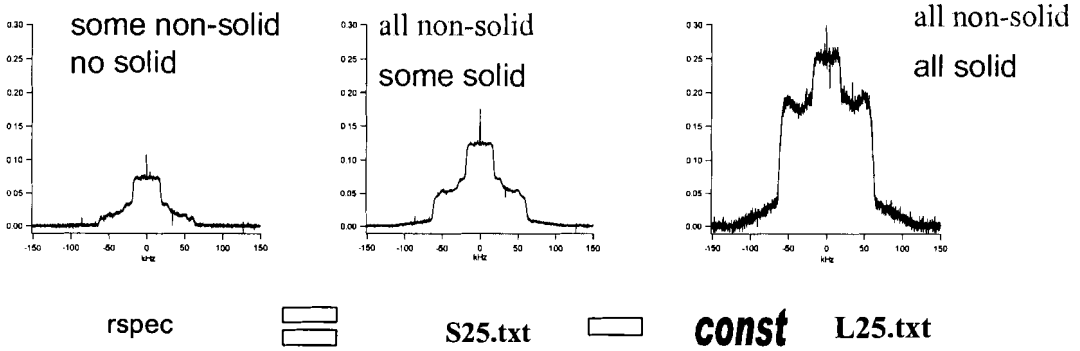

Let A = solid spectrum

B = non-solid spectrum

And $A + B = 1$

Long reptime spectrum $(L25.txt) = A + B$

Short reptime spectrum $(S25.txt) = \left(\frac{3}{n+c}\right)A + B$, where $0 \leq c < 1$.

So, $\left(\frac{3}{n+c}\right)A$ is the fraction of solid from the methyl group $\left(\frac{3}{n}\right)$ and the fraction of solid which relaxes quickly (that's why we can see it in the short reptime spectrum) and B is the entire non-solid component.

The difference spectrum $(\text{rspec}) = (\text{S25.txt}) - c(\text{L25.txt})$, where $0 \leq c < 1$.

$$= \left(\frac{3}{n} + c\right)A + B - c(A + B)$$

$$= \left(\frac{3}{n}\right)A + (1 - c)B$$

Now, to find $\frac{A}{A+B}$ = fraction of solid, first dividing rspec with (A + B).

We get:

$$\frac{\text{rspec}}{A+B} = \left(\frac{3}{n}\right)\left(\frac{A}{A+B}\right) + (1-c)\left(\frac{B}{A+B}\right)$$

$$\frac{M_0(\text{rspec})}{M_0(\text{L25.txt})} = \left(\frac{3}{n}\right)\left(\frac{A}{A+B}\right) + (1-c)\left(1 - \frac{A}{A+B}\right)$$

$$= \left(\frac{3}{n} + c - 1\right)\left(\frac{A}{A+B}\right) + (1-c)$$

$$\therefore \frac{A}{A+B} = \frac{\left[\frac{M_0(\text{rspec})}{M_0(\text{L25.txt})} - 1 + c\right]}{\left(\frac{3}{n} + c - 1\right)}$$

$$= \frac{n\left[\frac{M_0(\text{rspec})}{M_0(\text{L25.txt})} - 1 + c\right]}{(3 + nc - n)}$$

$$= \frac{n}{(3 + nc - n)}\left[\frac{M_0(\text{rspec})}{M_0(\text{L25.txt})} - 1 + c\right]$$

$$= \frac{n}{(n - 3 - nc)}\left[1 - c - \frac{M_0(\text{rspec})}{M_0(\text{L25.txt})}\right]$$

So, the percentage of the non-solid component in MSC containing Cer16-d_{31} can be written as:

$$\%non-solid = \frac{non-solid}{non-solid+solid} \times 100 = \frac{nM_0(rspec)}{(n-3-nf)\cdot M_0(L25.txt)} \times 100$$

Thus, the percentage of the solid phase component in MSC containing Cer16-d_{31} can be written as:

$$\%\ solid = \left(\frac{n}{n-3-nc}\right)\left(\frac{EH_L - EH_S}{EH_L}\right) \times 100$$

Appendix A-4: "MestRec" graphing analysis program

"MestRec" graphing analysis program was received from courtesy of Dr. A. Tracey, Department of Chemistry, Simon Fraser University. This program is licensed to Thewalt Laboratory, Department of Molecular Biology and Biochemistry. The following is the "MestRec" analysis procedure for analyzing ^{1}H-NMR and ^{13}C-NMR spectra.

Procedure 7: The "MestRec" spectral analysis program analysis procedure for plotting ^{1}H-NMR and ^{13}C-NMR spectra of FID data acquired from MA- d_{27} and IPM-d_{27}.

Step	Procedure
1	Import the FID data
2	Fourier-transform the FID data (use the default values)
3	Perform auto-zero function and baseline correction
4	Assign the chemical shift for individual peaks
5	Assign the area-integration for individual peaks

Appendix B: Nuclear Magnetic Resonance Spectroscopy (NMR) Supplemental

Appendix B-1: The History of NMR spectroscopy - continuous wave NMR spectroscopy and pulse NMR spectroscopy

The technical development of NMR spectroscopy has undergone for decades. In the early days, NMR spectroscopy was used to observe the nuclear magnetic resonance in bulk materials by sweeping the radio frequencies (RF) through a sample in a fixed magnetic field, or sweeping the field through a sample in a fixed/constant radio frequency. The results would contain sets of data points that show a time varying signal known as the Free Induction Decay (FID) (Refer to Section 2.2.2). By converting this time varying signal to a frequency varying signal using the Fourier transformation procedure (Refer to Section 2.2.4), an NMR spectrum can be obtained. During the sweeping process, if the resonance frequency is matched, a Lorentzian line would be observed on the spectrum at the resonance frequency. This process is called continuous wave NMR spectroscopy (cw NMR). It is generally a slow procedure because of the slow passage of frequency/field sweep. To find an alternative procedure to cw NMR, Bloch *et. al.* suggested applying short square pulses of RF power at a discrete frequency (Hahn's theory) (Farrar and Becker, 1971). All the input frequencies go into the processor at once and the output will consist of a range of frequencies inversely proportional to the data acquisition time, as well as absorption and signal intensity at each frequency, all at once. This method has become the most frequently used technique in today's NMR spectroscopy: the pulse method which is the origin of the "pulse" NMR spectroscopy. In this process, the nuclear spin system is observed only after a pulse of RF is turned off. (Fukushima and Roeder, 1994; Farrar and Becker, 1971)

The invention of the Fourier Transformation technique has brought spectroscopy into a whole new era. It enables the transformation of the FID into a range of frequencies to obtain a spectrum with absorption signal intensity at each frequency. That is, it allows the transformation of an FID from a time domain into a frequency domain. (Farrar and Becker, 1971)

A schematic diagram is provided in Figure 41 with a detailed description of each stage of the entire process of NMR. (Reusch, 2004)

(i) Gyroscope showing rotational inertia

(ii) Magnetic Moment in External $\mathbf{B}_0$ Field

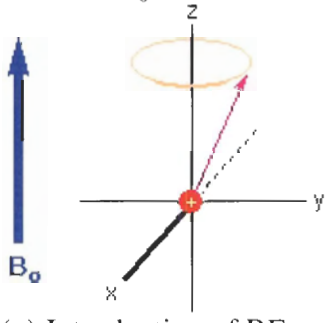

(iii) Net Magnetization of Nuclear Spins

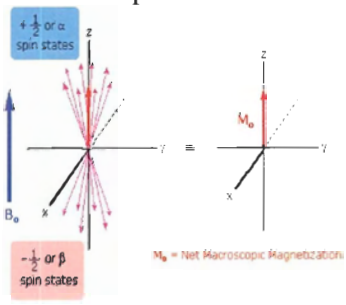

(iv) The axis of RF input & Signal detection

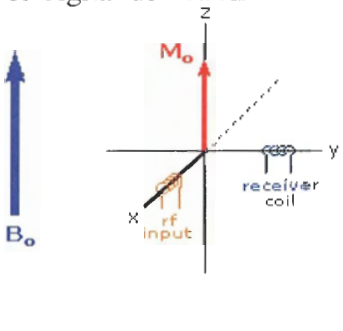

(v) Introduction of RF and Energy Absorption

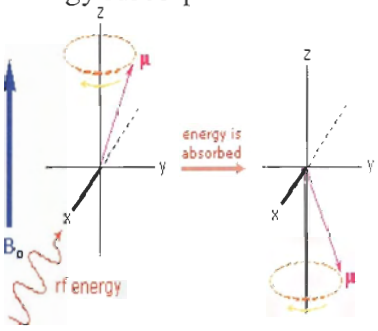

(vi) Probability of absorption

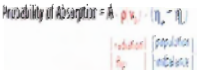

(Vii) The output signal consists of different frequencies as from the chime

(viii) Different frequencies add up to a single signal

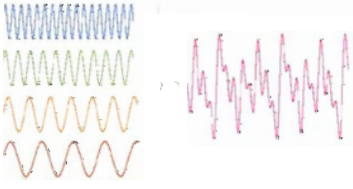

(ix) Fourier transform of the signal from time domain into frequency domain

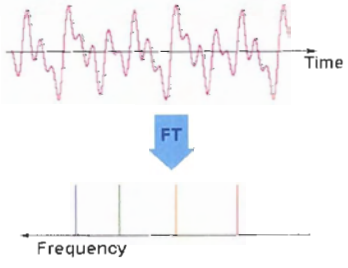

Figure 41: Process of NMR excitation

[Adapted from Reusch, W., Michigan State University.] (Reusch, 2004)

Appendix B-2: NMR time-scale

NMR has a slow time-scale according to the following calculation:

$$\frac{1}{2\pi\left(126\times10^{3}\,\mathrm{Hz}\right)}$$
$$=\frac{1}{792\times10^{3}\,\mathrm{rad}\cdot\mathrm{sec}^{-1}}$$
$$\approx 1.263\ \mu\mathrm{sec}$$

However, this slow time-scale allows the observation of averaged molecular motions over a period of 10^{-4} s~ 10^{-5} s. To complement, one could use other spectroscopic techniques with faster time-scale such as Raman and IR spectroscopy, which would image a snapshot of the molecule instead of motional averaging. By combining these techniques, one can recreate a reasonable image of the sample. Despite the slow time-scale, ^{2}H-NMR can still provide sufficient information on the macroscopic observation as the nuclei contribute to the signal. (Abraham *et al.*, 1997; Rowat, 1996).

Appendix B-3: Curie's law

At room temperature, there are more spins aligned with the external magnetic field in order to reach their equilibrium state at the lower energy level. The total equilibrium magnetization is thus created and its value is given by Curie's Law:

$$\vec{M}_0 = \frac{N\gamma^2\hbar^2 I(I+1)}{3kT}H$$

Equation 16: The Curie's Law

Where $\mathbf{M}_0$ is the total magnetization; N is the number of spins; γ is the magnetogyric ratio [$sec^{-1} \cdot T^{-1}$]; k is the Boltzmann's constant [1.38066×10^{-23} $J \cdot K^{-1}$]; **H** is the field [T]; T is the temperature [°K]; and Ih is the angular momentum [$kg \cdot rad \cdot sec^{-1}$]. (Fukushima and Roeder 1994)

Appendix B-4: The schematic diagram of the probe

Some probes are designed to be able to fit between the pole faces of a magnet or in the bore of a superconducting solenoid.

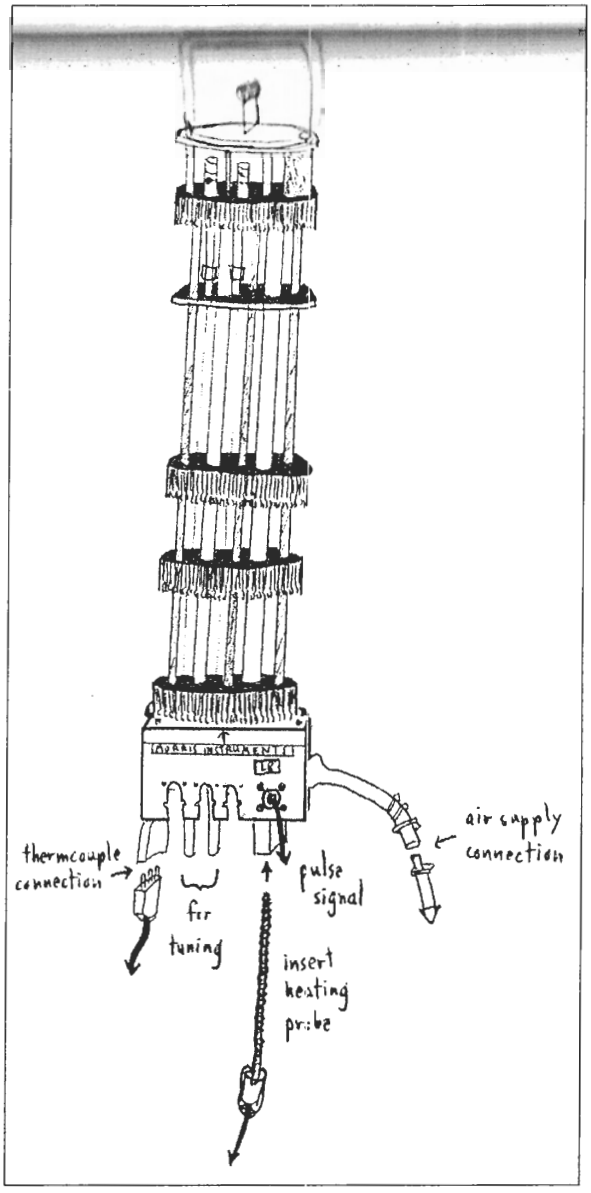

Figure 42: The schematic diagram of the probe

[Courtesy of Rowat, A., Simon Fraser University.] (Rowat, 1996)

Appendix B-5: FID along different axes

It is important to understand the electronics for obtaining an FID. The receiver coil is located along and picks up the signal along the y axis. The U channel is the real data acquisition channel and it is phase with the y axis. The V channel is the imaginary data acquisition channel and it is in phase with the –x axis. If a pulse is applied in different axes, the FID can be at a full positive/negative signal or zero signal. Figure 43 shows the schematic demonstration.

(i) **M** is tipped to the y axis by $\mathbf{H}_1$ applied along the x axis. U channel picks up the maximum positive signal along the y axis.

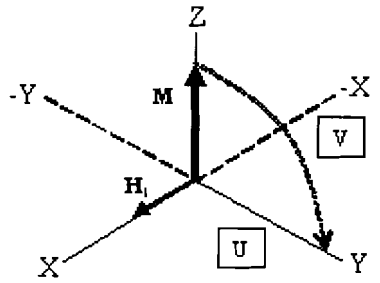

(ii) Now, **M** is tipped to the -x axis by $\mathbf{H}_1$ applied along the y axis. U channel is fixed along the y axis, so it picks up no signal along the y axis.

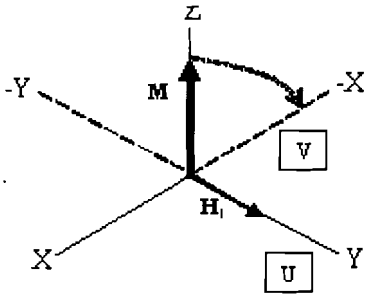

Figure 43: The relationship between U/V channel and FID signal detection.

The pulse is applied along (i) x axis leading to a maximum positive signal or (ii) y axis leading to a zero signal. The signal will have different FID amplitudes, either zero or maximum, depending on the position M is tipped to. (Rowat, 1996)

Appendix B-6: T_1 relaxation supplemental (Inversion recovery theory)

This is also known as the longitudinal relaxation or spin-lattice relaxation. Spin-lattice relaxation is defined to be the process of spins aligning toward the equilibrium magnetization along the external magnetic field with a time constant T_1, at where 26.4% of the magnetization recovers to the equilibrium position according to the equation of Inversion Recovery (Fukushima and Roeder, 1994):

$$\vec{M}_z = \vec{M}_0\left(1-2e^{\frac{-\tau}{T_1}}\right)$$

Equation 17: T_1 relaxation (Inversion recovery)

Where $\mathbf{M}_0$ is the equilibrium magnetization; $\mathbf{M}_z$ is the vector quantity of $\mathbf{M}_0$ in z axis; τ is the time between the 180° and 90° pulse in 180°-τ-90° pulse sequence which will be discussed later in this section. T_1 is the time constant for spin-lattice relaxation as mentioned. (Fukushima and Roeder, 1994)

The energetic or thermodynamic process of spin-lattice relaxation can be understood from the following perspective. When an object is inserted into a magnetic field sufficiently stronger than the environmental magnetic field from the earth, the spins in the object with magnetic moment μ antiparallel to the external field will try to align with the field. In order for this process to occur, the spins would have to give up their potential energy against the field, $+\mu\mathbf{H}$, to other media. The spins would not be able to go to the lower energy state without a mechanism to transfer this potential energy to other repositories for thermal energy, for example, rotations, translations, and vibrations,

collectively called the "lattice". This is the reason why it is called the spin-lattice relaxation. (Fukushima and Roeder, 1994)

An interesting phenomenon to notice is that the spins can jump from the higher energy state to the lower energy state by simply emitting an energy-rich photon or particle. But, sometimes, they may need to be stimulated as the probability for spontaneous transition between the energy states is not sufficiently high. So, most NMR transitions are stimulated by the fluctuating field where an unpaired electron can cause the nuclear relaxation, as an example. (Fukushima and Roeder, 1994)

The value of T_1 depends on the strength of the coupling between the spin system and the lattice. Various modes of interactions have been discovered and suggested to facilitate this exchange of energy between the two systems. Examples are magnetic dipole-dipole interaction, electric quadruple interaction and scalar-coupling interaction. (Farrar and Becker, 1971)

The 180°-τ-90° sequence is commonly used to measure T_1. The 180° pulse would tip the $\mathbf{M}_0$ to –z axis. Then, the longitudinal relaxation would proceed where $\mathbf{M}_z$ starts returning from –z axis to back to it equilibrium value $\mathbf{M}_0$ along z axis again. After a period of time τ, where the relaxation is still in progress, another 90° x-pulse will be applied to rotate **M** to the y axis. At this point, the receiver coil should pick up the FID signal along the y axis. Then, the spectrometer is able to obtain information on the changes in FID amplitude and the decay rate of $\mathbf{M}_z$ with respect to different values of τ by repeating the experiment with this pulse sequence over a range of τ. Generally, the range of τ value should extend to be sufficiently higher, ideally 4 ~ 5 times greater than T_1. Other methods are also available for finding T_1 such as using the pulse sequence

"90°-τ-90°" or "90°-τ,-90-τ,...". However, the 180°-τ-90° pulse sequence is the most widely used pulse sequence for measuring T_1. (Farrar and Becker, 1971)

Figure 44 shows the 180°-τ-90° pulse sequence:

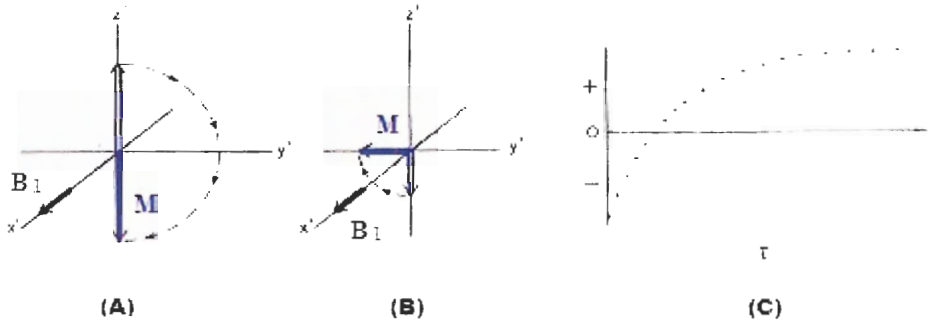

Figure 44: The 180°-τ-90° pulse sequence.

(A) **M** is tipped by a 180° pulse $\mathbf{B}_1$ at time 0. (B) After a time τ, a 90 pulse ($\mathbf{B}_1$) rotates **M** to the y or –y axis. (C) The initial FID amplitude after the 90° pulse, which is proportional to the value of **M** at time τ, is plotted as function of τ. Note that each point results from a separate the 180°-τ-90° pulse sequence. [Adapted from Farrar, T. C. and Becker, E. D., 1971. *Pulse & Fourier Transform NMR*, p. 21, Academic Press Inc.] (Farrar and Becker, 1971)

Appendix B-7: T_2 relaxation supplemental

T_2 relaxation is also known as the spin-spin relaxation or transverse relaxation. This process causes the $\mathbf{M}_{xy}$ component of **M** to decay over time after **M** is tipped to the y axis by a 90° x-pulse. T_1 and T_2 may have similar values mostly in liquids, but they may have very different values in solids. When T_1 approximately equals T_2, the relaxation times do not provide different information, but when they differ they do. Figure 45 shows how the transverse relaxation occurs.

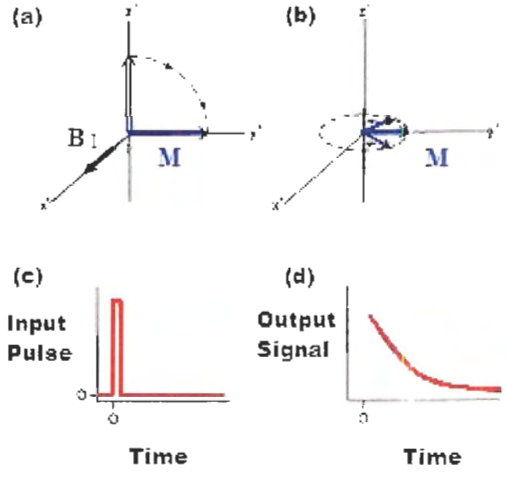

Figure 45: The transverse relaxation mechanism.

(a) A 90° pulse along x axis rotates **M** from the equilibrium position to the y axis. (b) **M** decreases as magnetic moments dephase. (c) Input signal, a 90° pulse, corresponding to (a). (d) Exponential free induction decay, corresponding to (b). [Adapted from Farrar, T. C. and Becker, E. D., 1971. *Pulse & Fourier Transform NMR*, p. 19, Academic Press Inc.] (Farrar and Becker, 1971)

Interestingly, different magnitudes of T_2 may pose problems as well. If T_2 is very long, then the inhomogeneity of the magnetic field would cause faster dephasing of spins than T_2. But, if T_2 is too short, then the FID already disappears before the receiver coil can pick up the signal after its instrumental dead time is over. Therefore, it is important to

try to avoid very short T_2 by setting a longer range of τ so an echo can still form later than the end of the instrumental dead time. (Fukushima and Roeder, 1994)

How is T_2 measured? It is very common to use the spin-echo technique. This technique has been known for overcoming the inhomogeneity problem. The pulse sequence is 90°-τ-180°. The echo is set to be observed at a time 2τ after the middle of the first pulse. The first 90° x-pulse tips the magnetization, $\mathbf{M}_0$, to the y axis. After a time τ, the spins dephase along the xy plane in opposite directions. At a time τ, a 180° x-pulse is applied to flip the spins 180° about the x axis to the opposite side of the plane. So now, the spins are moving toward each other and eventually will rephase and give an echo at the time 2τ along the –y axis. Generally, the receiver or detector should not be phase sensitive for the pulse sequence, so that it will still pick up positive FID amplitude at signal echo. If should it be phase sensitive, then the 180° y-pulse can be used to rotate the spins 180° about the y axis instead so that the spins would rephase in the y axis to give a positive FID signal. After the echo, the spins will continue their movement and dephase again. (Farrar and Becker, 1971)

Generally, if there is no transverse or longitudinal relaxation, then the rephrasing of spins at the time 2τ should give the maximum amplitude as the initial FID. However, as the value of the time τ increases, the spins decrease in magnitude during precession in time 2τ due to the time constant T_2 in the transverse relaxation. Therefore, in order to find the correct value of T_2, a graph of the FID amplitude versus the time τ should be plotted. (Farrar and Becker, 1971)

When a magnetic field, $\mathbf{B}_1$, is applied along the x axis, the total magnetization, **M**, will be tipped to, if by a full $\pi/2$ pulse, to the y axis. $\pi/2$ pulse is the pulse length in time unit required to tip **M** 90° fully from the z axis to the xy plane. When $\mathbf{B}_1$ is turned off, **M** undergoes the transverse relaxation where it decays in the xy plane. The component of **M** along the y axis is called $\mathbf{M}_y$. Over time, the $\mathbf{M}_y$ component of **M** decays. This is the process of spin-spin relaxation. This relaxation occurs when the nuclei exchange energy with each other, and the magnetic moments of $\mathbf{M}_y$ spread out in the xy plane with a time constant, T_2.

In addition, the inhomogeneity of $\mathbf{B}_0$ could cause the nuclei to experience different magnetic field strengths in different portions of the sample. As a result, nuclei would precess at different frequencies, slightly faster, slower or the same as the rotating frame. $\mathbf{M}_y$, through this process, would eventually perish to zero with the time constant, T_2^*. Overall, T_2^* is very short compared to T_2 and T_1 and therefore, it dominates FID. In general, $T_2^* \leq T_2 \leq T_1$.